2
2007

This is to certify that the
thesis entitled

AMPLITUDE-MODULATED EXCITATION OF A SEPARATED FLOW USING AN EXTERNALLY DRIVEN HELMHOLTZ RESONATOR

presented by

Antonius Krisna Aditjandra

has been accepted towards fulfillment
of the requirements for the

Master of Science degree in Mechanical Engineering

Major Professor's Signature

3/8/2006
Date

MSU is an Affirmative Action/Equal Opportunity Institution

AMPLITUDE-MODULATED EXCITATION OF A SEPARATED FLOW USING AN EXTERNALLY DRIVEN HELMHOLTZ RESONATOR

By

Antonius Krisna Aditjandra

A THESIS

Submitted to
Michigan State University
in partial fulfillment of the requirements
for the degree of

MASTER OF SCIENCE

Department of Mechanical Engineering

2006

ABSTRACT

AMPLITUDE-MODULATED EXCITATION OF A SEPARATED FLOW USING AN EXTERNALLY DRIVEN HELMHOLTZ RESONATOR

By

Antonius Krisna Aditjandra

A flow-excitation scheme based on an externally driven Helmholtz resonator was developed in order to force, and alter the global characteristics of, the separated flow over an axisymmetric, backward-facing step. Because the resonance frequency of the forcing device was well above the range in which the flow is receptive to excitation, low-frequency, amplitude modulation of the resonator's disturbance was employed to effectively excite the separated shear layer, causing shrinkage of the separation bubble. This approach also prevented contamination of measurements of the unsteady wall-pressure beneath the separating/reattaching flow by acoustic noise from the forcing device.

The driven resonator was employed to force the flow over a range of forcing frequencies and amplitudes. An optimal forcing frequency, corresponding to a minimum bubble size for a given forcing level, was found at a non-dimensional forcing frequency of $F^+ \approx 0.541$. Additionally, unsteady-wall-pressure measurements were conducted employing a 15-microphone sensor array. A frequency-wavenumber-spectrum analysis of these data suggested that the spatial scale, i.e., streamwise wavenumber, of the wall-pressure disturbance at a given forcing frequency could be predicted from the unforced flow's frequency-wavenumber spectrum. This finding could be useful in devising "wavenumber control" schemes for controlling flow-induced noise and vibration.

DEDICATION

To Papa, Mama, Paulus, and Karin,

for their everlasting devotion, compassion, and love

ACKNOWLEDGEMENTS

I would like to express my gratefulness to my advisor, Dr. Ahmed Naguib, whom I have learned so much from throughout the seven years span he had taken me as his undergraduate research assistant and graduate student. Dr. Naguib has truly been a wonderful and supportive advisor, teacher, and motivator that challenged his students to be the best that they can be. Outside the academic world, Dr. Naguib has shown amiable friendship that helped propel me through this research project. So, Dr. Naguib, *thank you*!

Many thanks to my thesis defense committee members, Dr. Manooch Koochesfahani and Dr. Brian Feeny, for their constructive inputs and recommendations of this thesis project. I would also like to acknowledge Roy Bailiff and Mike Mclean for their help at the machine shop; Jill Bielawski, Aida Montalvo, and Elaine Bailey for their help with numerous kinds of paperwork.

I would also like to thank my fellow graduate students from the Flow Physics and Control Laboratory: Laura Hudy, Yongxiang Li, Mohamed Daoud, Chad Stimson, and Barry Trosin for their assistance with the data collections and many discussions regarding my research projects. Their friendship and camaraderie throughout the years surely did not go unnoticed. Also, I would like to acknowledge Ke Zhang and Brendan Vidmar for their useful feedback on my thesis. Thanks are due to TMUAL and TSFL groups for the fun times together researching, teaching, attending MUFMECH, and socializing.

Aside from academia, I would like to thank some of my friends: Kathy Weathers, Liz Schweitzer, Fr. Jerry Vincke, Betsy Murphy, Ken Stinson, Margaret Beahan, Megan McCullough, The Liberato's, and St. John's Pastoral Team/Staff. Especially for my best friends, I must extend my special thankfulness. Brian Preston for the great times we

spent together camping, fishing, and hanging out talking about science. Elaine and Neal Adams for the abundant support and encouragements they provided me with and the many meals and fun family times we shared together. Stefanus Tanaya for being a cool roommate for so many years, which of course came with the package of many late night conversations, "*Gran Turismo*" challenges, and cars fixings together ... even when the temperature outside was below 25°F. Fr. Mark Inglot for the prayers, encouragements, and many glasses of excellent "*vino*" that went along with many philosophical discussions. The Preston's for their kindness and making me be apart of their family. They have made my many years at MSU that much more fun, meaningful, and enjoyable.

Last but not least, I must thank the most important people in my life. Thank you, Mama and Papa, for *everything* that you have done for me. Without the two of you, I would not be where I am at in my life right now. The two of you have taught me how to thrive and succeed in life. I am indebted to the two of you and I would like to especially express my deepest gratitude, from the bottom of my heart, for your unending support and love. I am forever grateful to have you as my parents. To my brother, Paulus, and his family, Fanny and Sean-Oliver, thank you for all of your support and love you have generously given to me throughout my life. Thank you for all of the long distance encouragements you provided me with concerning life and graduate school ... England surely is not close by. Finally, I would like to thank my sister, Karin, for her unwavering love and support throughout my life. I cherished the many unforgettable moments we shared together traveling across US and here at MSU. Also, I would like to thank Bryan, my sister's husband, for his support. Life really is that much better with all of you in it!

This research project was made possible through NSF grant #CTS0116907.

TABLE OF CONTENTS

LIST OF TABLES

LIST OF FIGURES

IMAGES IN THIS THESIS ARE PRESENTED IN COLOR

NOMENCLATURE

A magnitude response of second order system

c speed of sound at ambient temperature

C_p $= \dfrac{(P_x - P_\infty)}{\frac{1}{2}\rho_{air}U_\infty^{\,2}}$ = mean pressure coefficient

C_μ $= \dfrac{2du_{j,rms}^{\,2}}{HU_\infty^{\,2}}$ = momentum-based non-dimensional forcing-level coefficient

d slit width of resonator

f frequency

f_c carrier frequency

f_e $= 2f_m$ = excitation frequency

f_m modulation frequency

f_s sampling frequency

F^+ $= \dfrac{f_e L}{U_\infty} = \dfrac{2f_m x_r}{U_\infty}$ = reduced forcing frequency

H step height of backward-facing step

J resonator's system-response function

k discrete-frequency index

k_x wavenumber

l neck length of resonator

l' effective neck length of resonator

L length scale characteristic of the separation bubble size

N number of samples in a time series

p_a driving acoustic pressure of the Helmholtz resonator

$p_{a,p\text{-}p}$ peak-to-peak driving acoustic pressure of the Helmholtz resonator

p_c pressure inside the cavity of resonator

p_i acoustic pressure imposed at the slit opening of resonator

p'_w fluctuating wall-pressure

P_x mean surface pressure at a given streamwise location

P_∞ freestream pressure

q $= \sqrt{u^2 + v^2}$ = velocity magnitude

$<q>$ phase-averaged q

q' unsteady component of q

q_{max} maximum magnitude of q

Q time averaged component of q

r radius of circular neck opening for conventional resonator

Re_d $= \frac{U_{avg} d}{\nu}$ or $\frac{U_{\max} d}{\nu}$ = Reynolds number based on the resonator's slit width, d

Re_H $= \frac{U_\infty H}{\nu}$ = Reynolds number based on the step height, H

S surface area of the resonator's opening

St_d Strouhal number based on the resonator's slit width, d

St_l Strouhal number based on the neck length of resonator, l

t time

T period of forcing signal

u streamwise velocity component

$u_{j,rms}$ RMS jet velocity at frequency of $2f_m$

U_{avg} average jet velocity during ejection phase of a driven resonator

U_{max} maximum jet velocity during ejection phase of a driven resonator

U_∞ freestream velocity

v wall-normal velocity component

V cavity volume of resonator

x streamwise coordinate relative to back-step edge

x_r mean reattachment length

y wall-normal coordinate

$z(t)$ amplitude-modulated signal

Z Amplitude of amplitude-modulated signal

δ end correction factor for estimation of the resonance frequency of the acoustical resonator

ζ damping ratio

ϕ_{bb} power spectrum of quantity b

ϕ_{gb} cross spectrum between quantities g and b

ϕ_{QQ} power spectrum of Q

Φ phase angle of second-order mechanical system

Γ_{gb} coherence between quantities g and b

ρ_{air} density of air

ν kinematic viscosity

ω $= 2\pi f =$ angular frequency

ω_o angular natural frequency

1 INTRODUCTION

1.1 Background

1.1.1 Nature of the separated flow over a backward-facing step

Separated flows are encountered frequently in engineering applications. Examples include flow over wings, turbine and compressor blades, inside diffusers, and around automobiles. The occurrence of flow separation generally, but not always, results in adverse effects on the performance of engineering devices: reduced lift, increased drag, generation of noise and vibration, etc. Therefore, it is desirable to understand the flow physics associated with separated flows for the purpose of predicting, and hence design for minimizing, these adverse effects as well as for devising passive or active flow control schemes to eliminate or reduce the separated flow regions.

A fundamental flow geometry that is frequently used as a model for separated flows in the laboratory is the backward-facing step. Extensive studies have been done on separating and reattaching flows over the simple, classical geometry of a backward-facing step using a variety of both experimental and numerical methods. This geometry is fairly simple, however, the structure of the flow downstream of the step is rather complex and retains many of the features of the flow structure encountered in engineering applications.

Generally speaking, there are four flow-regions downstream of the back step: a separated free shear layer, primary and secondary re-circulating flows, and redeveloping boundary layer. As depicted in Figure 1.1, the shear layer separates from the edge of the back step. The discontinuity in the geometry creates substantial velocity variations across the separated, thin shear layer, with low-speed flow on the lower side of the layer

and high-speed flow on the other side. The resulting large, velocity gradient leads to the formation of spanwise, wall-parallel vortices that originate from the well-known Kelvin-Helmholtz instability. These vortices grow in size and convect downstream with a convection velocity that is typically in the range of 50 – 60% of the freestream velocity.

The primary re-circulation region is caused by the need to balance the entrainment flow into the separated shear layer. In this region, the flow is highly unsteady and it "drives" the, low-speed, second re-circulating region located just downstream of the back step. Driver *et al.* (1987), Heenan and Morrison (1998), Cherry *et al.* (1984) and Lee and Sung (2001, 2002), amongst others, argue that the unsteadiness in this particular region is due to the 'flapping' of the shear layer.

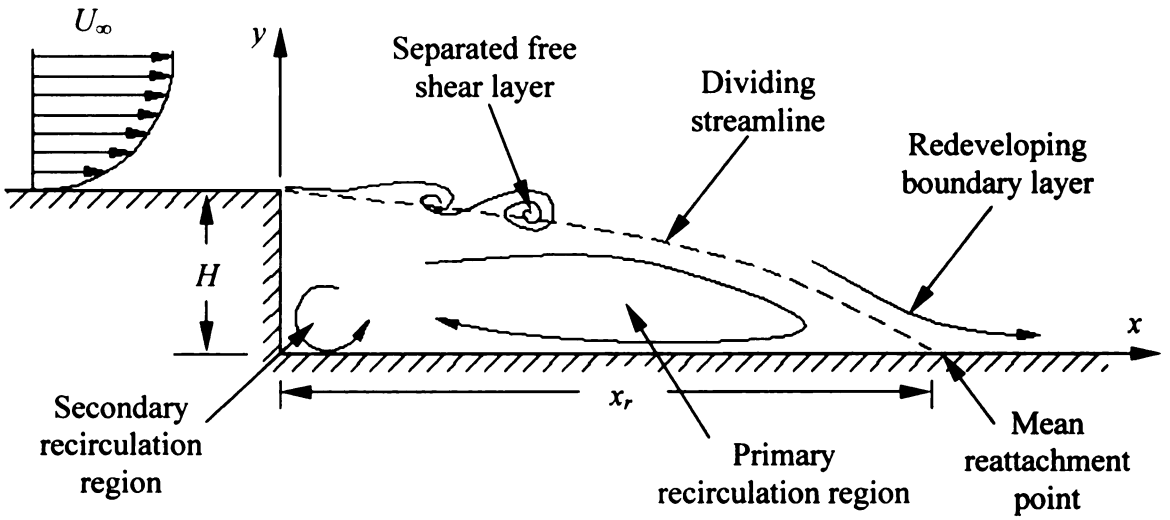

Figure 1.1. Backward-facing step flow features

The above scenario of the flow structures in the backward-facing step flow represents the generally accepted view. However, in the more recent study of Hudy *et al.* (2006) over an axisymmetric, backward-facing step, an alternate view was proposed. Utilizing an array of wall-pressure microphones to estimate the spatio-temporal evolution

of the flow structure downstream of the step through linear stochastic estimation, Hudy *et al.* (2006) proposed that a wake-like flow structure is dominant within the separation bubble. In this alternative scenario, large-scale (order of step height) vortex structures roll up from the separated shear layer at a location that is nominally half the reattachment distance downstream from the step. Once they reach a size comparable to the step these vortices accelerate and convect downstream. Hudy *et al.* (2006) attributed the difference between this scenario, which supports observations from an earlier computational study by Wee *et al.* (2002), and the traditionally accepted one to be related to the spanwise uniformity of the mean flow in the axisymmetric study. The bulk of the literature on the backward-facing-step flow is based on a rectangular geometry, which suffers from end-wall effects.

1.1.2 Control of separated flows

The concept of traditional boundary layer control (i.e., steady blowing or suction through a slit opening) introduced by Prandtl in 1908, according to Greenblatt and Wygnanski (2000), has been well studied. It was found that these traditional methods for controlling the flow work well. However, more recent research showed that a more efficient way to control separated flows is by periodic excitation of the boundary layer at separation. In 1948, Schubauer and Skramstad (1948) first introduced this type of flow control by periodically exciting the laminar boundary layer to produce a known instability called Tollmien-Schlichting waves (stated in Greenblatt and Wygnanski, 2000).

In periodic forcing of separated flows, it is generally believed that large coherent structures are responsible for the momentum transfer that leads to the control of the

separated flow. These coherent flow structures, which are generated by the flow instability to the periodic excitation, produce a significant change in the behavior of the separated flow region. In other words, "excitation accelerates and regulates the generation of large coherent structures, ... transferring high momentum fluid across the mixing layer", according to Greenblatt and Wygnanski (2000). Amitay *et al.* (2001) also suggested that "forcing of a separated flow by means of oscillatory net mass injection, ... has been found to be an effective means for control of separation with substantially less mass flux than required from steady blowing." Therefore, periodic excitation appears to be the more effective and preferred method to control a separated flow as opposed to the traditional steady blowing/suction method.

1.2 Literature review

There are various means by which periodic excitation can be achieved. Since the primary focus of the present investigation is to develop such a method for the control of an axisymmetric, backward-facing-step flow, a brief review of methods for separated-flow control is given here, along with highlights of the influence of oscillatory control on the flow behavior. It is to be noted that the review is only intended to outline some of the popular ways for achieving the control through representative studies rather than providing a comprehensive list of all possible control approaches and in-depth analysis of the resulting flow behavior.

In general, there are two types of flow control: passive and active. In passive control, no actuator is required, and hence this type of control does not require external energy input. On the other hand, active control requires the use of an actuator that is driven utilizing external energy input. An example of a passive, yet unsteady, control of a separated flow may be found in the study done by Urzynicok and Fernholz (2002). These investigators employed a Helmholtz resonator that was driven to oscillate at resonance by the natural unsteadiness of the flow above the resonator's opening, and hence the unsteady control input to the flow did not require external energy. Urzynicok and Fernholz (2002) utilized the passive resonator to demonstrate separation control in diffuser and airfoil flows. Though the approach of the passive-driven resonator is attractive, there are no means by which the device operation could be adjusted to changes in the Reynolds number and other flow conditions. Specifically, since the resonance frequency of the excitation device is not guaranteed to match the natural, or optimal-control, frequency of the flow, the control is most effective only over a narrow range of

flow parameters. It is also notable here that Urzynicok and Fernholz (2002) found that the most effective location for controlling the separated flow was to locate the resonator opening as near to the point of separation as possible.

Amitay *et al.* (2001) gave an example of actively controlling the separated flow over an unconventional-profile symmetric airfoil. Eight piezoceramic disks (four disks for each of two actuators located side-by-side) were used to drive synthetic (zero net mass flux) jets that were placed along the spanwise dimension of the airfoil. The piezo disks were placed inside a cavity behind the jet exit, and thus, the actuators may be classified as internally excited devices. Amitay *et al.* (2001) implemented the flow control utilizing high and low actuation frequencies. The former frequency, $F^+ = 10.6$ (where F^+ is the frequency normalized using a length characteristic of the streamwise scale of the separated flow and the freestream velocity; the corresponding physical frequency is $f = 740$ Hz), was more than an order of magnitude larger than the natural shedding frequency of the airfoil, which was $F^+ \approx 0.7$ ($f \approx 50$ Hz). The low frequency of $F^+ = 1.5$ ($f = 110$ Hz) was selected to be within the receptivity range of the separated shear layer (i.e., on the order of the natural shedding frequency of the airfoil). The low actuation frequency was achieved by using the entire volume of the actuator cavity, highlighting the difficulty to design an actuator that has the capability of operating at the low-frequency range (where the flow is most unstable) when geometrical constraints are present.

Amitay *et al.* (2001) found that without the synthetic jet control, the flow separated at the leading edge of the airfoil at angles of attack beyond 5°. However, the flow became completely attached for angles of attack up to (and partially beyond) 17.5°

with the application of the synthetic jet control. The control was achieved through low actuation frequencies that were within the receptivity band of the separated shear layer rather than the high actuation frequencies. The Reynolds number range used for their study was between 3.1×10^5 and 7.25×10^5, based on the chord length.

Extending the work of Amitay *et al.* (2001), Glezer *et al.* (2005) emphasized the aspects of low- and high-frequency actuation for flow control. They systematically varied the actuation frequency, corresponding to five different Strouhal numbers (F^+) of 0.7, 1.1, 2.05, 3.3, and 10. They argued that low-frequency (order of the natural shedding frequency of vortex structures from the separated-flow zone) actuation produces time-dependent flow disturbances, whereas the high actuation frequency results in a basically time-invariant flow modification. In the former case, they found that the control led to persistency of the vortices beyond the trailing edge of the airfoil. They suggested that this was due to the effective coupling of disturbances to the flow at the excitation (also structure formation) frequency that was close to the natural shedding frequency of the airfoil. This means that the low-frequency control produced highly organized structures that advect downstream.

As the Strouhal number was increased to 3.3, Glezer *et al.* (2005) showed that the shear-layer vortices became smaller and "somewhat smeared", indicating a deterioration in phase-locking between the flow structures and the actuation. This led to the conclusion that the actuation becomes less effective as the actuation frequency was increased beyond a certain optimal value. However, Glezer *et al.* (2005) made a case that when the actuation frequency was increased to an even higher value (i.e., Strouhal number of 10), the flow would remain attached to the suction surface of the airfoil with

no "evidence of organized, phase-coherent vorticity concentrations." Therefore, the separated flow was well suppressed at adequately high (an order of 10 higher than the natural shedding frequency) actuation frequency.

Chun and Sung (1996) provided another example of active, oscillatory, control of a separated, turbulent, shear layer. For their investigation, they utilized a classical backward-facing-step geometry over a flat plate. At the point of separation, sinusoidal velocity disturbances were generated through a slit opening at the edge of the step that ran the full spanwise length of the back step. The main driver of this internally driven actuator was a subwoofer that was mounted to one of the walls of a cavity placed behind the slit. Actuation of the subwoofer led to the generation of disturbances that excited the main flow through the slit opening at the separation edge.

Chun and Sung (1996) demonstrated that the effect on the flow of local forcing at the separation edge was significant. The Reynolds number range used in their study was varied in the range $1.3\times10^4 \leq Re_H \leq 3.3\times10^4$ (where Re_H is the Reynolds number based on step height), while the actuation frequency was varied between 25 Hz and 5 kHz. Their findings indicated that as the forcing amplitude was increased, the reattachment length became shorter. This trend became non-linear, showing signs of saturation, beyond a certain, critical, forcing level. Furthermore, they found that the most effective forcing frequency for reducing the reattachment length was close to that of the vortex shedding frequency of the unforced flow (i.e., natural frequency of the separated flow), which was $St_H = 0.275$ (where St_H is the Strouhal number based on step height and freestream velocity). However, when the excitation frequency was increased in the range $St_H \geq 0.8$, the reattachment length became independent of the excitation frequency. In

fact, in this frequency range, the reattachment length became larger than that of the unforced case. Thus, the mechanism for reducing the reattachment length seemed to be more sensitive to the excitation frequency than the forcing amplitude.

In a later study, Chun *et al.* (1999) utilized the same experimental parameters and configuration as Chun and Sung (1996) in an attempt to understand the effect of *spanwise-varying*, local forcing on the turbulent separated flow over the back-step. The spanwise variation in the forcing was achieved by blocking the control-jet's slit opening at the step edge at periodically-placed locations along the span of the slit. The most effective forcing frequency, St_H = 0.27, was found to be the same for all spanwise wavenumber employed in the forcing. This frequency value was the same as found in their earlier investigation utilizing spanwise-uniform forcing.

In 1998, Chun and Sung (1998) undertook a visualization study of a, locally forced, laminar, separated flow over a backward-facing step in a water channel. The Reynolds number (Re_H) used in their experiment of 1200 was substantially lower than the other studies from the same group (cited above). The local forcing was of the form of an oscillatory jet driven by a scotch-yoke mechanism. The scotch-yoke mechanism, which was connected to a piston and cylinder system, could produce different forcing frequencies and amplitudes, leading to the establishment of a periodic jet through a slit at the edge of the back step. In the experiment, dye was used for visualization and LDV was utilized to measure the velocity components in the re-circulating-flow region. The range of forcing frequencies, in terms of Strouhal number (St_H) based on the step height, used in the study was $0.305 \leq St_H \leq 0.955$.

The findings of Chun and Sung (1998) showed that the optimum Strouhal number for shortening the reattachment length was 0.477. This value was higher than Chun and Sung (1996) and Chun *et al.* (1999) findings; however, the Chun and Sung (1998) study was for the case of a laminar rather than the turbulent separation examined in the latter studies. Moreover, this value was in the neighborhood of the natural-flow-instability frequency (St_H = 0.4) found by Roos and Kegelman (1986) in their backward-facing-step, flow study of laminar, separated shear layers. Chun and Sung (1998) also found that the reattachment length increases with increasing Strouhal number beyond the optimum-control Strouhal number, which was consistent with their previous assertion made in Chun and Sung (1996). Moreover, they claimed that the secondary re-circulation flow located just downstream of the back step disappeared all together when the optimum forcing frequency was applied.

In a review paper, Greenblatt and Wygnanski (2000) provided many examples to demonstrate the importance of oscillatory addition of momentum to produce effective hydrodynamic interaction between the actuators and the flow in active flow control. They believed that large, coherent structures, introduced by the oscillatory control, are responsible for enhancement in the momentum transfer across the separated flow, leading to reduction in the length of the separated flow. They also mentioned that periodic flow oscillations could be achieved by "speakers/acoustic drivers, pistons, oscillatory-flow valve-system, piezoelectric-based diaphragms two-dimensionally, or surface mounted mechanical actuators such as ribbons, fliperons, or piezo-based benders."

In contrast to a later study done by Glezer *et al.* (2005), which was briefly summarized above, who showed that higher reduced frequency (i.e., F^+ order of 10 or

higher) could be effective for controlling the separated flow, Greenblatt and Wygnanski (2000) suggested that the optimum reduced frequency, F^+, for the majority of the tested cases ranged between 0.3 and 4.

1.2.1 Helmholtz resonators: background, concepts, and physics

For reasons that will become clear in section 1.3, an externally driven Helmholtz resonator was selected as the actuating mechanism for the present study. However, before getting into the motivation of the present investigation, it is helpful to briefly summarize the origin, theory, design, and physics of a Helmholtz resonator.

The idea of a Helmholtz resonator was first introduced and theorized in 1860 by Hermann von Helmholtz. This acoustic resonator was later named after Helmholtz and employed in the mid of 19th century for sound amplification of particular frequencies from a complex sound field. Moreover, this idea was applied, quite universally, as a sound-damping system in jet engines, train stations, and many other sound-damping applications. A Helmholtz resonator, also known as acoustic absorber, is basically a rigid container (or cavity) containing fluid (e.g., air) with an opening (or "neck"). A driven Helmholtz may be modeled using a simple, single-degree-of-freedom, second-order, spring-mass-damping system. The fluid that occupies the volume within the neck of the resonator acts as the mass, the compressible air inside the cavity behaves as spring stiffness, and viscous dissipation as well as sound radiation from the resonator provides damping. A schematic of a typical Helmholtz resonator is shown in Figure 1.2.

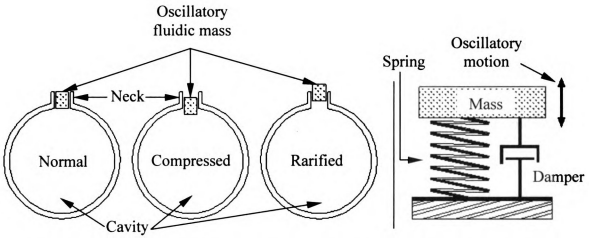

Figure 1.2. A sketch of a Helmholtz resonator during oscillation (left), and equivalent second-order mechanical system (right)

The driving source of oscillations in a resonator can be either fluidic or acoustic. In response, the driven Helmholtz resonator produces oscillations of the mass of air contained within the neck of the resonator. During oscillation, when the mass is pushed slightly inside the cavity, the fluid within the rigid container will be compressed. Consequently, the cavity pressure will rise and force the mass to move in the opposite direction. When the mass motion reverses, the pressure inside the cavity will eventually rarify, opposing the outward motion of the mass. The resonance frequency of the oscillation, which can be derived from analogy with the mechanical, second-order system, is a function of the geometry of the cavity, neck, and lip/orifice, in addition to the speed of sound (e.g., see Kinsler *et al.*, 1982), as given by the following equation:

$$\omega_o = c\sqrt{\frac{S}{l'V}} \tag{1.1}$$

where ω_o is the angular resonance frequency, c is the speed of sound at ambient temperature, S is the neck cross-sectional area, V is the cavity volume, and l' is the effective neck length (given by $l' = l + \delta$; where l is the neck length and δ is an end correction accounting for the additional mass motion at the outer and inner ends of the neck).

The above equation (also known as the Rayleigh equation) generally works well for estimating the resonance frequency provided that the wavelength of sound is much larger than any of the dimensions of the resonator; the cavity dimensions are of the same order in all three spatial directions, and the neck is centered above the cavity. Chanaud (1994) utilized lumped-parameter models in conjunction with solutions to the wave equation to derive analytical expressions for the resonance frequency of resonators with asymmetrically placed orifices, asymmetric cavities, and extreme geometric shapes.

Chanaud (1994) discovered that resonance-frequency calculations obtained from the Rayleigh equation worked well for thin orifices that are centered on cubical cavities (referred to as "symmetric condition"). Chanaud (1994) then concluded that the Rayleigh equation has strong limitations on its validity with extreme changes in the resonator's geometry from the symmetric condition.

Another important aspect of Helmholtz resonators relates to their behavior when driven at high-intensity sound levels. In this regard, Ingard and Labate (1950), Ingard and Ising (1967), and Lebedeva (1980) presented significant results concerning acoustic streaming and acoustic non-linearity in the vicinity of the resonator's orifice. Especially interesting is the research done by Ingard and Labate (1950), where smoke-particle visualization of the acoustical streaming (steady flow) phenomena in the vicinity of

orifices with different geometrical parameters were recorded. Ingard and Labate (1950) classified the streaming flow patterns into four distinct regions of flow based on the particle velocity in the orifice. These four regimes will be discussed in detail in section 3.2. Here, it is noted that the Ingard and Labate (1950) study clearly demonstrated the existence of *steady* flow patterns that are produced in the vicinity of the resonator's orifice as a result of driving the actuator at high intensity of sound. Such steady flow pattern cannot be modeled with the simple mechanical system shown in Figure 1.2, which can only account for linear effects. However, as will become clear in Chapter 3, this streaming flow is the key for the success of the flow excitation device developed in this study.

1.3 Motivation

Numerous studies have previously been done on control of the separated flow over a classical backward-facing-step geometry. Of these, only one study (Liu *et al.*, 2005) employed wall-pressure sensor array for the investigation of the space-time characteristics of the surface-pressure field beneath an excited separating/reattaching flow downstream of "two-dimensional" (rectangular) backward-facing step. Moreover, in all of the existing investigations, in a back-step or other separated-flow geometry, the actuation device produces substantial acoustic noise at the same frequency as that of actuation. Consequently, noise from the control device and the wall-pressure signature of the excited flow structures are both picked up by the wall microphones, and cannot be separated by frequency filtering. Therefore, there is a need for an actuator with an acoustic signature that does not overlap with the excitation frequency of the flow.

1.4 Objectives

The specific objectives of the present study may be summarized as follows:

1. To develop an actuator/actuation-scheme (specifically, an externally-driven Helmholtz resonator) that is suitable for studies of the surface pressure beneath oscillatory-controlled flows. The actuator is required to produce flow disturbances at the edge of the back step of an axisymmetric model that are capable of altering the global (overall) characteristics of the separation bubble. Moreover, disturbances to the flow from the actuation device should be at a frequency that is different from any acoustic noise emanating from the device.
2. To characterize the operation of the driven Helmholtz resonator using measurements of the unsteady pressure at the neck and within the cavity of the resonator, and velocity measurements as well as visualization of the flow in the vicinity of the neck.
3. To characterize the overall effect of forcing by the Helmholtz resonator on the separation bubble through mean-wall-pressure measurements.
4. To conduct a preliminary investigation of the wall-pressure fluctuations beneath the separation bubble under natural and forced conditions utilizing wall-pressure-array measurements. In particular, to be examined are measurements of the RMS pressure fluctuations, power spectra, and frequency-wavenumber spectra.

2 EXPERIMENTAL SETUP AND METHODOLOGY

This chapter provides description of the experiments, measuring instruments, and test procedure employed in the present study. The experiments conducted may be classified into two main categories based on their goal. The first type of experiments targeted the characterization of the *acoustic* and *fluidic* response of the flow excitation device (i.e., the externally-driven Helmholtz resonator). The second type of tests aimed to characterize the influence of the excitation device on the wall-pressure field beneath the separating/reattaching shear layer. This characterization includes both the mean- and fluctuating-pressure field. To conduct both types of experiments, three measurement techniques were used. More specifically, microphones were used for measurement of acoustic and hydrodynamic pressure fluctuations; static-pressure taps, coupled with a pressure scanner and high-sensitivity pressure transducer, were employed to capture the mean-pressure field beneath the separated flow; and hotwires provided the flow-velocity data for capturing the fluidic response of the resonator. In the following chapter, these techniques along with the experimental procedure are described in detail. This is done following the description of the facilities and test model.

2.1 Experimental setup

The experimental setup includes the wind-tunnel facility, axisymmetric test model with the backward-facing-step (BFS), and all of the instruments used during the experiments, along with their calibration processes.

2.1.1 Wind-tunnel facility

The wind-tunnel facility used here consists of five parts: contraction, test section, pre-diffuser, diffuser, and axial fan. A 15 HP DC wound shunt GE motor with adjustable speed controller drives the fan. A schematic of the wind tunnel may be seen in Figure 2.1.

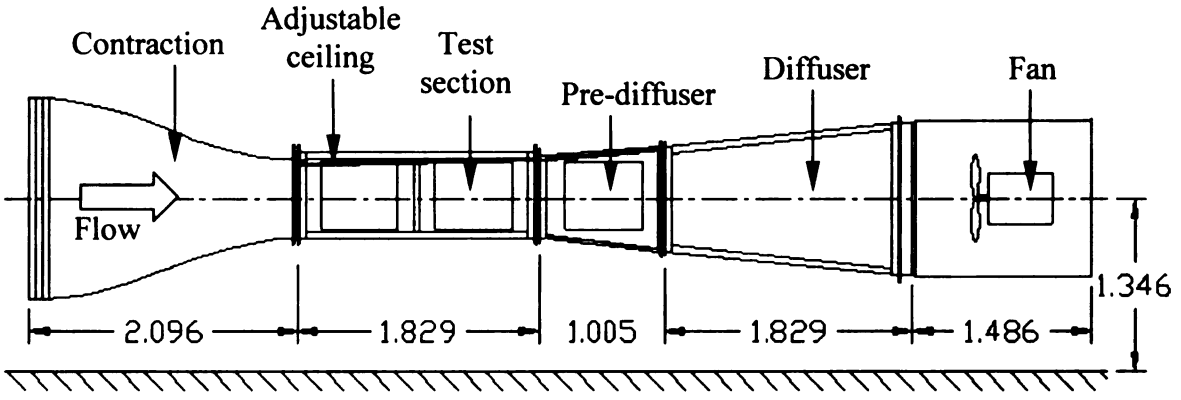

Figure 2.1. Schematic of the wind tunnel (dimensions in meter)

The total length of the wind tunnel is slightly more than 8 meters and the test-section-centerline height is nominally 1.35 meters from the floor. The contraction has 6.25:1 area ratio with the cross section at the inlet being 1.524 m × 1.524 m in width and height. Precision honeycomb and variable-porosity screens are mounted at the front end of the contraction to reduce the turbulence intensity of the airflow in the test section to less than 0.5% at freestream velocities up to 15 m/s.

The test section has an inlet area of 0.6096 × 0.6096 m^2 with an adjustable ceiling to achieve a nominally zero, pressure gradient in the freestream. The ceiling also has two slots, along its centerline, with 12.7 mm width to allow insertion of instrumentations (e.g., hotwire traversing mechanism, Pitot tube, etc.). The side and lower walls of the test section consist of acrylic windows inserted into sanded-plywood panels that are coated with transparent polyurethane to ensure smoothness of the surface. Four acrylic windows supported by aluminum frames, two on each of the sides of the test section, are attached using hinges and clamps to the tunnel to allow for easy access to the test model inside the tunnel.

Similar to the test section, the pre-diffuser also has an adjustable ceiling to avoid any discontinuity in the tunnel walls between the test section and the pre-diffuser section. Except for this adjustable ceiling, the walls of the pre-diffuser diverge at an angle of 6°. Additionally, the floor has a 50 mm wide slot that is used as a pass-through for the test model's support plate. The downstream end of the pre-diffuser is then connected to the diffuser directly. The diffuser has an expansion angle of 5.88° and an inlet-to-outlet area ratio of 1:1.9 to recover the pressure drop across the test section.

2.1.2 Backward-facing-step (BFS) test model and flow-excitation device

The BFS model has an axisymmetric geometry and is supported by a heavy traverse table that allows for adjustment of the yaw and pitch angles as well as the height, and lateral position of the model. The centerline of the model is aligned with the center of the inlet area of the test section. The length of the model extends from ≈ 0.3 m downstream of the test section entrance to near the downstream end of the pre-diffuser

section, as seen in Figure 2.2. In the following, more specific details are provided concerning the geometry of the model and the Helmholtz resonator employed to excite the separated flow.

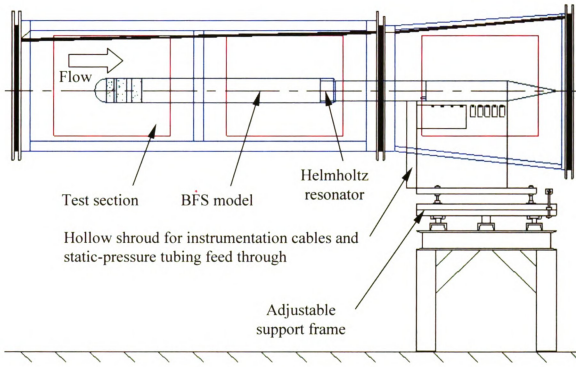

Figure 2.2. General schematic of the BFS axisymmetric model inside the wind tunnel

2.1.2.1 Cylindrical (axisymmetric) model

The axisymmetric model has a total length of 2.38 m (see Figure 2.3) and is mostly made of aluminum tube with wall thickness of 6.35 mm. The nose of the model has a half-sphere shape and is made of aluminum as well. Downstream of the nose and upstream of the step, the model has a diameter of 124.4 mm. Downstream of the step, the diameter decreases to 100.0 mm, creating a step height, H, of 12.2 mm. The step is at the

downstream end of an acrylic component, or module, that forms the step *and* contains the Helmholtz resonator (description of this module is given in the next subsection, 2.1.2.2).

Piano wires with nominally 1 mm in diameter are used to support the front end of the model to avoid the "cantilever deflection" associated with the long overhang of the model. These wires are located nominally 0.10 m downstream of the tip of the nose and pass through narrow slots in the side and bottom acrylic windows of the test section near its entrance. Outside the test section, the piano wires are connected to a supporting framework with fair amount of tension. Li (2004) found the wires to have no interfering effect on the separated flow. This was demonstrated through hotwire measurements around the perimeter of the model just upstream of the step.

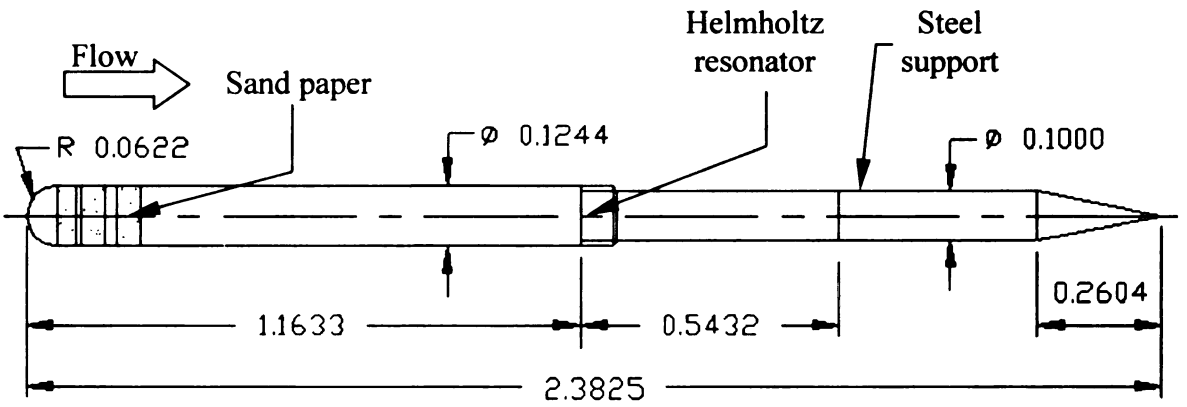

Figure 2.3. BFS axisymmetric model with Helmholtz resonator (dimensions in m)

Three aluminum-oxide, wet-cut, 120 grit, sand paper strips were adhered to the model surface at the upstream end (just downstream of the nose) of the model to hasten the transition of the boundary layer to a turbulent state. Finally, the tail end of the model has a conical shape to ensure that there is no sudden changes in geometry that might create undesirable disturbance to the overall flow structures around the model. For

additional details about the model geometry, its internal construction, etc., the reader is referred to Chapter 8.2 (appendix) of Hudy (2005).

2.1.2.2 Flow excitation device: externally-driven Helmholtz resonator

To form the resonator's cavity volume, a 3.175 mm-thick acrylic cylindrical shell and a 6.35 mm-thick acrylic cover were assembled around the model just downstream of the existing step in the model as shown in Figure 2.4. The streamwise location of the cover was adjusted, using gage shims, to maintain a uniform slit opening, d, of 0.5 mm around the model's perimeter. The corresponding slit height (or resonator's neck length, l) was 3.175 mm. Because it is well established in the literature (e.g., Greenblatt and Wygnanski, 2000, and Chun and Sung, 1996, 1998) that the most effective unsteady forcing of a separated flow is achieved very near the point of separation, the resonator's slit was made to coincide with the back-step edge. This was accomplished by the creation of a 45^{o} chamfer in the cover, on the downstream side of the slit as depicted in Figure 2.4.

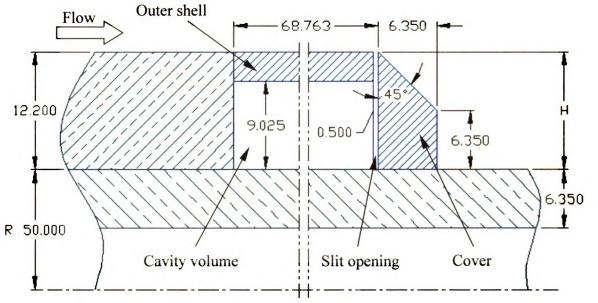

Figure 2.4. Half-sectional schematic of the Helmholtz resonator (dimensions in mm)

To mount the resonator on the model, it was necessary to make both the shell and the cover out of two halves that were aligned using dowel pins and were assembled around the model as depicted in Figure 2.5. Once assembled, the two halves were held together using a 63.5 μm-thick Kapton (Polyimide) film tape with silicone adhesive. Four acrylic brackets were utilized to support the shell portion of the resonator (Figure 2.6). These brackets occupied a very small fraction of the cavity volume in order to minimize their influence on the device's resonance frequency. After considering the four support brackets, the cavity volume was found to be nominally 202,304 mm^3.

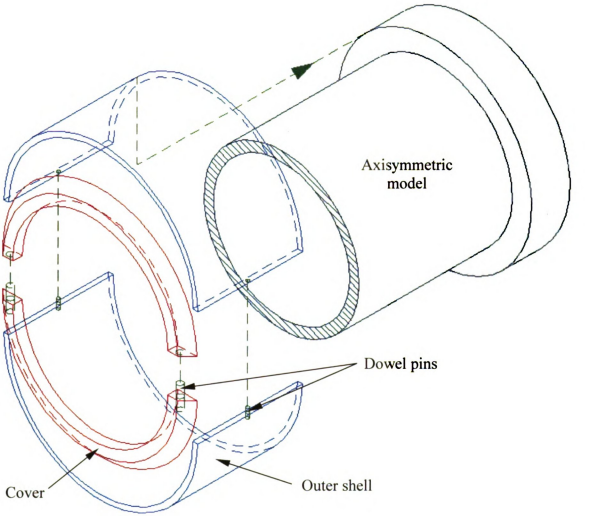

Figure 2.5. Helmholtz resonator assembly on the axisymmetric model

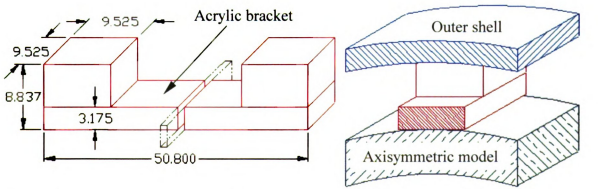

Figure 2.6. A schematic of one of the resonator's support brackets: isolated bracket (left), and assembled on model (right) (dimensions in mm)

To predict the resonance frequency of the resonator, Equation 1.1 is used, in connection with an end correction (δ) that is given by (e.g., see Kinsler *et al.*, 1982):

$$\delta = 1.7r \qquad \text{(outer end flanged)} \qquad (2.1a)$$

$$\delta = 1.5r \qquad \text{(outer end unflanged)} \qquad (2.1b)$$

where r is the radius of the neck opening (taken here as the radius of a circle with the same area as that of the current resonator's slit). The Helmholtz resonance frequency was calculated to be 425 Hz and 447 Hz when employing Equations 2.1a and 2.1b respectively for the end correction. These values are quite far from the actual resonance frequency of the device of 657 Hz (see section 3.1). This is not too surprising since Equations 2.1a and 2.1b work well for symmetric cavity geometry (similar dimensions in all three dimensions) with centered circular neck. The present resonator's geometry deviates substantially from this simple geometry, with its approximately rectangular (when unwrapped), high-aspect-ratio (width/height) cavity, and off-center, rectangular neck. Ingard (1953) derived analytical expressions for the end correction of the neck length of various resonators' geometrical shapes.

Of these shapes, the square cavity with rectangular neck provided the closest approximation to the geometry of the present resonator (although this does not account for the high-aspect-ratio of the cavity and the eccentricity of the neck). Calculation of the resonant frequency based on the results of Ingard (1953) for the square cavity yields a resonant frequency of 585 Hz. Although this new prediction remains significantly far from the true frequency (about 11% deviation), it is substantially better than that based on

the simplest resonator geometry (equations 2.1). It is suspected that if the high aspect ratio of the resonator and eccentricity of the neck were taken into account, the proper frequency value would be predicted. However, no analytical solutions that account for these factors were found.

During operation, external sound waves at the resonance frequency were used to excite the resonator, as will be described in section 2.1.3.5. In response, large oscillation of the air mass within the neck of the device was produced, creating an energetic unsteady air jet in the immediate vicinity of the point of separation. The coupling of this jet to the flow field is what ultimately leads to the manipulation, or control, of the separation bubble and associated wall-pressure field.

2.1.3 Instrumentations and their calibration

The next several subsections provide a description of the instrumentation used for the experiments and their calibration processes. The instrumentation include microphones, hotwire anemometry, static-pressure-measurement system, Pitot tube and temperature sensors, along with other hardware such as the subwoofer/speaker utilized in driving the Helmholtz resonator, and the data acquisition hardware.

2.1.3.1 Microphones

There are three common types of microphones: capacitive, electret, and piezoresistive (micro-fabricated) microphones. Capacitive and electret type microphones have a wide frequency response (a typical bandwidth is 3 Hz – 70 kHz for ¼" capacitive microphone), and very good sensitivity. They are capable of detecting pressure

fluctuation levels that are well below one millionth of standard atmospheric pressure. On the other hand, the piezoresistive type has a frequency response that is comparable with that of capacitive and electret microphones on the high-frequency end, but it can extend to DC (zero frequency) on the low-frequency end. The piezoresistive sensors also tend to have sensitivity that is one or two orders of magnitude lower than a comparable size capacitive and electret microphones. Therefore, piezoresistive microphones are generally suitable for measurements of high-level pressure fluctuations and when information on the mean pressure (zero frequency) is desired.

For low-speed flows, such as the case in the present study, the wall-pressure fluctuations are on the order of fraction of a Pascal. This very low level of pressure fluctuations eliminates the possibility of utilizing piezoresistive sensors because of their relativity low sensitivity. Additionally, to achieve high spatial resolution and to minimize the cost of the microphones, Emkay (model FG-3629-P16) electret microphones were utilized for measuring the surface pressure. These sensors also have a very compact package size that allowed them to be integrated into test model within the available space.

In addition to the Emkay microphones, a stand-alone electret Panasonic microphone was used to sense the sound pressure imposed on the Helmholtz resonator. A summary of the characteristics of both types of microphones and other relevant information is provided below.

2.1.3.1.1 Panasonic microphone

The Panasonic microphone used here is an omnidirectional back electret condenser microphone (model P9925-ND). It has a nominal manufacturer sensitivity of

–35 ± 4 dB (relative to 1 V/Pa; i.e., nominally 18 mV/Pa) for a frequency range of 20 to 20,000 Hz. The overall dimensions of this microphone cartridge are as follows: outside diameter is 6.0 mm and length is 3.4 mm. The sensing diaphragm of the microphone is exposed to the sound field through a 2 mm-diameter sensing hole covered with a thin, sponge-type material. This microphone cartridge is mounted in a homemade PVC and brass tubing to provide means for holding the microphone (Figure 2.7). The resulting probe length is 104 mm. The microphone cartridge is slip fitted into the PVC tubing and made flush at the tube opening. The outside of the PVC tubing was machined such that the probe would fit into the mounting hole of a Larson-Davis microphone calibrator (model CAL 200) for determining the sensitivity of the Panasonic microphone on daily basis. The brass tube is press fitted into the PVC on the opposite end of the microphone and held together by epoxy around its circumference to ensure rigid construction.

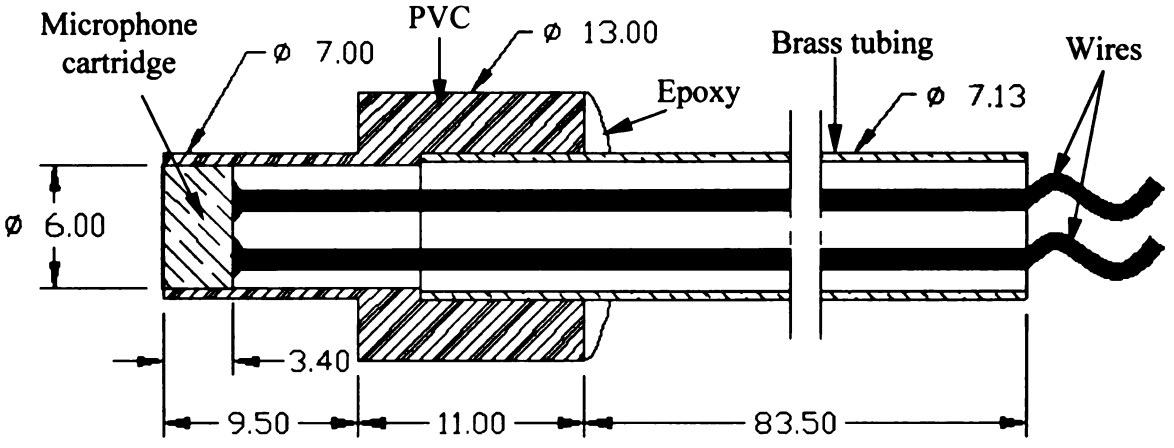

Figure 2.7. Panasonic microphone probe (dimensions in mm)

To operate the microphone, it was connected to one of the ports of a 16-channel homemade, electrical circuit. Details of the circuit, which is powered by a 9 V, DC power supply, is provided in Daoud (2004). The output signal of the microphone was

connected to one of 16 channels of a National Instrument A/D board (model NI 6024E) through a two-channel, Larson-Davis signal conditioner (model 2200 C) to remove any DC offset from the output signal. The microphone was calibrated using the Larson-Davis precision acoustic calibrator at 114 dB and 1000 Hz. Typically, the resulting sensitivity of the microphone was found to be 14.8 mV/Pa or –36.6 dB (relative to 1 V/Pa).

2.1.3.1.2 Emkay microphones

In the study by Hudy (2005), a 32-sensor array of Emkay (model FG-3629-P16) microphones was constructed and integrated into the axisymmetric, back-step model in order to measure the space-time signature of the wall-pressure fluctuations downstream of the step. Each of the microphones has a nominal manufacturer sensitivity of –53 ± 3 dB (relative to 10 V/Pa; i.e., nominally 22.4 mV/Pa) for a frequency range of 100 to 100,000 Hz. The actual sensitivity value for the individual microphones was obtained by Hudy (2005), where these microphones were bench calibrated using a B&K (model 4226), multifunctional calibrator in the frequency range between 20 and 15,000 Hz. The outside diameter of the microphone cartridge is nominally 2.6 mm. The sensing diaphragm of the microphone is exposed to the sound field through a 0.77 mm-diameter sensing hole.

The present investigation utilized only part (15 sensors) of the same microphone array for capturing the unsteady wall-pressure field downstream of the resonator. The remaining microphones were not utilized for the same purpose since they were either contained within the volume of the resonator, or located downstream of the measurement extent of interest. However, one of the microphones contained within the resonator's

cavity was used to measure the sound pressure within the resonator, and hence determine the resonator's acoustic response. Figure 2.8a provides a photograph showing the placement of the microphones relative to the resonator.

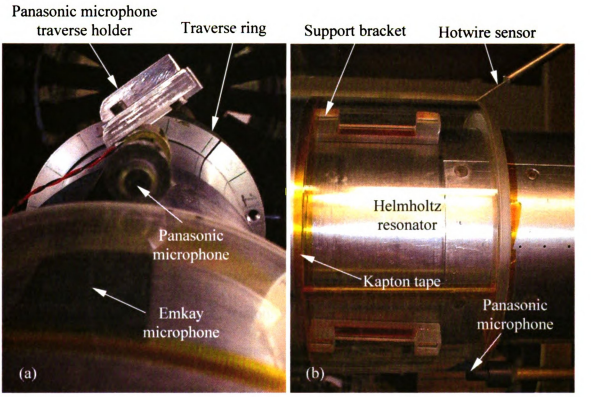

Figure 2.8a-b. Photograph of Panasonic, Emkay, and hotwire sensors: (a) Panasonic microphone mounted on an azimuthal traverse mechanism, and (b) hotwire sensor at $y = 0$ (within the resolution of the measurement) above slit opening

Note that the first, most upstream, microphone utilized in the measurements of the flow-induced pressure fluctuations is located 11.73 mm downstream of the resonator cover's sharp orifice (i.e., the step). The rest of the microphones have a distance of 4.8 mm centerline-to-centerline between each other. This microphone array was used to sense the unsteady pressure induced by the flow structure downstream of the separation point.

2.1.3.2 Hotwire anemometry

A single, hotwire probe was used to measure the velocity within the oscillatory jet produced by the forced resonator. The hotwire sensor was made from Tungsten wire with a diameter of 3.75 μm. The wire was electroplated in a copper-sulphate solution to define a sensing length (un-plated portion) of 0.78 mm. This provides a wire length-to-diameter ratio of more than 200:1. The plated wire is soldered to the tip of two stainless steel prongs of the hotwire probe, which is nominally 300 mm long and has an outside diameter of 5.56 mm. In turn, the prongs are soldered to lead wires that are threaded through the length of the probe body and terminated with a SMA – coaxial connector for coupling to the anemometer circuit. A schematic of the hotwire probe may be seen in Figure 2.9.

Constant Temperature Anemometer (CTA) from TSI (model 1750) that was powered by a 15-Volts, Elenco Precision, variable, power supply (model XP – 581) was used to operate the single-hotwire sensor. The resistance of the hotwire was typically 4.80 Ω and the overheat ratio was set to 1.62. The output of the CTA was split into two paths: one that was connected directly to one of the analog-input channels in a National Instrument A/D board (model NI 6024); the other one was routed through a two-channel, Larson-Davis signal conditioner (model 2200 C) to remove the mean voltage and amplify the fluctuating signal using a gain of 10. This mean-removed/amplified signal allowed better digitization resolution of the unsteady velocity information. In the processing of the hotwire signal, the unconditioned voltage time series was averaged to yield the mean voltage. The mean-removed/amplified one was divided by the gain factor then added to the mean voltage to retrieve a digitized record of the full hotwire output. Note that the

cut-off frequency of the high-pass filter of the Larson-Davis signal conditioner was 1.6 Hz. This is well below any of the frequencies associated with the measured velocity fluctuations, and hence the signal conditioning process should not lead to the loss of any relevant information.

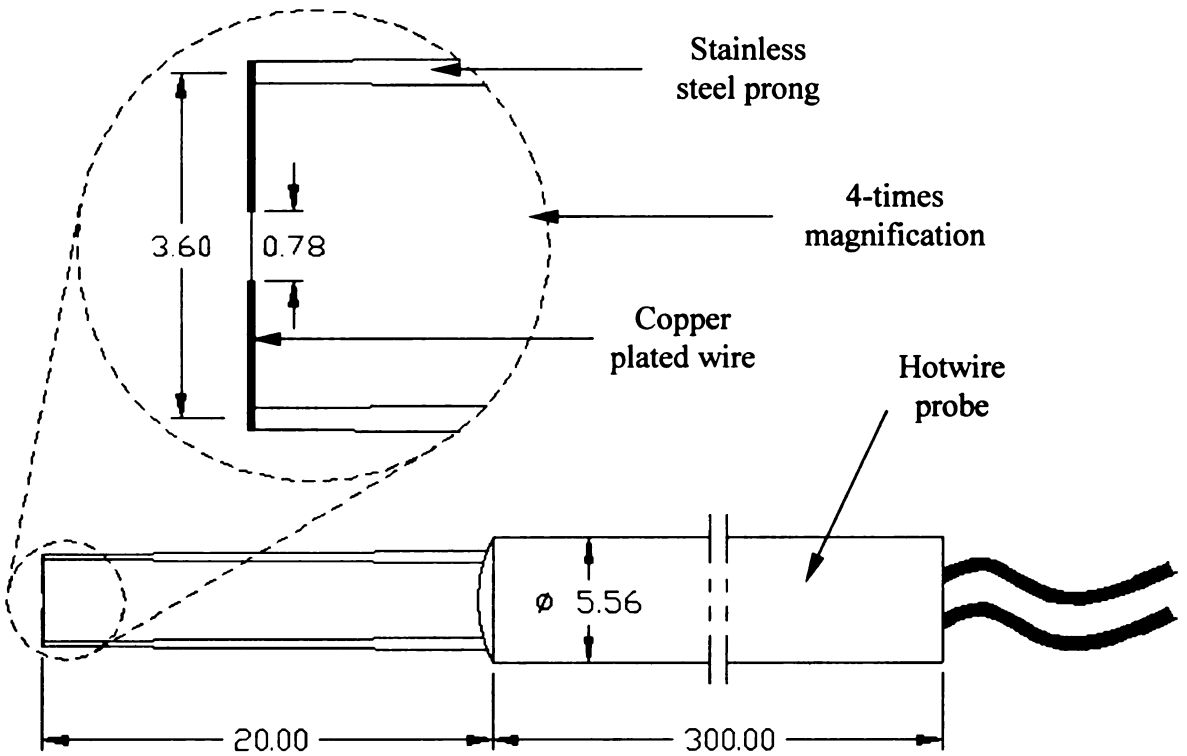

Figure 2.9. Hotwire probe (dimensions in mm)

During the experiments, the hotwire probe was held by aluminum mounting bracket that was connected to a traversing mechanism via a tube that passed through the slot in the ceiling of the test section. This traversing mechanism was driven by TMG, Hybrid Stepper Motor (model 5618 S – 0105) coupled with TMG, MS 2.0 series, quad-step controller. The latter was driven by an 8-bit digital I/O interface integrated into the NI 6024E multi-purpose A/D card. The whole assembly of the stepper motor unit was

located outside the test section. The resolution of the stepper motor/traversing-mechanism system, which was calibrated using a 12.7 μm resolution Starrett dial indicator (model 25-631), was found to be 0.824 μm per motor step (where one full revolution of motor shaft corresponds to 800 steps). To position the hotwire sensor accurately relative to the resonator's slit, a digital imaging system was utilized. The system consisted of a Sony (model XC-75) Charge Couple Device (CCD) video camera connected to a PC-driven, National Instruments, IMAQ frame grabber (model PCI-1411). A Nikkor 500 mm (model NH – 27) lens was utilized for capturing images of the hotwire tip near the resonator opening. A Steady Lite, high-intensity, lighting manufactured by Stocker & Yale, Inc. (model 13 Plus Lite Mite® Series) is used to illuminate the imaging region of the hotwire tip and the lip of the resonator. A sample of a captured image is depicted in Figure 2.10.

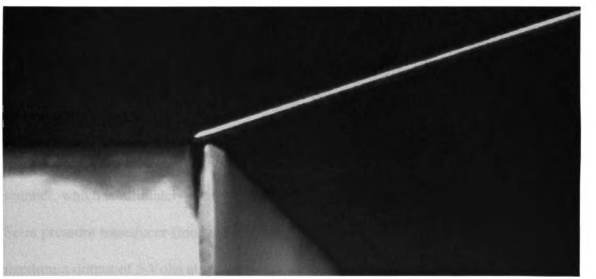

Figure 2.10. A sample image used in positioning the hotwire sensor near the resonator's slit

2.1.3.3 Mean-pressure measurements

Static-pressure-taps coupled with an appropriate pressure transducer were used for measuring the mean-pressure distribution beneath the separating/reattaching flow. There are four arrays of static pressure taps: one on the north (top) side of the model, two on the east and west sides, and one on the south side. The array on the north side consists of 27 pressure taps exposed to the flow while the other three sides have 7 pressure taps each. The north static pressure taps lay along side the Emkay microphone array at the same spatial distance of 4.8 mm from centerline-to-centerline with the first pressure tap located 11.73 mm downstream of the sharp edge of the resonator's cover.

The static-pressure taps were connected to polyurethane pressure tubing that were threaded inside the axisymmetric model and came out through a half-rounded, hollow shroud attached to the vertical steel support plate of the model. The other ends of the tubing were connected to 48 input ports on a rotary, solenoid-driven, pressure scanner (model 48D9 – 1346 from Scanivalve). The rotary solenoid was driven by a homemade solenoid-actuation circuit that was, in turn, controlled using one of two analog-output channels available from the NI-6024E general-purpose, data-acquisition board. The analog channel was used to generate a 0 – 5 Volts transition to step the scanner from one static-pressure port to the next. The selected port connects to the output port of the scanner, which is ultimately connected to a low-range (0 – 12.7 mm H_20, or 0 – 124.7 Pa) Setra pressure transducer (model 239 – XW 211). The transducer's output is linear with maximum output of 5 Volts at full-scale pressure.

2.1.3.4 Pitot tube and temperature sensor

A $^{5}/_{16}$ -inch diameter Pitot tube manufactured by Dwyer Instrument Inc. (model 160-12) was used for measuring the freestream velocity in the test section. The device was inserted into the test section through the slot in the ceiling with tube's static-pressure ports located nominally 20 mm upstream of the step. The pressure ports of the Pitot tube were connected to either a 0 – 13.3 Pa, or 0 – 133.3 Pa, Baratron pressure transducer (model 223-B) depending on the flow velocity. In either case, the output of the Baratron pressure transducer is in the range of 0 – 1 Volt. The Pitot tube measurements were used to set the freestream velocity to the desired value, and monitor its stability during the experiments. In addition, the tube was used to calibrate the single hotwire sensor.

The temperature of the air in the test section was also measured in order to calculate the air density for Pitot tube velocity measurements as well as for correction of the hotwire signal for temperature effects. The temperature sensor employed was manufactured by Omega (model DP-25-TH), which provides an analog output signal for sampling by the computer. In addition, the sensor has an LED panel that gives instantaneous readouts for monitoring by the operator during the experiments. The sensor was of the thermistor type and had a sensitivity of 0.1 Volt/°C.

2.1.3.5 Helmholtz resonator driving system

As discussed previously, the Helmholtz resonator was driven by imposing a sound field external to the device. This was accomplished using a 0.381 m diameter, 450-Watts, Eminence LLC subwoofer (model Kappa 15) with 0.3496 m baffle-hole diameter. The

subwoofer was located at the centerline of the contraction, nominally 2.3 m upstream of the intake (see Figure 2.11).

A two-channel, 110-Watts/channel, power amplifier manufactured by Hafler (model Trans-ana P 1000) was used to drive the loudspeaker. The two channels of the amplifier were "strapped" together; i.e., connected in parallel, to operate the speaker at power levels up to 220 Watts. The input signal to the amplifier was provided using two Hewlett Packard function generators (model 33120A), the output of which was summed together. The adoption of two function generators enabled the generation of amplitude-modulated excitation of the Helmholtz resonator.

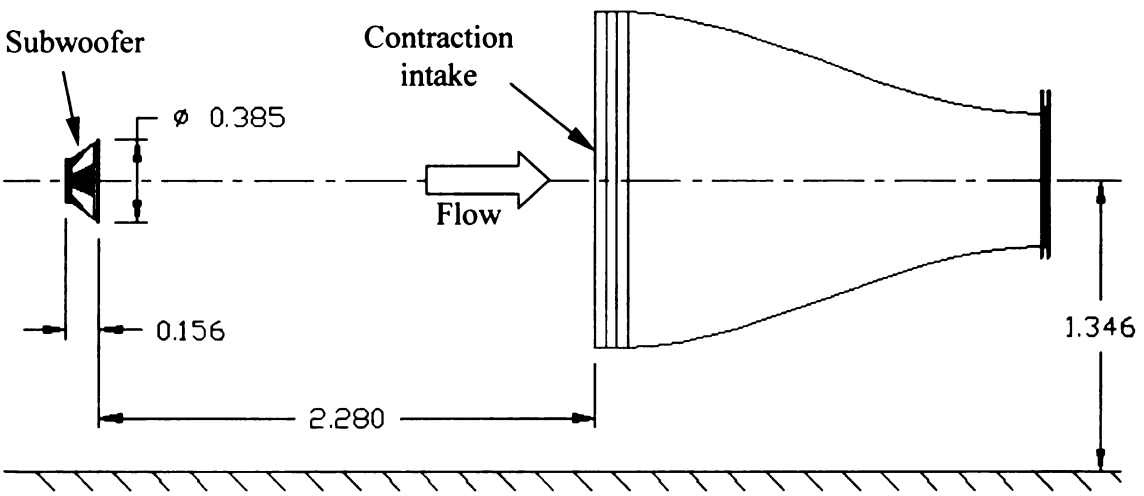

Figure 2.11. A schematic showing the subwoofer location relative to the wind tunnel intake (dimensions in meter)

The need for employing amplitude-modulated, rather than pure-harmonic excitation stems from the mismatch between the resonance frequency of the forcing device (630 Hz: see section 2.2.3) and the frequency range of the inherent flow instability (i.e., the range in which the unsteady excitation affects the flow). In particular, the latter

is more than an order of magnitude lower than the former. Since, it was not possible to employ a Helmholtz resonator with sufficiently low resonance frequency to match that desired by the flow (the resonator's volume would be prohibitively large), seeding of low-frequency disturbances into the flow was accomplished through low-frequency amplitude modulation of the high-frequency excitation signal of the device. As will become clear in Chapters 3 and 4, the success of this strategy is related to the establishment of a "streaming" (i.e., steady) velocity component at the resonator's opening when exciting the resonator with high-intensity harmonic sound. Subsequent modulation of the harmonic sound causes this steady flow to oscillate at the low frequency of modulation, thus coupling effectively to the flow. Equally significant is the fact that the generated low-frequency *fluidic* disturbance is at much lower frequency than the acoustic signal driving the resonator. Therefore, the flow disturbance occurs at a frequency that is different from the acoustic noise produced by the excitation scheme.

Although it is possible to generate an amplitude-modulated signal from a single function generator, there are some *subtle* issues relating to the acoustic response of the wind tunnel that led to the use of two function generators. More specifically, mixing (i.e., multiplication) of two sinusoidal signals was used in the present study to form the amplitude-modulated signal. Such a signal, say $z(t)$, is given by the following equation:

$$z(t) = Z \sin(2\pi f_m t) \sin(2\pi f_c t) \tag{2.2}$$

where t is time, Z is the signal amplitude, f_m and f_c are the modulation and carrier frequencies respectively, and no phase difference is assumed between the two sinusoids

because of its insignificance to the present analysis. Employing trigonometry, Equation 2.2 can be rewritten as:

$$z(t) = \frac{Z}{2}\left[\cos 2\pi(f_c - f_m)t - \cos 2\pi(f_c + f_m)t\right] \tag{2.3}$$

Equation 2.3 shows that a harmonic signal with frequency f_c that is modulated with frequency f_m can be created by adding two harmonic signals with frequencies $(f_c - f_m)$ and $(f_c + f_m)$. However, the amplitude of the two signals must be equal.

If a single function generator is used to generate a modulated signal such as that given by Equation 2.2, this would be equivalent to seeding the wind tunnel with two sound waves at frequencies of $(f_c - f_m)$ and $(f_c + f_m)$ and equal amplitude. However, because of the dependence of the tunnel acoustic response on frequency, the two waves may be preferentially amplified and/or attenuated as they propagate through the tunnel. Furthermore, reflection of the waves from the laboratory walls creates a standing-wave component within the tunnel, leading to spatial dependence of the sound wave amplitude, which in turn is dependent on the wave frequency. The net result of these effects is that, *at the location of the resonator slit*, the two seeded waves may not have equal amplitude. In the extreme case, when one is substantially attenuated relative to the other, a pure harmonic, rather than amplitude-modulated, excitation of the Helmholtz device is produced. In other more moderate situations, where the two signals are of comparable but not equal magnitude, modulation is achieved but not with the desired strength. As described above, the ability to excite the flow relies on the modulation signal, and

therefore the ability to control the modulated-forcing-component strength properly is important.

The employment of two function generators to produce the amplitude-modulated signal remedies the problem described above by allowing independent adjustment of the amplitude of each of the sound wave components. In this case, one of the function generators is used to produce a harmonic signal at a frequency of $(f_c - f_m)$ while the other one produces the other harmonic component with frequency $(f_c + f_m)$. The two signals are then added together using a summation circuit before they are fed to the power amplifier. To set the amplitude of each of the two signals, the Panasonic microphone is placed at the resonator's opening to monitor the incident sound wave. The amplitude of one of the waves is kept constant and that of the other is adjusted. This is done while monitoring the microphone output signal on the oscilloscope until a good-quality amplitude-modulation signal is observed. Subsequent adjustment to the forcing-signal strength at the given carrier and modulation signal frequencies is accomplished by equally amplifying the two signals.

Figure 2.12 provides a block diagram of the entire driving system. Note that the combined signals were sampled by the A/D board in various experiments to provide a reference for the forcing-signal phase. In addition, the signal is fed into a homemade low-pass filter powered by a couple of Imation, AC/DC adaptor power supplies (model JOD 48U–08). The low-pass filter was utilized only when broadband sound was generated for obtaining the frequency response of the resonator. In this case, a white noise signal was fed from one of the function generators to the power amplifier. The filter helped to limit the bandwidth of the white noise to that desired (to avoid subsequent

aliasing of the digitized data records). Finally, certain characterization tests of the resonator required the use of pure harmonic signals. In this case, only a single function generator was employed as the source of the driving-signal.

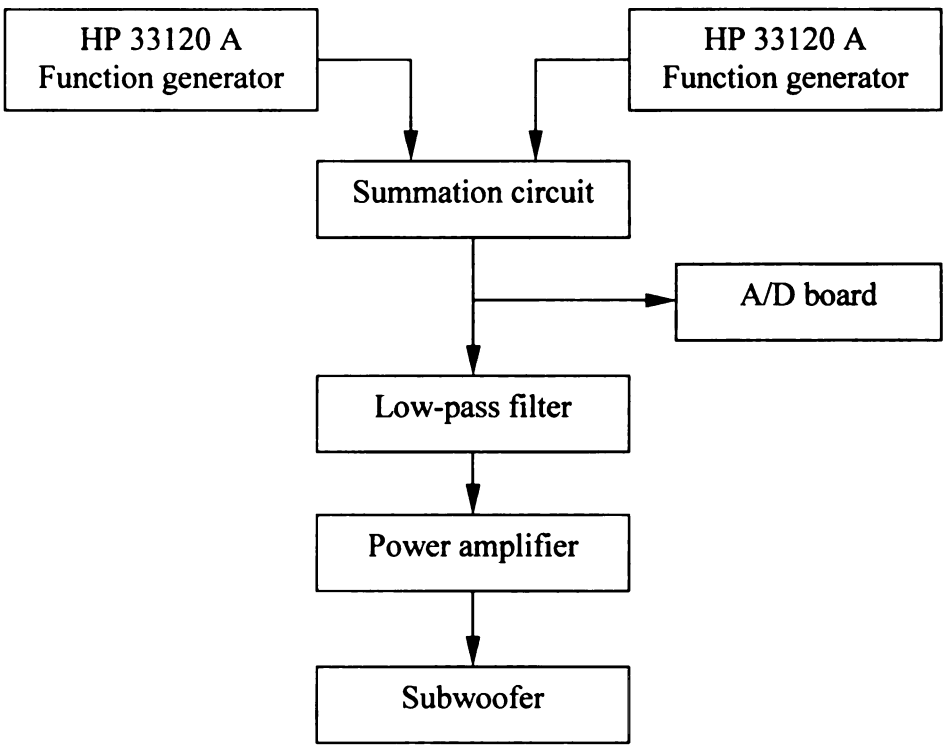

Figure 2.12. Block diagram of the Helmholtz-driving system

2.1.3.6 Data-acquisition and experiment-control hardware

As briefly discussed in the previous subsections, there are two different computer-based-data-acquisition boards used for the experiments. The main data acquisition board is a PC-based National Instrument A/D board (model NI 6024E). This board is equipped with 16 single-ended analog-input channels and has a maximum sampling frequency of 12,500 Hz per channel if all channels are consumed. Because the channels were multiplexed, a systematic error in the sampled data could occur due to an average inter-

channel time delay. However, this error is relatively small, 5 μs, and has negligible effect on the measurements compared to the flow convective time scale, 318 μs, over a distance equal to sensor (i.e., microphone) spacing. The board was used for various measurements that included velocity, pressure, and temperature. In addition, the board was also used for driving the stepper motor unit connected to the hotwire traversing mechanism.

The other data acquisition hardware is a PC-based, National Instruments, IMAQ frame grabber (model PCI-1411). This frame grabber was mainly used for capturing close-up images of the hotwire in order to position it with good accuracy relative to the resonator's opening. The board is capable of capturing video image frames in real time, converting them into digital format using an 8-bit, flash, analog-to-digital converter.

2.2 Experimental methodology

This section includes a categorization of the experiments conducted along with a summary of the data acquisition parameters, followed by a description of the procedure of those experiments.

2.2.1 Experiments categorization and data acquisition parameters

The experiments may be categorized into three different topics: test-model alignment, Helmholtz resonator characterization, and mean- and unsteady-wall-pressure measurements for examination of the flow-forcing effect on the surface-pressure field beneath the separated/reattaching flow.

In all the experiments, two-different sets of data-acquisition parameters were utilized depending on whether time-resolved information or only statistical quantities are to be obtained. In the former case, the sampling frequency, f_s, was set to 8,000 Hz and the total number of samples, N, was 262,144 or 2^{18}. The sampling frequency was well above the largest frequency (nominally 1 kHz) where any significant signal fluctuation existed in order to avoid any aliasing during the digitization of data. In addition, the number of points was large enough to attain proper resolution of the lowest frequency of interest, while providing sufficient number of data sub-records for reducing scatter in the calculation of frequency spectra.

The above parameters were used for all except the mean-pressure measurements, where f_s was set to 1,500 Hz and N was 15,000 samples. This rendered a 10-second average of the pressure, which was long enough to obtain a stable average at all static-tap locations. The A/D board input range used was either ±5 or ±0.5 Volts, depending on the

signal level. When coupled with the board's resolution (12-bit), the larger range provides a voltage resolution of 2.44 mV. The lower range reduces this value by an order of magnitude, which was particularly important for measurements of the mean-pressure and the resonator's unsteady-jet velocity at low levels of excitation.

2.2.2 Model alignment

The test model was aligned parallel to the freestream direction prior to installing the resonator on the model. This was done by adjusting the model's support frame and the tension of the four piano wires at the upstream end of the model. Initially, the model surface was set parallel to the sidewalls and floor of the test section using tape measure, ruler angle, and level. This was regarded as coarse adjustment with additional fine-tuning of the model's alignment conducted based on the mean-pressure distribution around the model.

As described earlier in section 2.1.3.3, there are four, static-pressure-tap arrays located downstream of the step. Azimuthally, these arrays are positioned on the top and bottom (indicated as the north and south here), and both sides (east and west) of the model. A plot of the streamwise distribution of the mean-pressure coefficient (C_p) obtained from the four arrays may be seen in Figure 2.13. Note that the streamwise coordinate is normalized by the step height (H) and that C_p is given by the equation:

$$C_p = \frac{(P_x - P_\infty)}{\frac{1}{2}\rho_{air}U_\infty^{\,2}} \tag{2.4}$$

where P_∞ is the freestream pressure, P_x is the pressure measured at each of the pressure taps surrounding the model, ρ_{air} is the density of air, and U_∞ is the freestream velocity.

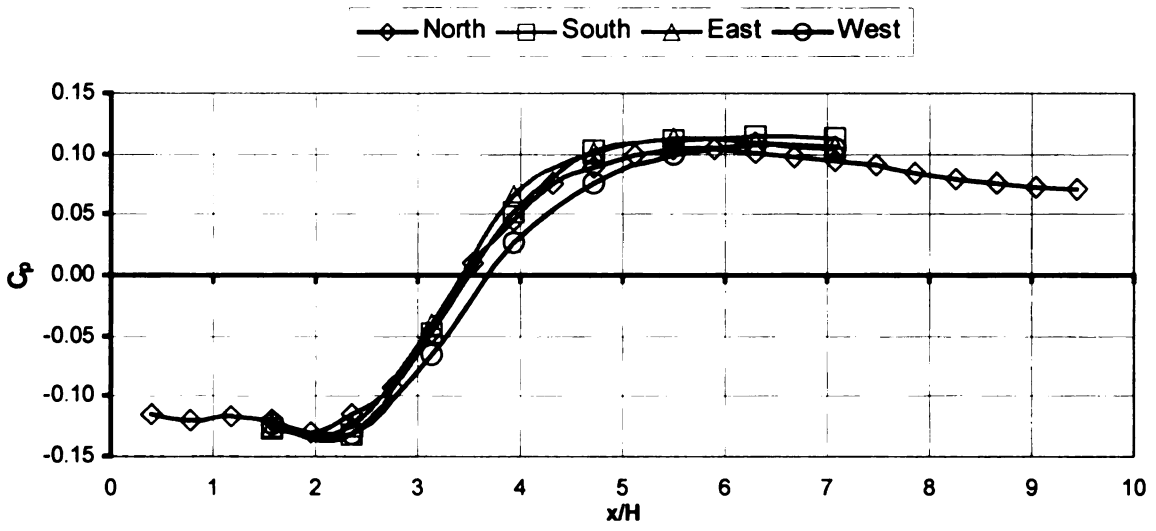

Figure 2.13. Streamwise distribution of C_p at four different azimuthal locations

As seen from Figure 2.13, the mean-pressure distributions at all four azimuthal locations seem to collapse up to nominally $x/H = 3$. Downstream of this location the largest deviation is found near $x/H = 4$. This deviation (relative to an average of all four values at a given x position) is about 10% of the overall pressure variation within the separation bubble.

2.2.3 Helmholtz resonator characterization

Both broadband (white noise) and harmonic sound waves were used to characterize the Helmholtz resonator. The broadband signal was utilized in tests directed towards obtaining the frequency response of the resonator. The main goal of these tests was to identify the resonance frequency of the device, and to verify that the behavior of

the device may be approximated by that of a second-order system (as expected from a Helmholtz resonator). In addition, these experiments were also employed to verify the azimuthal uniformity of the incident sound field. On the other hand, the harmonic test signals were primarily employed to determine the *fluidic* response of the resonator. That is, these tests rendered information on the strength of the unsteady jet produced by the resonator at different locations away from the slit, and for different forcing levels. In the following, more detailed description of each of the tests is provided. Note that all the tests were conducted without flow in the tunnel.

For the broadband tests, the Panasonic microphone was placed in the immediate vicinity of the resonator's slit, as illustrated earlier in Figures 2.8a-b, in order to measure the acoustic input that drives the resonator. The Panasonic microphone was mounted on a traverse ring that was attached to the model and allowed for measurement of the input sound at different azimuthal angles while maintaining the same location relative to the resonator's orifice. The traverse ring is made of two aluminum halves held together by two dowel pins and tape. This ring was assembled around the model such that the center of the ring coincides with the center of the axisymmetric model. The tests were performed at sixteen different azimuthal angles, starting from 22.5°, relative to the top of the model, to 360.0° in 22.5° increments.

To measure the response (output) of the resonator to the input sound, the pressure inside the resonator's cavity was acquired using the Emkay microphone embedded inside the resonator (see section 2.1.3.1.2). This rendered the *acoustic* response of the device. Additionally, the hotwire was located slightly (y = 0.034 mm; corresponding to 2 pixels in the image captured by the CCD camera used for the hotwire positioning) above the slit

opening, where for the remainder of the discussion will be referred as $y = 0$ (within the resolution of the measurement), and at the slit opening's center line in order to capture the *fluidic* output of the device (i.e., the velocity oscillations associated with the air mass movement within the neck of the resonator). Figure 2.8b provides a photograph showing the placement of the hotwire relative to the resonator. To position the hotwire above the resonator, images of the hotwire at different locations were captured. First, the hotwire was positioned as close as possible to the resonator's slit. Then the hotwire probe was traversed upward in the wall-normal direction at known increments. Concurrently, an image was captured for every hotwire position and a corresponding dial indicator (manufactured by Starrett – model 25-631) reading of the traversing system movement was recorded. The captured images were then processed using MATLAB software to obtain the number of pixels that the hotwire moved for each increment and correlate this with the actual distance traveled by the hotwire in order to arrive at the imaging scale factor. After averaging for all incremental movements, this factor (which is also the measurement resolution) was found to be nominally 17.2 μm/pixel.

For the broadband tests, four channels of data were acquired: two for the hotwire signal (unconditioned and mean-removed/amplified), one for the Panasonic microphone, and one for the Emkay microphone located inside the resonator. Before activation of the sound field, measurements of the background noise were conducted. This was done in order to verify that, once the sound was activated, the signal-to-noise ratio was sufficiently high to render the response of the device. As will be seen in Chapter 3, that this was in fact true for the entire frequency range of interest when determining the

acoustic response of the resonator. On the other hand, the *fluidic* response could only be obtained within a narrow frequency band around the resonance frequency of the device.

A similar setup was utilized for the harmonic tests. In this case, however, the Panasonic microphone's azimuthal location was fixed at an angle of 180° relative to the top of the model (see Figure 2.8b). Also, in addition to sampling four channels of data as described above, the sound source signal from the function generators was captured to provide a reference for the forcing signal phase. Table 2.1 summarizes all data acquisition parameters employed for both the broadband and harmonic tests. Note that all harmonic tests were conducted at a frequency of 630 Hz. This corresponds to the frequency at which the unsteady resonator's jet was the strongest for a given sound input. It is interesting to point out that this frequency was somewhat smaller than the resonance frequency of the resonator (which was 657 Hz). The reason for this difference will become clear in Chapter 3.

Table 2.1. Data acquisition parameters for broadband and harmonic tests

Channel	Channel descriptions	Broadband test	Harmonic test
Ch. 10	Panasonic microphone	± 0.5 Volts	± 0.5 Volts
Ch. 11	Function generator	Shorted	± 5.0 Volts
Ch. 12	Unconditioned hotwire	± 5.0 Volts	± 5.0 Volts
Ch. 13	Amplified hotwire	± 0.5 Volts External gain of 10	± 0.5 Volts External gain of 10
Ch. 14	Emkay microphone	± 0.5 Volts	± 0.5 Volts
Number of samples, N		262,144	262,144
Sampling frequency, f_s		8000 Hz	8000 Hz

When utilizing a pure harmonic signal to drive the resonator, three different tests were conducted. First, the location of the hotwire was kept at $y = 0$ above the slit opening and data was acquired for seven streamwise locations spanning a distance of slightly more than the slit width (see Figure 2.14 for demonstration of the location of the measurements relative to the slit). This test was used to identify the location within the slit where the velocity fluctuations are the largest. Subsequently, a second test was conducted where the hotwire was positioned at this location and the forcing level (imposed sound amplitude) was changed. In particular, five different levels of forcing were considered. These forcing levels corresponded to a sound-pressure-level (SPL) of 98.1 dB, 102.6 dB, 107.3 dB, 109.3 dB, and 111.7 dB based on the RMS pressure.

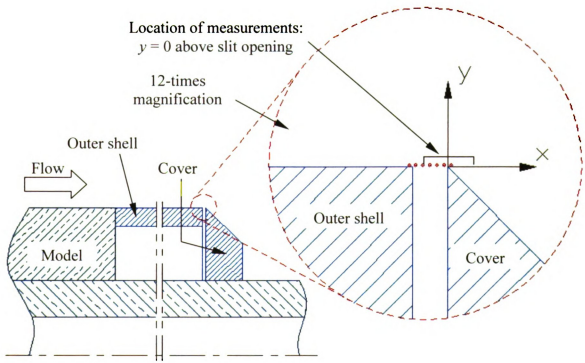

Figure 2.14. Location of the hotwire measurements across the slit opening

Finally, a third test was conducted where the sound level was kept at the highest value and the hotwire was used for measurements at different locations in the wall-normal (y) direction. Starting with an initial location of y = -0.055 mm relative to the surface of the slit opening, the hotwire was traversed in increments of 0.10 mm up to 0.945 mm above the surface of the slit opening.

2.2.4 Mean- and unsteady-wall-pressure measurements

Mean-pressure measurements were undertaken for both unforced and forced flow conditions. The unforced, or natural, case was done first to produce a benchmark. Subsequently, the mean-pressure distribution was acquired when forcing the flow at five different modulation frequencies (i.e., 10 Hz, 15 Hz, 18 Hz, 20 Hz, and 25 Hz) with a carrier frequency, f_c, of 630 Hz. As will become clear in Chapter 4, since 18 Hz produced the strongest effect on the flow, the mean-pressure distribution was also measured for different forcing levels for this particular frequency to observe the effect of forcing strength on the mean-pressure distribution. During the measurements, the freestream dynamic pressure was also acquired with each static-tap measurement to account for any small variation in the tunnel velocity when calculating the mean-pressure coefficient. All of data were acquired at an average freestream velocity, U_∞, of 3.25 m/s.

While the mean-pressure information is useful in examining if the flow excitation is pronounced enough to produce a global effect on the average flow behavior (i.e., affecting the entire separation bubble behavior and not merely the shear layer), the unsteady surface-pressure measurements would yield information that is related to the alteration of the turbulent structures. The energetic flow structures leave a wall-pressure

imprint as they advect downstream. Therefore, alteration of the flow structures behavior via the forcing should also lead to corresponding change in the space-time characteristics of the wall-pressure. To investigate the latter, the fifteen-Emkay-microphone array described in section 2.1.3.1.2 was used for measuring the instantaneous wall-pressure signature downstream of the resonator.

Because microphones are sensitive to the *hydrodynamic* pressure fluctuations (i.e., that produced by the flow structures) as well as the *acoustic* pressure fluctuations produced by speaker driving the Helmholtz resonator, it was desired to document the latter by conducting measurements for all the forcing conditions without flow. Subsequently, these measurements were also repeated for a freestream velocity of 3.25 m/s.

The forcing conditions for which microphones data were compiled corresponded to a carrier frequency of 630 Hz, two modulated frequencies of 10 Hz and 18 Hz, and two different forcing levels. Note that because the dynamic range of the microphones is limited to about 130 to 140 dB SPL, it was not possible to conduct the measurements at the "higher" forcing levels as the output of the microphones would "clip". In general, the speaker-generated sound dominated the microphone measurements. However, because of the amplitude-modulated excitation, the sound and hydrodynamic signals were in two widely separated frequency bands. Specifically, the sound signal was confined to the two frequencies $(f_c - f_m)$ and $(f_c + f_m)$, while the hydrodynamic signal was at $2f_m$ (and not f_m as will become clear in Chapter 3). Since f_c is more than an order of magnitude larger than f_m, it was possible to effectively separate the acoustic and turbulent components using frequency-domain filters. The latter was implemented during the post processing of data.

3 CHARACTERIZATION OF THE HELMHOLTZ RESONATOR

This chapter contains three sections that provide details of the data analysis, and discussion of the results pertinent to characterizing the Helmholtz resonator. The first section contains material related to the acoustic and fluidic response of the resonator. This is followed by qualitative and quantitative characterization of the resonator's fluidic disturbance under pure-harmonic forcing conditions in the second section. Finally, the third section contains further study of the resonator's fluidic disturbance under modulated-forcing conditions.

In order to characterize the Helmholtz resonator, several analyses were conducted. These are summarized here in order to familiarize the reader with the details of the signal processing prior to presentation of the results. First, the Power Spectrum Density (PSD) of various discrete-time measurement signals was obtained by means of the Fast Fourier Transform (FFT). PSD yields information about the distribution of the "energy" of the signal over different frequencies, allowing one to identify the dominant frequencies in a signal (i.e., frequencies at which large fluctuations take place). The one-sided PSD for a signal $b(n)$, where n is the discrete-time index (or sample number), is given by the following equation:

$$\phi_{bb}(k) = \begin{cases} \dfrac{B(k) \times B^*(k)}{N^2} & ;k = 0, \dfrac{N}{2} \\ \dfrac{2 \times B(k) \times B^*(k)}{N^2} & ;k = 1,2,\ldots,\dfrac{N}{2}-1 \end{cases} \tag{3.1}$$

where, ϕ_{bb} is the discrete PSD, $B(k)$ is the FFT of $b(n)$, $B^*(k)$ is the complex conjugate of $B(k)$, k is the discrete-frequency index, and N is the number of data points in the time

series. Note that to obtain the physical frequency value corresponding to a particular value of k, the latter is multiplied by the spectrum resolution $\Delta f = f_s/N$ (where f_s is the sampling frequency). It is evident from Equation 3.1 then that the largest frequency in the one-sided spectrum is the Nyquist frequency, or $f_s/2$.

A second quantity of interest is the cross-spectrum. Specifically, this quantity is useful in obtaining the response of a system from measurements of its input and output, as will become clear later. This was utilized for characterization of the forcing-device response from measurements of the Panasonic microphone's signal, or resonator's input, while employing the Emkay microphone and hotwire to capture the acoustic and fluidic, respectively, disturbance as the system's output. Unlike the power spectrum analysis that helps find the dominant frequencies in a signal, the cross-spectrum analysis offers information regarding the correlation between two different signals for different frequencies. The one-sided, discrete-frequency, cross-spectrum was calculated from the equation below for two signals, b and g, where definitions of various symbols are similar to that given earlier for Equation 3.1.

$$\phi_{gb}(k) = \begin{Bmatrix} \dfrac{G(k) \times B^*(k)}{N^2} & ;k = 0, \dfrac{N}{2} \\ \dfrac{2 \times G(k) \times B^*(k)}{N^2} & ;k = 1,2,\ldots,\dfrac{N}{2} - 1 \end{Bmatrix} \tag{3.2}$$

The magnitude and phase responses, respectively, of the Helmholtz resonator, were obtained from the cross- and auto-spectrum results as follows (note that here b indicates the sound input to the resonator; i.e., that measured by the Panasonic

microphone, and g is the acoustic or fluidic output; i.e., that captured by the Emkay microphone and hotwire respectively):

$$|J(k)| = \left| \frac{\phi_{gb}(k)}{(\phi_{bb}(k) - \phi_{bb\_background}(k))} \right| \tag{3.3}$$

$$\angle J(k) = angle\left(\frac{\phi_{gb}(k)}{(\phi_{bb}(k) - \phi_{bb\_background}(k))} \right) \tag{3.4}$$

where $J(k)$ is the discrete-frequency, resonator's system function, and subscript background indicates the background noise measured by the Panasonic microphone without any deliberate sound excitation of the device.

Subtraction of the spectrum of the background noise from the input-sound spectrum helps to remove noise influences (including electronic noise as well) on the input signal when estimating the system, or transfer function. Noise influences on the output signal are accounted for by utilizing the cross-spectrum in the numerator of J instead of the auto spectrum of the output signal. These provisions help in improving the quality of the estimate. However, this does not alleviate the need to have a good signal-to-noise ratio at all frequencies of interest. Two measures were utilized here to gauge the signal-to-noise quality of the measured input and output signals. First, the auto spectrum of each signal with and without imposed sound field were compared to ensure that the latter was well below the former. Second, the coherence between the input and output

signals was checked to examine the phase-locking between b and g. The coherence (Γ_{gb}) was obtained from the cross-spectrum using:

$$\Gamma_{gb}(k) = \frac{\left|\phi_{gb}(k)\right|}{\sqrt{\phi_{bb}(k) \times \phi_{gg}(k)}} \tag{3.5}$$

Note that since the resonator is a deterministic system, the coherence between b and g should be equal to unity across all frequencies. Deviations from this value are due to phase variation associated with random noise. The associated reduction in Γ_{gb} depends on the relative magnitude of the random and deterministic signal components. Therefore, for the purpose of transfer function determination, a high value of coherence is desired. In the present investigation, a coherence threshold of 0.7, or 70%, was adopted to gauge the quality of the measurements at different frequencies.

Note that in calculating the power and cross-spectrum, the 262,144 points time series were sub-divided into 512 records of 512 points each. The spectra obtained from each of these records were then averaged yielding a frequency resolution of 15.625 Hz and random uncertainty of 4.4%.

3.1 Determination of the resonator's acoustic and fluidic response

The acoustic response of the resonator refers to the pressure fluctuations produced inside the resonator's cavity (p_c) in response to the acoustic pressure imposed on the outside of the slit, or neck (p_i). On the other hand, the fluidic response pertains to the unsteady fluid velocity at the slit opening of the resonator produced by the imposed sound.

To determine the response of the resonator over the entire frequency range of interest, white-noise sound input was utilized. This enabled excitation of all frequencies at once. The bandwidth of the white noise was limited to less than 4 kHz (the Nyquist frequency of the data acquisition) by feeding the function generator output through a low-pass filter before feeding it to the speaker's power amplifier. Figure 3.1 shows the power spectrum of the generated sound-field pressure just outside the resonator's slit. The different curves correspond to measurements conducted at sixteen different angles around the perimeter of the slit. Also included in the figure is the power spectrum obtained with the speaker turned off. This spectrum represents the background noise level, and therefore is denoted by "BG" on the spectrum plot. Also note that the results are plotted for frequencies up to 1 kHz only since higher frequencies are not of interest.

Inspection of Figure 3.1 shows that, overall, the imposed sound field at the lip of the resonator is azimuthally uniform up to a frequency of about 700 Hz (some narrow-band exceptions to this uniformity are found at nominal frequencies of 310 Hz, 565 Hz, and 670 Hz). The spectra depict multiple peaks that presumably correspond to resonances of the wind-tunnel test section, with the highest peak found at nominally 630 Hz. This frequency then corresponds to the largest achievable magnitude of the driving

pressure of the Helmholtz resonator for a given input-signal-amplitude to the speaker. Finally, consideration of the background-noise spectrum shows that, except at 360 Hz and 720 Hz, the imposed sound-pressure spectrum is more than one order of magnitude higher than the background noise. Therefore, the measured signal has an acceptable signal-to-noise ratio for utilization in determining the resonator's response.

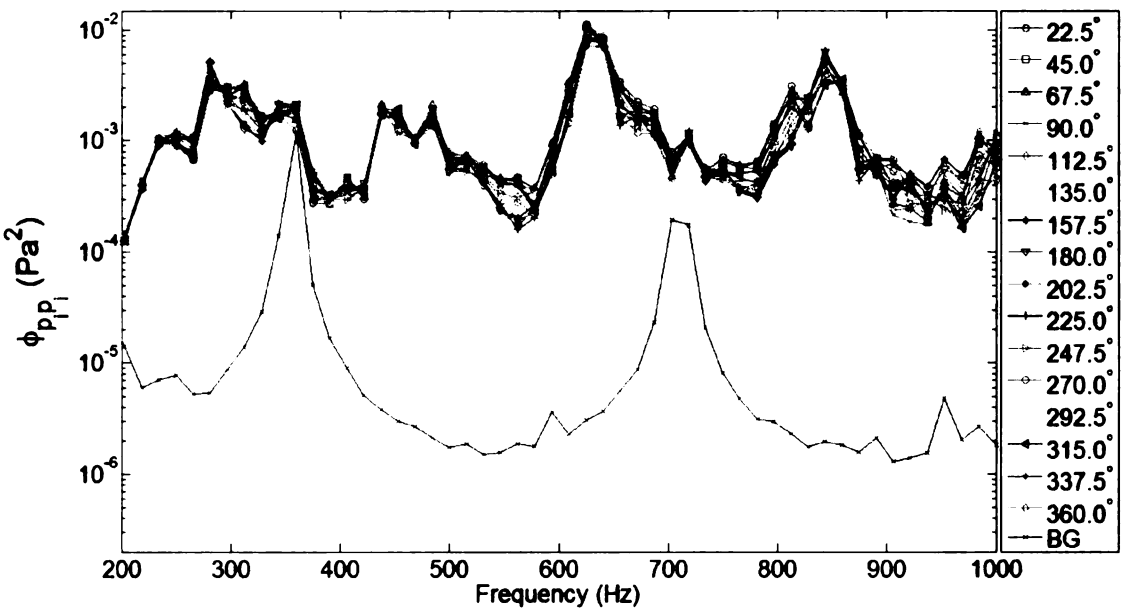

Figure 3.1. Power spectrum of the sound pressure just outside the Helmholtz resonator's slit for 16 different azimuthal angles

A similar plot to that shown in Figure 3.1 is given in Figure 3.2 for the pressure inside the cavity (p_c), which was obtained using the Emkay microphone. The data from the Emkay microphone were acquired simultaneously with the data from the Panasonic microphone. Therefore, there is one Emkay time series for each azimuthal position of the Panasonic microphone. However, since the Emkay microphone position did not change during the acquisition, the different-color data sets shown in Figure 3.2 may be used as an indication of the repeatability of the measurements.

Similar to the results in Figure 3.1, the highest spectrum peak is found to be at nominally 630 Hz for the cavity pressure. However, it is important to realize that this frequency does not necessarily correspond to the resonance frequency of the resonator. The highest peak observed in Figure 3.2 indicates that the strongest cavity-pressure fluctuations for a given input to the speaker are found at 630 Hz. Hence, this frequency corresponds to the resonance frequency of the *entire* system consisting of the power amplifier, speaker, wind tunnel and resonator. On the other hand, the resonance frequency of the resonator should correspond to the largest pressure fluctuation amplitude inside the resonator's cavity for a given sound-pressure amplitude imposed on top of the slit. Lastly, inspection of the background-noise spectrum (blue line in Figure 3.2) clearly shows that the measured sound pressure is one or more orders of magnitude larger than the background noise.

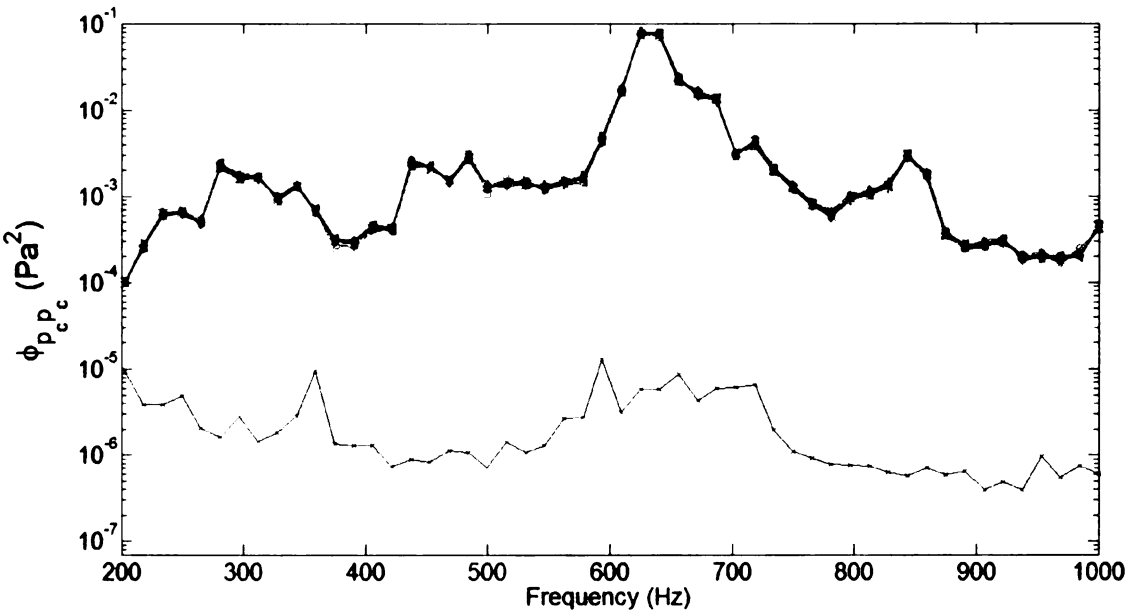

Figure 3.2. Power spectrum of the resonator's cavity pressure with and without (blue line) speaker excitation. Different line colors correspond to repeated measurements.

The fluidic response of the Helmholtz resonator is represented using the one-sided, power-spectrum plot shown in Figure 3.3. For all spectra shown, the hotwire was located at $y = 0$ (within the resolution of the measurement) relative to the slit opening of the resonator. It is noted that the representation of the data here is in volts (i.e., without conversion of the hotwire's output voltage to velocity). No calibration was conducted for this test since it does not influence the outcome of the analysis, which primarily aims at identifying the Helmholtz resonance frequency. Similar to Figure 3.2, the different color-coded curves correspond to repeated runs of the measurements, and the blue line (see arrow) denotes the background noise.

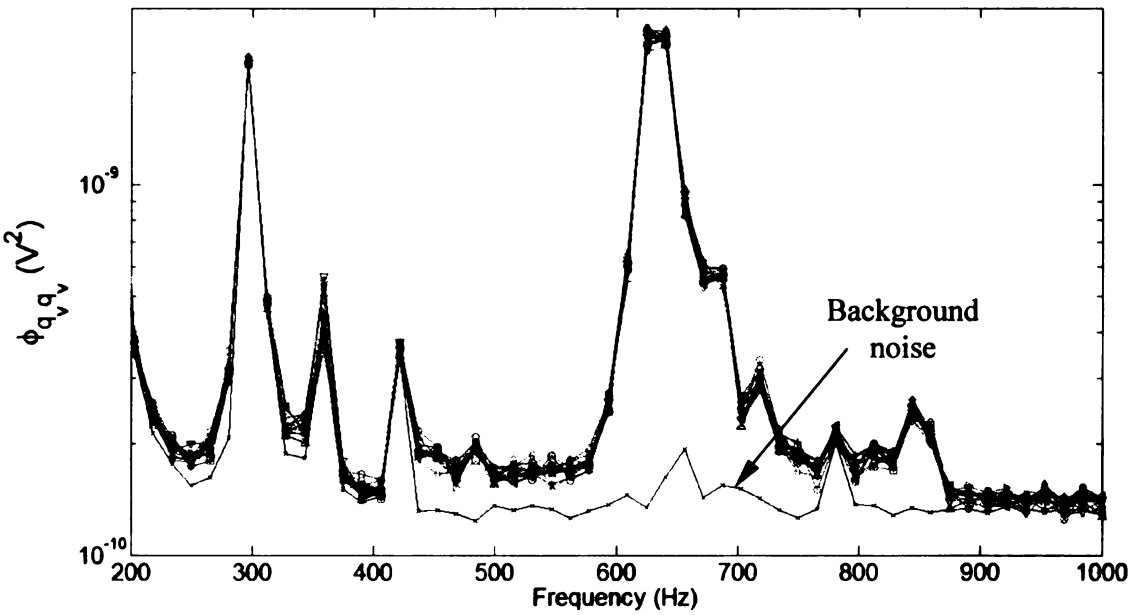

Figure 3.3. Power spectrum of hotwire sensor output

Several peaks can be identified in the spectra in Figure 3.3. The largest two peaks are found at nominal frequencies of 300 Hz and 630 Hz. However, the former frequency is clearly dominated by the background noise (this point will be reinforced using the

coherence analysis below). On the other hand, the peak at 630 Hz is more than an order of magnitude larger than the background noise, and hence this peak corresponds to actual velocity fluctuations produced by the coupling of the speaker-driven pressure fluctuations with the resonator. Unlike the pressure measurements, the velocity data seem to have large signal-to-noise ratio only within a narrow frequency band of 50 – 100 Hz that is in the vicinity of 630 Hz. Consequently, the fluidic response of the Helmholtz resonator can only be determined reliably within this band. The results suggest that the resonator is highly inefficient in generating velocity disturbances at frequencies that depart appreciably from the resonance frequency of the system.

As discussed earlier, coherence analysis was used to examine the phase-locking, and hence the signal-to-random-noise quality, between the Panasonic input signal, on one hand, and the Emkay and hotwire output signals, on the other. Based on Equation 3.5 above, the coherence could be calculated, and an arbitrary threshold of 0.7 or 70% was chosen to distinguish between good and poor phase-locking (coherence > 0.7 for the former). The results may be seen in Figure 3.4 when considering the Panasonic and Emkay signals. In the figure, different colors represent the different azimuthal angles (relative to the top of the model) at which the Panasonic microphone was located. With the exception of f = 360 Hz, the phase-locking quality between the acoustic input and output signal is quite good between 200 Hz and 700 Hz. This is true for all locations of the Panasonic microphone. At frequencies higher than 850 Hz, considerable scatter is found among the results obtained for different azimuthal locations. This indicates the poor axisymmetric quality of the incident sound filed at these high frequencies. However, since this frequency range was not utilized in the actual experiments, this was

of no concern. Along with the power spectrum analysis done previously, the coherence analysis demonstrates the high signal-to-noise ratio of the measurements within the frequency range of interest, and gives evidence of the deterministic coupling between the input and output acoustic signals.

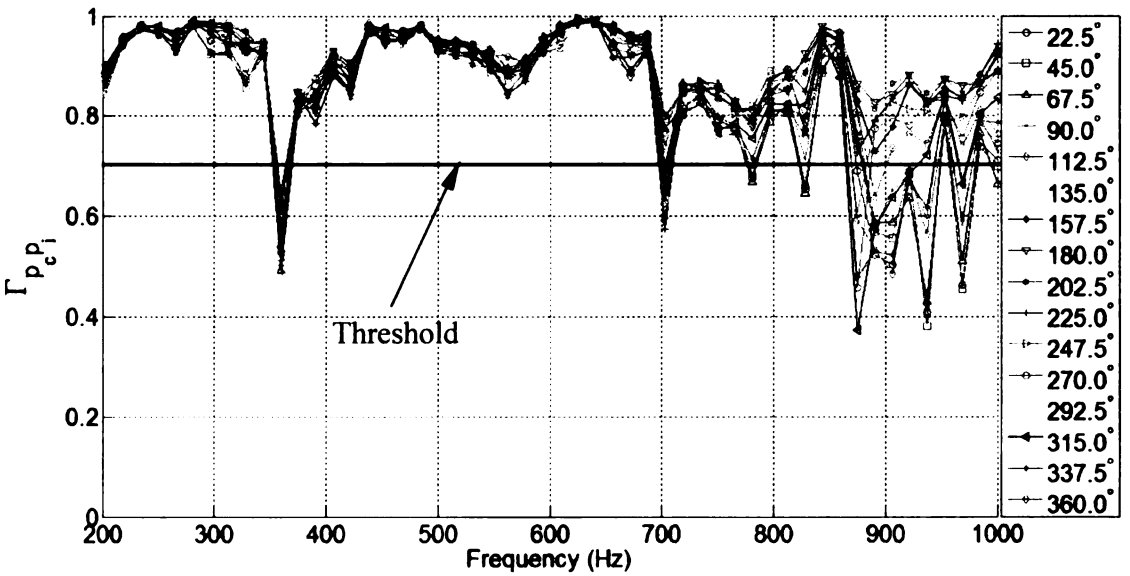

Figure 3.4. Coherence plot for the input and output acoustic signals of the resonator

A plot of the coherence between the acoustic input and fluidic output signals (i.e., that measured by the Panasonic microphone and hotwire sensor) is shown in Figure 3.5 below. Unlike the coherence between the Emkay and Panasonic microphones, the frequency range for good-quality phase-locking between the hotwire sensor and Panasonic microphone signals is found to be much narrower. Specifically, the frequency range with coherence value above 70% is seen to be confined between 600 Hz and 700 Hz only. Hence, outside this frequency band, the Helmholtz resonator's fluidic response

cannot be determined reliably. This implies that fluidic-response information will be limited to the vicinity of the system's resonance frequency.

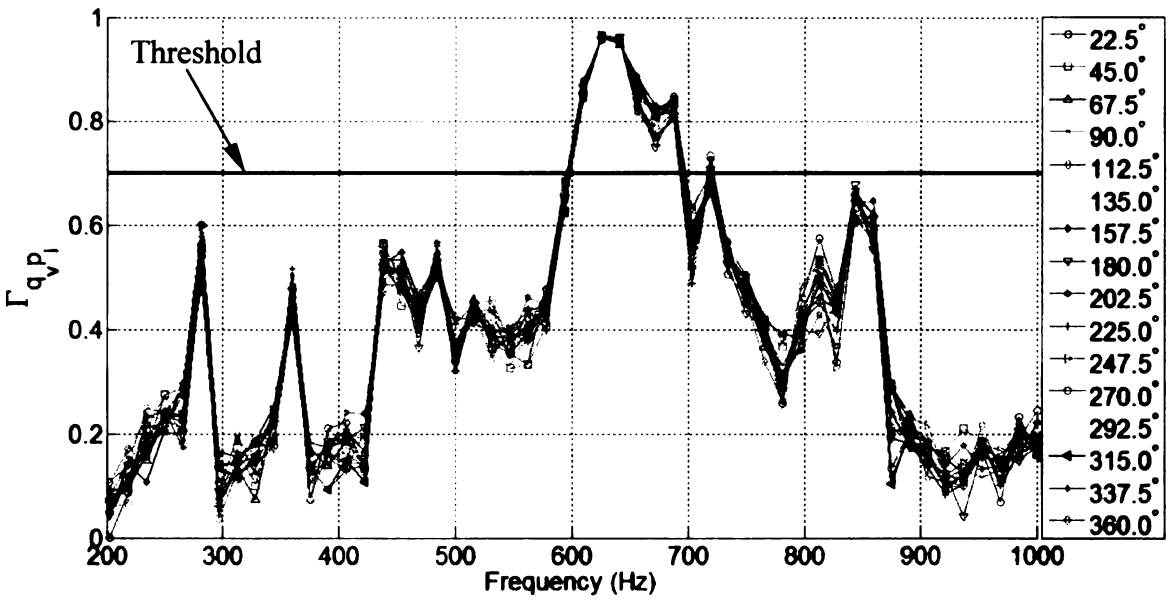

Figure 3.5. Coherence plot for the hotwire and Panasonic signals

The resonator's acoustic response determined from application of Equations 3.3 and 3.4 to the Panasonic and Emkay signals is shown in Figures 3.6 and 3.7 for the magnitude and phase, respectively. As previously noted, the different-color lines represent results obtained from different azimuthal locations of the Panasonic microphone. Additionally, the solid black lines in the figures display the theoretical response of a second-order, lumped-parameter, mechanical system for comparison purposes. The equations for this response are given by:

$$A = \frac{\left(\omega/\omega_o\right)^2}{\sqrt{\left[1-\left(\omega/\omega_o\right)^2\right]^2 + \left[2\zeta\left(\omega/\omega_o\right)\right]^2}} \tag{3.6}$$

$$\tan\Phi = \frac{2\zeta\left(\omega/\omega_o\right)}{1-\left(\omega/\omega_o\right)^2} \tag{3.7}$$

where ζ is the damping ratio and ω_o is the natural frequency. Note that for the curves shown in Figures 3.6 and 3.7, the values of ζ and ω_o were taken as 0.11 and 4151 rad/s (or 661 Hz), respectively. These values were not based on any curve fitting but rather on visual observation of the agreement between the measured and theoretical response. This is sufficient for the purposes of the discussion, which aims at examination of the consistency of the measured response with the second-order-system behavior.

Overall, the magnitude results in Figure 3.6 are consistent for all angles except at 360 Hz, where there is large scatter. This is not too surprising since the coherence is low at this frequency (refer to Figure 3.4). There is also some scatter at the resonance peak of about 15% relative to the mean response over all azimuthal locations. This number is reflective of the axisymmetric quality of the sound input to the resonator. For convenience, the experimental curves at all azimuthal angles were averaged and represented by solid red line. The behavior of this average seems consistent with that of the second-order system. This is confirmed further from consideration of the phase results where the 180-degree phase change characteristic of the behavior of a second-

order system is observed as the frequency increases from low values to values beyond the resonance frequency. The specific value of the resonance frequency is found to be 657 Hz.

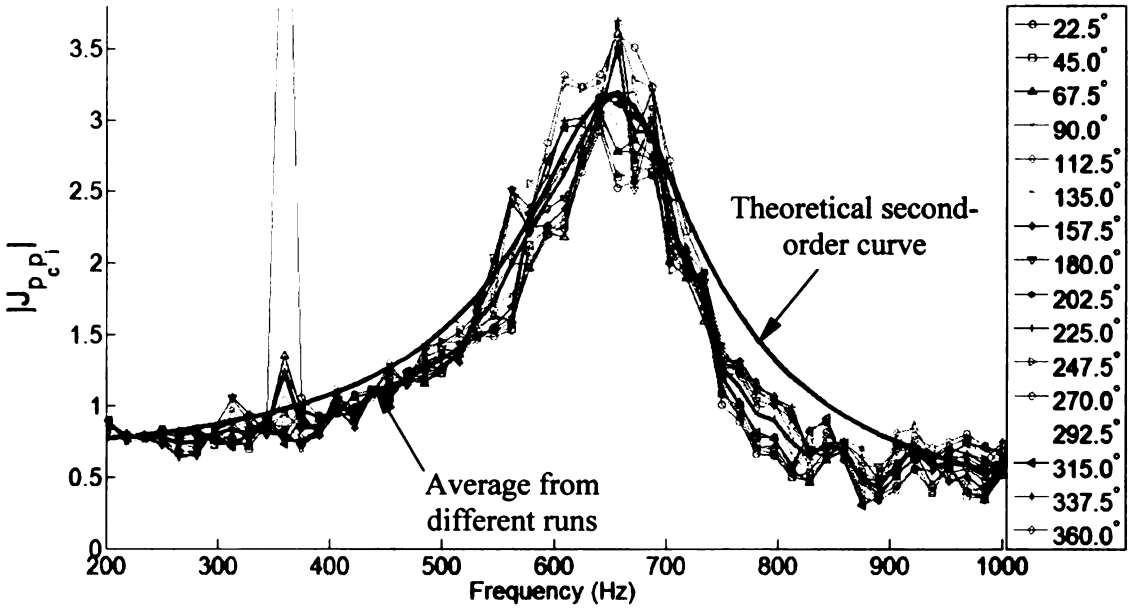

Figure 3.6. Magnitude of the acoustic system function of the Helmholtz resonator

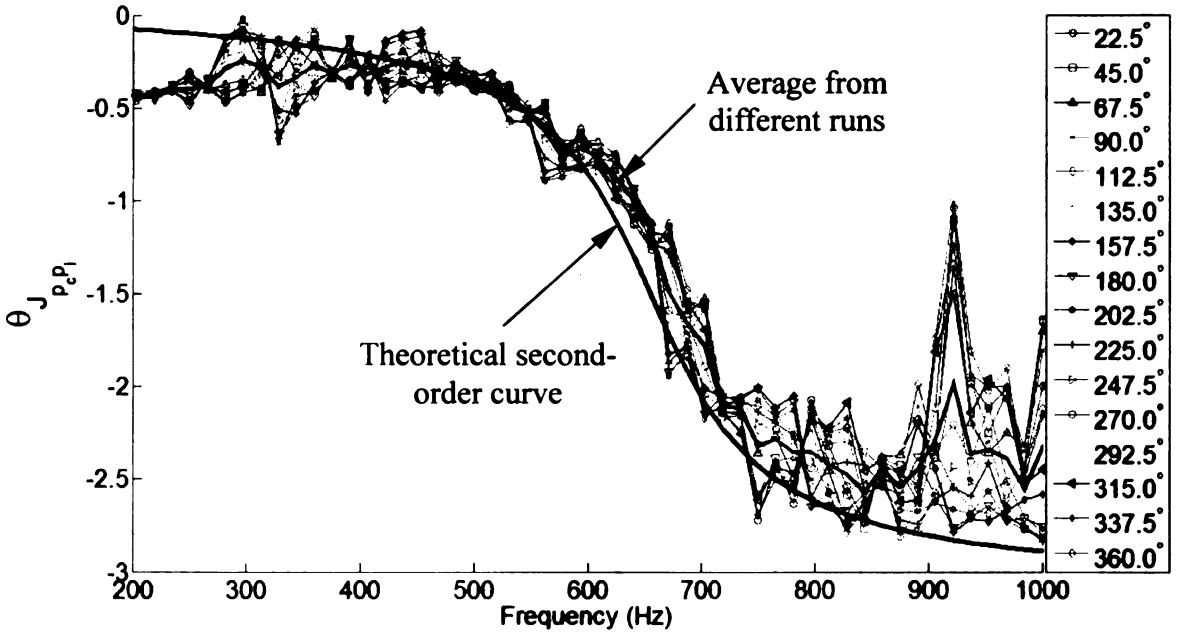

Figure 3.7. Phase of the acoustic system function of the Helmholtz resonator

The consistency of the resonator's acoustic response with that of a second-order system provides a significant verification concerning the behavior of the device. Specifically, unlike a simple Helmholtz resonator with small (relative to the wavelength of sound) circular opening, the current resonator has an azimuthal slit and hence is capable of sustaining infinite azimuthal modes of oscillation of the air mass within the resonator's neck. When forcing the flow, it is desired to control the oscillation mode to be of the axisymmetric form; i.e., that corresponding to in-phase movement of the air mass across the entire perimeter of the slit. This corresponds to the lowest order mode of oscillation of the device, which is the Helmholtz resonance. Thus, the current results confirm the observance of Helmholtz-resonance behavior, leading to axisymmetric forcing of the flow.

The magnitude and phase plots of the fluidic response of the resonator can be seen in Figures 3.8 and 3.9 below. The results are consistent with the acoustic response in

depicting a resonance frequency of 657 Hz and a behavior consistent with second-order system's response. However, the reader is reminded here that confidence in these results is limited to the frequency band extending from 600 Hz to 700 Hz (see coherence results above).

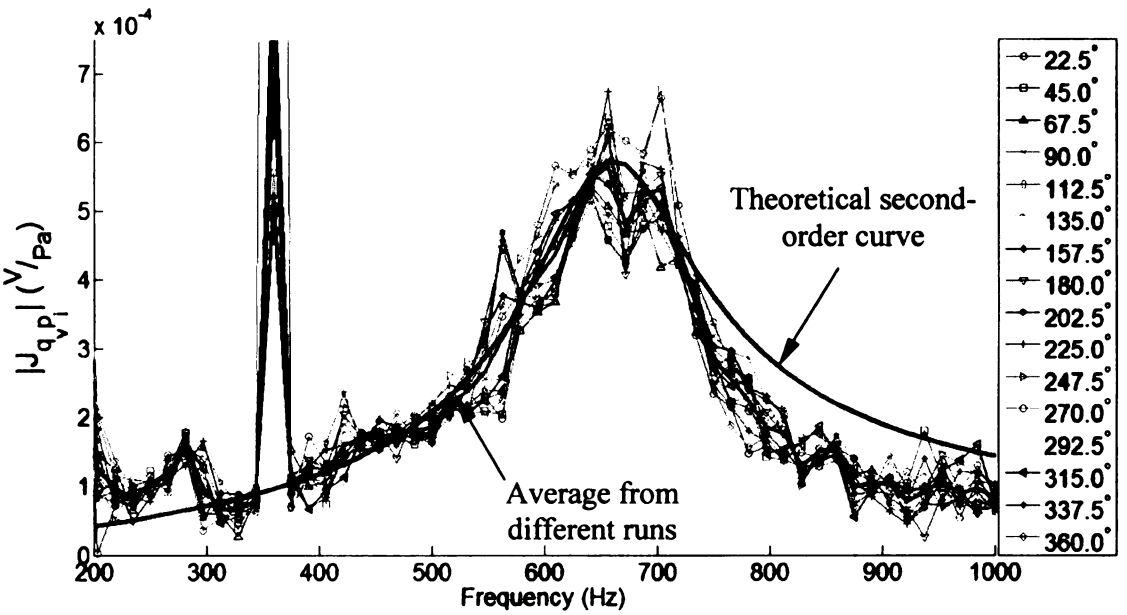

Figure 3.8. Magnitude of the fluidic system function of the Helmholtz resonator

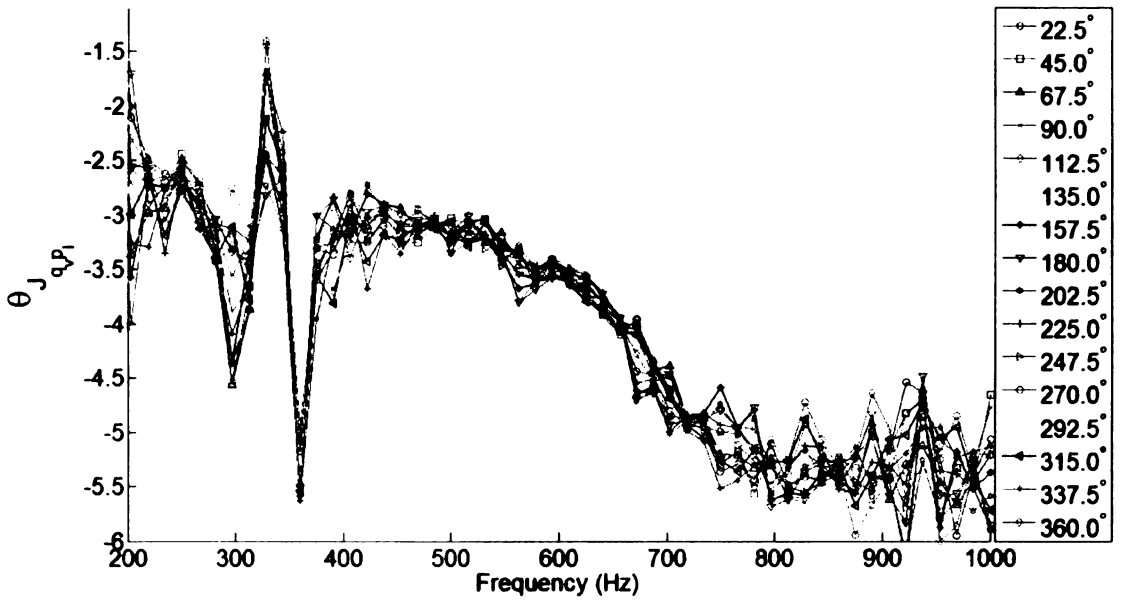

Figure 3.9. Phase of the fluidic system function of the Helmholtz resonator

3.2 Characterization of the nature of the resonator's fluidic disturbance

3.2.1 Background

Prior to examination of the velocity field produced by the excitation device, a brief summary of some pertinent literature is provided here. The aim of this summary is to use existing information to arrive at a "picture" of the expected nature of the fluidic disturbance. Subsequently, in sections 3.2.2 and 3.2.3, flow-visualization and single-hotwire results will be used to demonstrate the consistency of the resonator's behavior with that projected from consideration of the literature. The discussion should also help clarify certain flow physics about the behavior of driven resonators.

One of the early studies to examine the flow physics in the vicinity of the orifice of a driven resonator is that by Ingard and Labate (1950). In their flow visualization experiments, they identified four distinct regions of flow behavior depending on the acoustic velocity, i.e., sound level, of the imposed acoustic field. The brief descriptions by Ingard and Labate (1950) of these four regions are as follows:

- Region 1 A low intensity region with stationary circulation; the flow is directed out from the orifice along the axis.
- Region 2 A region of stationary circulation in which the direction of the flow along the axis is toward the orifice, i.e., the reverse of that in region 1.
- Region 3 A medium sound intensity region where pulsatory effects are superposed upon circulation of the kind in region 2.
- Region 4 A high sound intensity region in which pulsatory effects are predominant, resulting in the formation of jets and vortex rings. The jet consists of a strong airflow through the orifice, signified by a sudden burst of air. This burst appears symmetrically on both sides of the orifice and is made up of pulses contributed by each cycle of the sound wave.

As will be clarified later, the velocity field produced by the resonator here corresponds to two distinct regions (i.e., regions 1 and 4). Within region 1, the sound level is large enough to produce what is known as streaming, or steady, flow in addition to the usual oscillating flow component in the vicinity of the orifice. The streaming flow is characterized by a steady, outwards-directed jet along the centerline of the orifice. Two re-circulating-flow regions just outside the edges of the orifice surround this jet. Ingard and Labate (1950) pointed out that no mass exchange takes place between the inside and outside of the cavity in region 1. Therefore, the streaming motion consists entirely of the fluid from outside the resonator that is entrained into the jet.

On the other hand, a significant regime for the operation of the resonator is that at very high sound-intensity levels, or region 4. In this regime, formation of vortex structures takes place at the orifice during the blowing phase of the unsteady jet. These vortices move away from the orifice under the action of self-induced velocity, and hence produce a jet flow. Unlike region 1, however, this jet consists of the vortex structures (in addition to the entrained fluid), which originated from the fluid within the resonator's cavity. Therefore, the flow corresponding to region 4 involves mass exchange between the inside and outside of the cavity according to Ingard and Labate (1950). Of course, the mass outflow from the cavity must be balanced by the mass inflow to the cavity in a given oscillation cycle. Otherwise, the resonator would become a material "source" or "sink." However, Glezer and Amitay (2002) contradicted that finding, suggesting that no mass exchange took place with vortex formation. Glezer and Amitay (2002) pointed out that the jet's unique feature formed entirely from the working fluid of the flow system.

In recent history, utilization of jets with characteristics similar to those corresponding to region 4 has become wide spread. These jets, which are known as "synthetic jets", are produced by devices, which are quite similar to the driven Helmholtz resonator, except the driving mechanism is internal rather than external. The use of internal driving mechanisms, such as a piezoelectric membrane, compression driver, etc., has been favored over an external sound field due to the extremely loud sound required in the latter case to produce a region 4 behavior.

A fairly comprehensive review article of synthetic (zero mass flux) jets is that by Glezer and Amitay (2002). These authors point out that two of the key non-dimensional parameters characterizing the behavior of synthetic jets are the Reynolds number and non-dimensional stroke length. The former parameter may be defined utilizing the peak or average blowing velocity, or the jet impulse during discharge. The non-dimensional stroke length provides a measure of the distance traveled by a fluid element during the ejection phase relative to a characteristic dimension of the orifice.

The Reynolds number influence primarily relates to the asymmetry of the flow field during the ejection and suction phases. Specifically, at very low Reynolds numbers (creeping flow), the ejection flow does not separate from the orifice, and the flow during the ejection and suction phases will look like that of a "source" and "sink", respectively. As the Reynolds number increases, the "source" flow separates from the edges of the orifice, forming a jet that becomes much narrower, and directed along the orifice's centerline, than the "sink" flow.

On the other hand, the non-dimensional stroke length seems to be the primary parameter influencing whether or not periodic vortex-ring formation takes place.

Specifically, if the distance traveled by a fluid particle during the ejection phase of the cycle is too small in comparison to a characteristic orifice scale, one would not expect the fluid mass to travel too far from the resonator. That is, the ejected mass is likely to be drawn back again into the device during the suction phase. Under these conditions, no mass exchange takes place between the cavity and outside, and region 1 or 2 behavior is observed. However, if the non-dimensional stroke length is too large, fluid mass will be ejected from the cavity during the blowing phase, leading to region 4 behavior and periodic formation of vortices.

More recently, Wu and Breuer (2003) pointed out that the non-dimensional stroke length is essentially equivalent to the inverse of the Strouhal number, given by:

$$St_d = \frac{\omega d}{U_{\max}} \tag{3.8}$$

where ω is the driving angular frequency, d is the jet-slit width, and U_{max} is the maximum jet velocity during the ejection phase. Using PIV measurements, they documented the velocity field of a rectangular synthetic jet driven by internally mounted miniature speakers. Results were shown for two different cases corresponding to a Reynolds number (Re_d) of 15 and 62 (based on d and U_{max}) and St_d values of 4 and 1, respectively. The lower Reynolds number case exhibited practically similar flow fields during the ejection and suction phases (with the exception of reversal of the flow direction). The higher Reynolds number case (and lower Strouhal number/higher non-dimensional stroke length) exhibited a high degree of asymmetry between the suction and ejection phases. This was associated with a flow velocity at and near the centerline of the jet that was

always directed away from the orifice (i.e., in the ejection direction). However, the Strouhal number was too large (or, the stroke length was too small) for vortex formation to take place.

The velocity-field measurements of Wu and Breuer (2003) at the higher Reynolds number seems to correspond quite well with region 1 behavior described above. Interestingly, the non-dimensional parameters of their jet are of the same order as found in the current study. In particular, for the strongest sound used here during resonator characterization under harmonic excitation, the Reynolds number (Re_d) and St_d were nominally 29.9 and 2.1 respectively. Based on this comparison, it is unlikely that periodic vortex formation occurs in the present case under periodic driving conditions. Under amplitude-modulated conditions, higher instantaneous sound amplitudes were utilized, leading to peak instantaneous velocity values that are approximately twice that of the strongest harmonic condition. The corresponding peak, *instantaneous*, $Re_d \sim 60$ and $St_d \sim 1$, are almost identical to the strongest forcing case of Wu and Breuer (2003). This, again, suggests that no unsteady vortex formation takes place here. This suggestion should be treated with caution, though, since the jet is operating under unsteady, amplitude-modulated conditions, which is different from the steady, harmonic excitation of Wu and Breuer.

To illustrate further that no mass exchange between the cavity and outside is expected to take place for the resonator used here, consider a slightly different form of the Strouhal number:

$$St_l = \frac{l}{(T/2)U_{avg}} \tag{3.9}$$

where T is the period of the forcing signal, l is the length of the resonator's neck and U_{avg} is the average velocity during the blowing stroke. The denominator in equation 3.9 gives the distance traveled by a fluid particle on the centerline of the jet during the blowing stroke. Calculation of St_l for the strongest jet velocity encountered here under harmonic forcing conditions (order of 1 m/s) yields a value of nominally 8.1. This shows that during the ejection stroke the particle travels a distance that is almost an order of magnitude smaller than the length of the resonator's neck. This provides additional support to the idea that the current flow-excitation device does not involve mass exchange between the cavity and outside. The following section provides flow-visualization and hotwire-measurement results that are consistent with this statement.

3.2.2 Flow visualization of the flow field in the vicinity of resonator's opening

Four sequences of flow-visualization snapshots corresponding to four forcing configurations under no-flow condition are to be represented in the following order: unforced-flow case, sine-wave-forcing cases (at two different forcing amplitudes), and amplitude-modulation-forcing case. The aim of this flow-visualization analysis is to examine the consistency of the behavior of the resonator's fluidic disturbance with the assessments made in section 3.2.1, and attempt to understand the nature of the flow behavior in the vicinity of the resonator's orifice.

The smoke-wire technique was employed for flow-visualization. The set-up involved the use of a couple of short-length, 0.1 mm-diameter, stainless steel wires

("smoke wires") that were mounted on two hotwire prongs, with wires lined-up in parallel to each other. The use of two wires helped in the retention of an oil film when the wires were wetted with oil for model-train smoke. The wetted wires were then positioned immediately above the resonators' slit opening (see Figure 3.10a). A homemade smoke-wire, controller box was used to initiate the smoke generation and capturing of images using a CCD camera at standard video rate of 30 frame/s. This was accomplished through flipping of a toggle switch on the controller-box panel, which immediately actuated a solenoid to feed electrical current through the smoke wire for heating and subsequent evaporation of the smoke, for a period of time that is adjustable through a timing knob in the controller box. Simultaneously, flipping of the toggle switch initiated a 0 – 5 V output-signal that was connected to the trigger-signal input of the image grabber used for capturing the output of the CCD camera. Thus, the process of image capturing and smoke generation commenced simultaneously. Given the initial thermal transient associated with heating and evaporation of the oil, a typical test allowed for capturing of enough number of images that covered the duration before, during and after the generation of smoke.

3.2.2.1 Buoyancy effect (unforced condition)

Given that the heated smoke will have lower density than the surrounding air, it is evident that, especially in the absence of flow external to the resonator, the visualization technique could introduce a significant, buoyancy-induced, flow pattern that is not related to the actual fluidic disturbance produced by the resonator. Therefore, it was desired to initially capture images of the flow pattern resulting from pure buoyancy effects; i.e.,

without driving the resonator. The resulting sequence of images is presented in Figures 3.10a-f, where the first image (Figure 3.10a) was taken almost immediately after triggering the smoke wires. These images are provided for reference in order to demonstrate that subsequent observations, obtained when the resonator is actuated, are not an artifact of buoyancy effects.

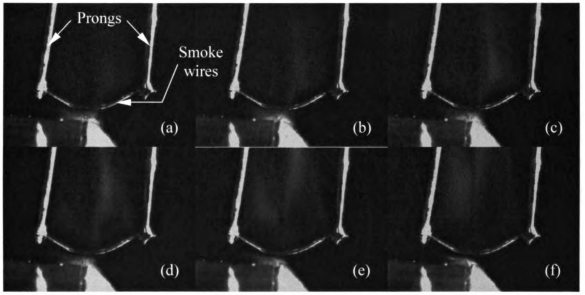

Figure 3.10a-f. Smoke-wire images of the buoyancy-induced flow under unforced condition

3.2.2.2 Sine-wave forcing effect

For this case, a pure harmonic wave at frequency $f \approx 630$ Hz was used to drive the speaker at two different forcing amplitudes: one representative of the forcing levels used in this study, and the other at a level that is well above any employed here. The latter was employed in order to examine if the resonator could be operated in the regime where periodic vortex ejection takes place; i.e., similar to a synthetic jet (or region 4 of Ingard and Labate, 1950).

3.2.2.2.1 Forcing amplitude representative of those used in present study

A sequence of twelve images is displayed in Figures 3.11a-l for sinusoidal forcing at RMS acoustic pressure value of 4.63 Pa at the resonator opening. The most significant point concerning the images in Figure 3.11 is that, consistent with the earlier projection based on the analysis in section 3.2.1, there is no evidence of periodic formation of vortices. Additionally, video observations of several recordings similar to that shown in Figure 3.11 always revealed steady flow of smoke in the upward direction. This provides evidence for the establishment of streaming flow. This flow should not be an artifact of the smoke-wire's buoyancy effects, given the big difference in the observed smoke pattern between Figures 3.11 and 3.10. Of course, this does not imply that buoyancy effects are negligible all together in the images shown in Figure 3.11. In fact, it is believed that these effects are responsible for the meandering (flame-like) appearance of the smoke.

Another interesting point concerning the results in Figure 3.11 is the formation of what appears to be two re-circulating flow regions at the edges of resonator's slit (most evident in Figure 3.11j and 3.11k). The reader is cautioned, though, that these regions are difficult to identify in the picture, since they are very small and are not resolved properly in the given view. However, if correct, this would be consistent with the expected flow behavior in "region 1" of the Ingard and Labate (1950) study (see section 3.2.1).

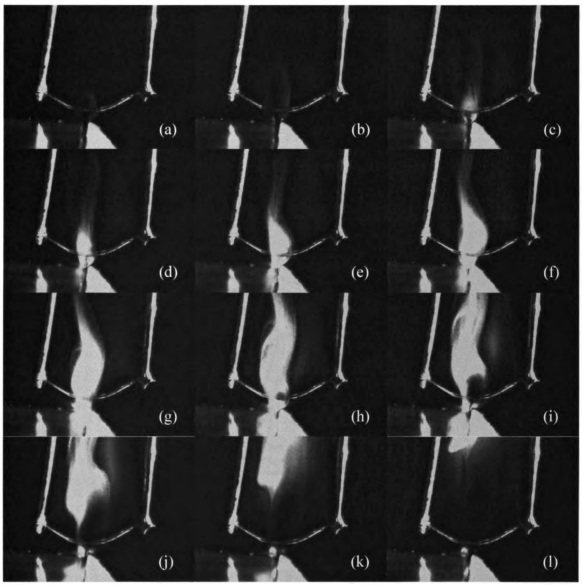

Figure 3.11a-l. Smoke-wire images of the flow above the resonator's slit under sinusoidal forcing conditions at a level representative of that used to obtain data in this study

3.2.2.2.2 High intensity forcing amplitude

The next sequence of images (Figures 3.12a-i) represents sinusoidal forcing at a level higher than any employed for quantitative measurements in this study. It is clear that under these forcing conditions the Strouhal number (or stroke length), see section 3.2.1, is sufficiently small (large) for periodic vortex formation to take place.

Additionally, observations of the temporal evolution of the image sequence shown in Figure 3.12, and other similar sequences, reveal the existence of strong streaming flow. The behavior of the resonator disturbances is consistent with that of region 4 of the Ingard and Labate (1950) study.

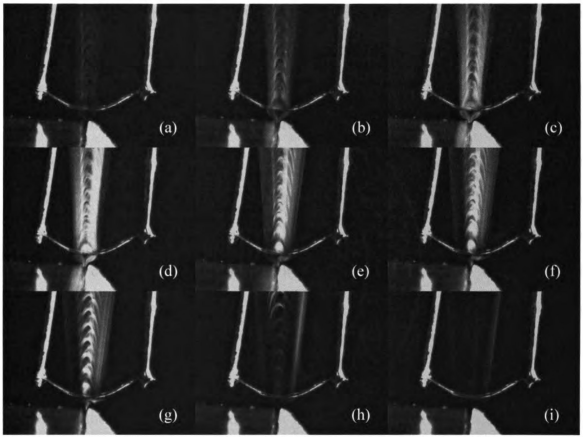

Figure 3.12a-i. Smoke-wire images of the flow above the resonator's slit under sinusoidal forcing conditions at a level stronger than that used to obtain data in this study

3.2.2.3 Amplitude-modulation forcing effect

The last sequence of images (shown in Figures 3.13a-o) demonstrates flow visualization of the resonator's flow field under the strongest amplitude-modulated forcing used here. The forcing was achieved using a nominal carrier frequency, f_c, of 630 Hz and a modulation frequency, f_m, of 18 Hz.

The images in Figure 3.13 reveal periodic modulation in the width of the smoke pattern. It is presumed that this modulation takes place at twice the modulation frequency, which corresponds to the repetition of the cycle of build up of strong forcing amplitude followed by decay to zero forcing. In the absence of existing literature concerning the flow structure of amplitude-modulated, synthetic jets and driven resonators, it is difficult to rely on the qualitative flow visualization results shown in Figure 3.13 to clarify the underlying flow physics. A simple-minded possibility for the observed modulation in the smoke width may relate to the spread rate of the jet associated with the streaming flow. During the modulation cycle, the jet is likely to spread more widely at low forcing levels because of the lower Reynolds number of the jet. At higher level, a narrower and faster jet will be produced. Periodic repetition of this cycle would then cause the jet's width to be modulated, as seen in the images. The actual flow behavior is likely to be substantially more complex than offered by this "quasi-steady-flow" description.

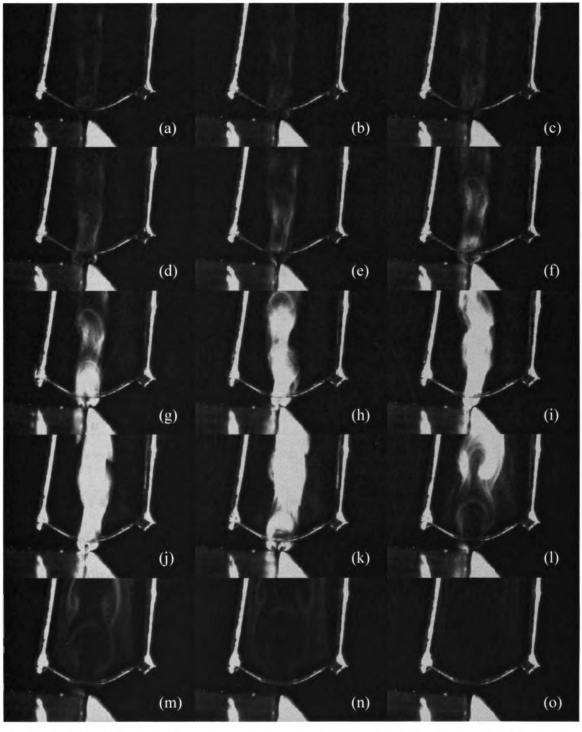

Figure 3.13a-o. Smoke-wire images of the flow above the resonator's slit under amplitude-modulated forcing conditions at highest level of forcing

3.2.3 Hotwire measurements of the resonator's velocity field

To quantify the velocity disturbance produced by the Helmholtz resonator, a single hotwire sensor was utilized. The adoption of the hotwire for the velocity-measurement tool was motivated by the simplicity of its use, and its good temporal and spatial resolution. However, the hotwire suffers from two important shortcomings that limit the interpretation of the measurements. First, it is directionally blind, so it cannot distinguish between the suction and ejection velocity. Second, it is equally sensitive to the lateral (x) velocity component, as it is to wall-normal (y) velocity component (see Figure 2.14 showing the x and y axes). Therefore, the hotwire sensor actually measures q, or the total velocity component in the x-y plane, given by:

$$q = \sqrt{u^2 + v^2} \tag{3.10}$$

where u and v are the velocity components parallel to the x and y directions, respectively. Note that the azimuthal velocity component is ignored here since: (1) it has an order of magnitude lower cooling effect on the hotwire; (2) the resonator disturbance is predominantly two-dimensional as demonstrated earlier from the velocity spectra (see Figure 3.3). Finally, for the remainder of this work, q will be frequently decomposed into the sum of a time average component Q, and an unsteady component q'.

Although the above discussion points out important limitations concerning the information that can be extracted from the single-wire measurements, the data can be used to reliably quantify the excitation level of the flow. This can be done for instance by calculating the relative magnitude of q_{max} to the freestream velocity (a more specific

definition will be introduced in Chapter 4). Additionally, q information may be combined with physical reasoning to infer certain characteristics of the measured velocity field. These can then be examined against the nature of the fluidic disturbance predicted from analysis of the literature in section 3.2.1 and the flow visualization results in section 3.2.2.

Figure 3.14 provides a plot of the *phase-averaged* q ($<q>$) measured at $y = 0$ above the slit exit for one cycle of forcing at a nominal frequency of 630 Hz. The phase average is obtained relative to the phase of the forcing signal. For reference, the latter signal is included in Figure 3.14 in a separate plot. The different-color lines in the figure correspond to measurements at different x locations across the slit. Note that $x = 0$ corresponds to the "downstream" edge of the slit (see Figure 2.14). The driving acoustic pressure for this particular data set was 43.1 Pa peak-to-peak.

The measurements indicated by the red line correspond to a location of the hotwire sensor that is about 0.05 mm upstream of the slit (or x = -0.55 mm). Thus, the wire is in the immediate vicinity of the test-model's surface, which suggests that the measurements primarily correspond to the u, or wall-parallel, velocity component. The shape of the red line corresponds to a 'rectified-like' sinusoidal variation with two velocity peaks per cycle. Presumably, these peaks correspond to the peak suction and ejection phases; although it is not clear which is which. During the ejection phase, one would expect that measurements at the location corresponding to the red line should reflect the velocity of the entrainment flow towards the jet. In addition, during the suction phase the velocity will also be directed towards the centerline as the suction effect draws fluid mass towards the orifice. Therefore, it is likely that the rectified waveform

seen at x = -0.55 mm is in fact reflective of flow towards the jet for *both* the suction and ejection phases.

Consideration of the hotwire traces close to the slit's center helps to distinguish the suction from the ejection phase. For instance, at x/d = -0.5, one can still identify two local peaks per cycle in the hotwire signal. Since the jet flow is substantially narrower than the sink (suction) flow, the velocity should be higher during the ejection phase. Therefore, the peak of the ejection cycle is identified with the larger peaks in the hotwire trace (see arrows shown in the figure). On the other hand, the peak of the suction cycle is associated with the smaller velocity peak at x/d = -0.5. The velocity direction corresponding to this peak cannot be determined without ambiguity. The high-Reynolds-number synthetic jet of Wu and Breuer (2003) always sustained positive velocities, even at the peak suction phase, on the centerline of the slit. In their case, however, the velocity trace had a local minimum at the peak suction phase. This is unlike the results found here where a local peak, albeit weak, is identified. Thus, in this study it is possible that the flow actually reverses direction for part of the suction cycle and/or the peak may be produced by an instantaneous cross-stream (wall-parallel) component.

Another piece of information that is depicted from the results in Figure 3.14 relates to flow symmetry relative to the center of the slit. Data measured at x locations that are symmetric relative to the center of the slit are generally different. For example, the velocity signal at x/d = -0.7 and -0.3 exhibit large differences during the suction phase. At x/d = -1.1 and 0.1, substantial differences are seen for the ejection phase. This flow asymmetry should not be too surprising given that the geometry of the resonator is not symmetric relative to the slit's center.

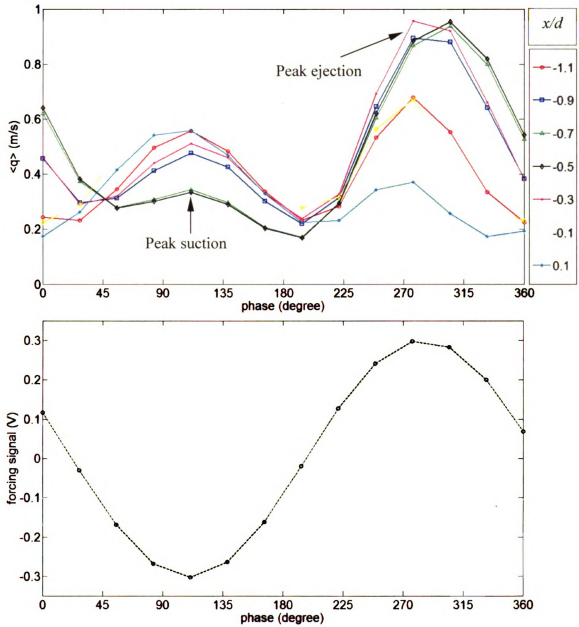

Figure 3.14. Phase-average of hotwire output at different x locations and $y = 0$ (top); forcing signal (bottom)

Some of the above observations may also be seen more easily in Figure 3.15, which provides plots of the velocity profiles across the slit opening of the resonator taken at the peaks of both the suction and ejection phases.

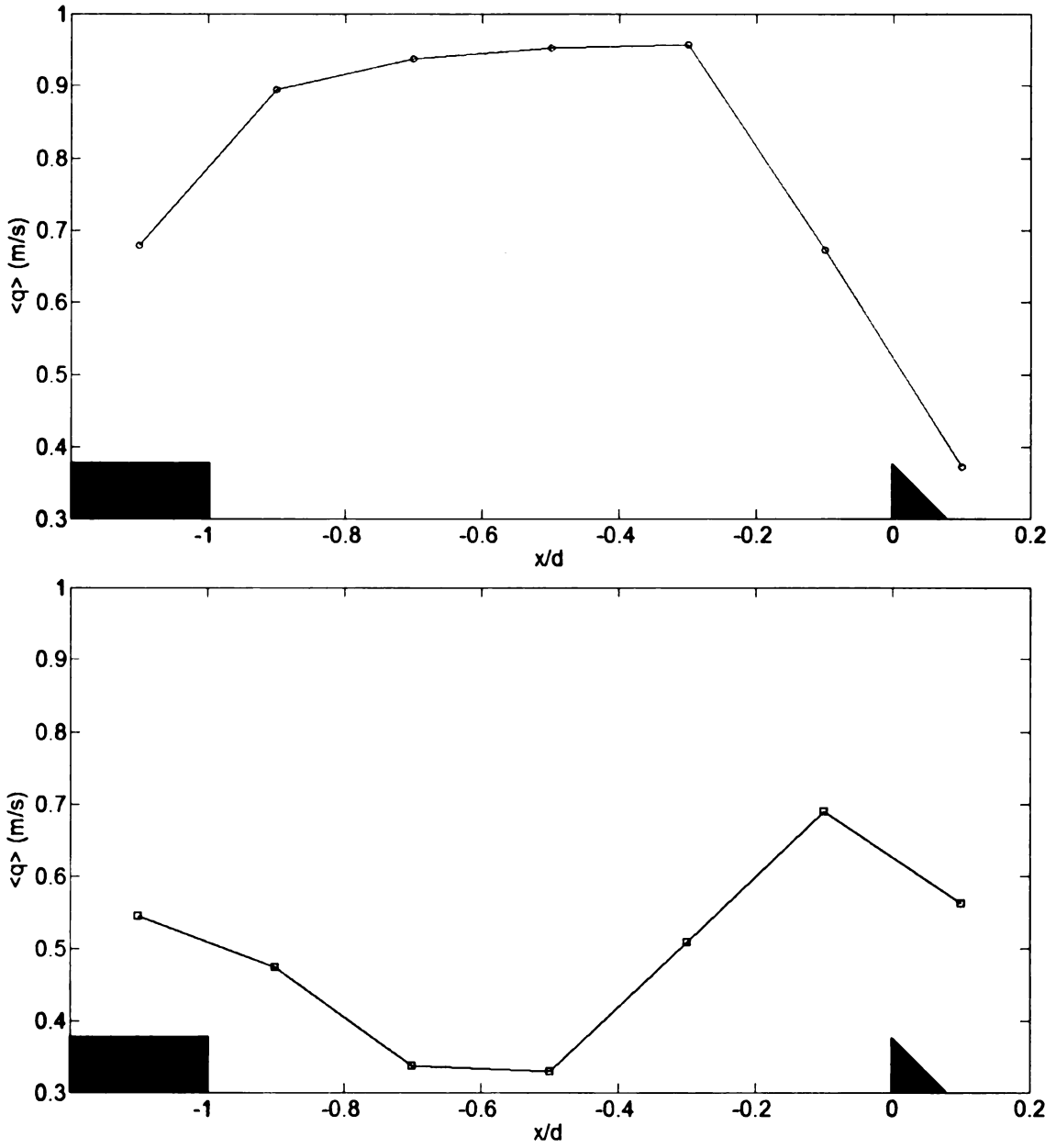

Figure 3.15. Velocity profiles across the resonator's slit opening during peak ejection phase (top) and peak suction phase (bottom)

The next analysis is concerned with the influence of the driving-sound level on the generated hydrodynamic disturbance. To this end, velocity data were sampled with the hotwire sensor located at the center of, and just above the resonator's slit (x/d = -0.5 and y/d = 0). The forcing amplitude was varied to produce five different levels of RMS

acoustic-pressure fluctuations at the resonator's opening: 4.65, 2.71, 4.63, 5.83 and 7.68 Pa. The corresponding hotwire signals are displayed in Figure 3.16 for two forcing cycles. Note the displayed signals have been phase-averaged, and therefore the peaks and valleys in the results for the different forcing levels occur at the same time.

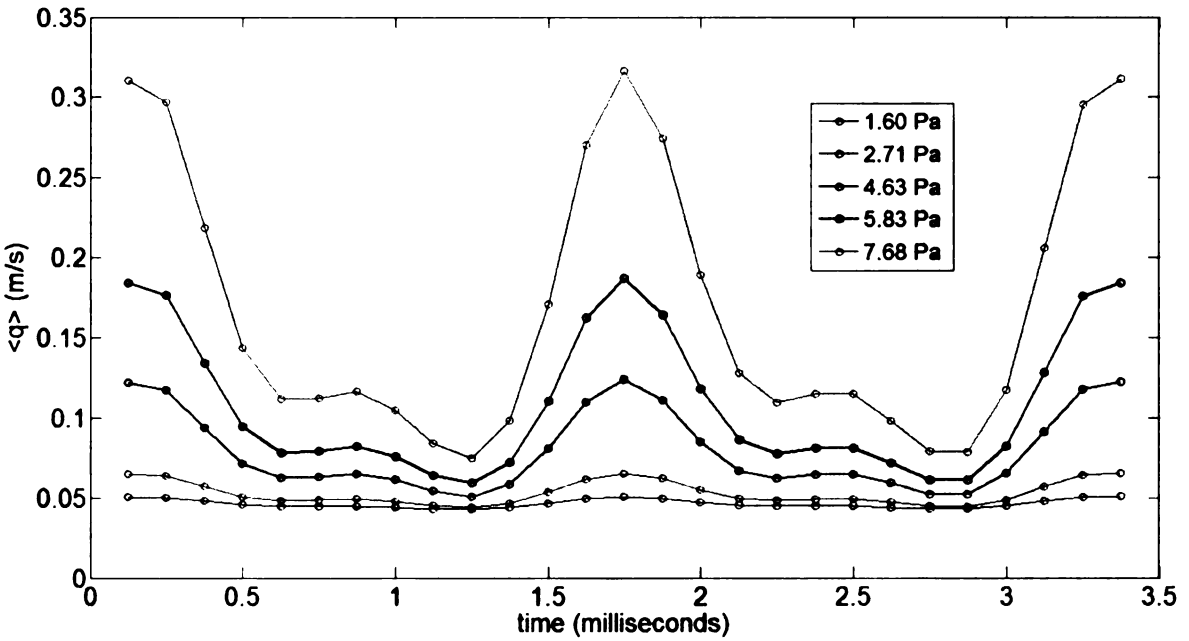

Figure 3.16. Conditional average of the hotwire output for different forcing levels (data obtained at x/d = -0.5 and y/d = 0)

Two primary effects of forcing level can be depicted from Figure 3.16. Not surprisingly, as the forcing amplitude is increased, the fluctuating velocity component associated with the jet ensuing from the resonator becomes more significant. More interestingly, however, is the vertical shift in the mean ("DC" component) of the measurements that becomes progressively stronger with increasing forcing level. This provides evidence that the purely sinusoidal acoustic forcing imposed by the speaker produces not only a sinusoidal fluidic disturbance of the flow, *but also* a steady

component as well. These observations, although seem counter intuitive, they are consistent with the findings of Ingard and Labate (1950) discussed in section 3.2.1 and the flow visualization results presented in section 3.2.2 earlier.

The formation of the mean motion is essentially reflective of the non-linearity of the resonator at large levels of driving acoustic pressures. As explained in section 3.2.1, this mean motion is formed entirely from entrained fluid from outside the cavity at high Strouhal numbers, but its motion does contain fluid from the cavity at low Strouhal numbers. In the latter case, the fluid ejected from the cavity must be replaced during the suction stroke since the net average mass flow rate through the resonator must be zero. Given the qualitative similarity of the hotwire signal shapes in Figure 3.16 for all forcing levels that extend down to the weakest level, it is apparent that no change in the nature of the resonator's fluidic disturbance takes place as the forcing level is increased. Moreover, it is also most likely that the resonator's operating regime corresponds to the weakest-forced regime of Ingard and Labate (1950) since the lowest forcing level used here corresponds to a quite low sound pressure level of 98.1 dB. In fact, St_l (see Equation 3.9) for the lowest forcing level is 39.9, which provides further support that no mass exchange takes place between the inside and outside of the resonator's cavity in this study, and that the streaming motion is formed from fluid entrained from outside the cavity. This is also consistent with the flow visualization results in Figure 3.11, where no evidence of periodic vortex formation was found.

Finally, the dependence of the fluidic disturbance on the distance from the resonator's exit was investigated. This was accomplished by locating the hotwire at the center (x/d = -0.5) of the resonator's slit and different heights in the range of y/d = -0.11

to $y/d = 1.89$. For all y locations, the driving acoustic pressure was kept at a level of 16.7 Pa. The resulting phase-averaged velocity traces can be seen in Figure 3.17 for the duration of two forcing cycles. As expected, the strength of the streaming and unsteady disturbance velocity decreases as the distance between the hotwire sensor and the slit opening increases.

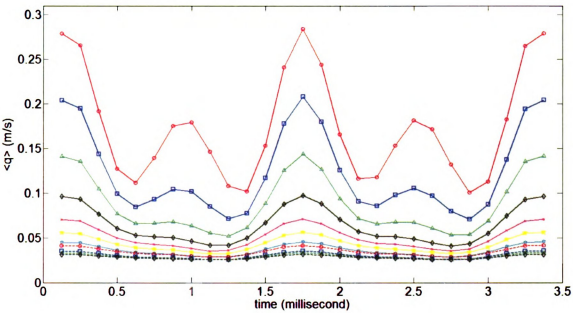

Figure 3.17. Conditional average of hotwire output at 11 different y–positions (y/d = -0.11, 0.09, 0.29, 0.49, 0.69, 0.89, 1.09, 1.29, 1.49, 1,69, and 1.89 from top to bottom)

3.3 Resonator's disturbance characteristics under modulated forcing conditions

As discussed in the introduction (section 1.2), periodic excitation of separated flows near the separation point is most effective if the excitation frequency is selected such that the reduced frequency F^+, defined as follows, is of order 1:

$$F^+ = \frac{f_e L}{U_\infty} \tag{3.11}$$

where, f_e is the excitation frequency of the flow, L is a length scale characteristic of the separation bubble size (typically taken as the reattachment length, x_r, for separating/reattaching flows), and U_∞ is the freestream velocity. For the present flow field, an $F^+ = 1$ corresponds to a frequency of 67 Hz. Clearly, this is an order of magnitude lower than the resonant frequency of the Helmholtz resonator, and hence simple driving of the resonator at its resonance frequency is not anticipated to lead to effective control of the separation bubble. On the other hand, if one operates the resonator directly at the desired low frequencies, the resulting fluidic disturbance is extremely weak and incapable of exciting the flow (e.g., see Figure 3.3, where the disturbance velocity is indistinguishable from the hotwire anemometer's background noise for frequencies below 400 Hz).

To remedy the mismatch between the resonator's operating frequency and the effective flow forcing frequency, it was decided to modulate the amplitude of the main resonator's driving, or carrier, acoustic signal (with frequency f_c = 630 Hz) at the desired low frequency (f_m). In order for this approach to be successful, a non-linear coupling mechanism is required between the input acoustic disturbance and the flow field.

Specifically, modulation alone will result in exciting the flow at two different frequencies simultaneously: $(f_c - f_m)$ and $(f_c + f_m)$ as described in section 2.1.3.5. Since the modulated frequency is much smaller than the carrier frequency ($f_m << f_c$), these two new frequencies do not deviate substantially from the high operating frequency and would not produce the desired result. However, if a non-linear coupling mechanism exists between the modulated acoustic signal and the flow, then frequencies corresponding to various sums and differences of $(f_c - f_m)$ and $(f_c + f_m)$ will be generated. In particular the difference between these two frequencies produces a sinusoidal signal at a frequency of $2f_m$, which is much lower than f_c.

For this study, the Helmholtz resonator, when driven at high sound intensities, provides the necessary non-linear coupling mechanism. As demonstrated earlier, the non-linearity of the resonator results in the formation of a streaming disturbance component when driven using a pure harmonic signal. Since the magnitude of the streaming disturbance increases with the amplitude of the harmonic signal, then amplitude modulation of the latter will result in a time-varying magnitude of this streaming disturbance at a frequency of $2f_m$. It is this sinusoidal disturbance that should couple to the separated flow effectively. Consequently, it is likely that the flow response to this type of amplitude-modulated forcing is similar to direct harmonic excitation at frequency of $2f_m$ (although this statement requires verification via measurements of the flow field under forced conditions). This is to be distinguished from other types of amplitude-modulated frequency, such as that by Wiltse and Glezer (1993), where the non-linear response of the *flow* to high-amplitude forcing by piezoelectric actuators, is

argued to provide the coupling mechanism between the amplitude-modulated excitation and the flow.

The range of modulation frequencies employed here is f_m = 10 – 40 Hz. As will become clear in the following chapter, an optimal (largest flow change for a given forcing level) modulation frequency of 18 Hz (note that actual flow excitation frequency is $f_e = 2f_m$ = 36 Hz) was found. Therefore, the main focus of the discussion in this section, and the remainder of the thesis, will be on cases corresponding to 10 Hz and 18 Hz modulation frequencies. The first case provides an example of forcing that produces hardly any change to the flow, whereas the latter is where substantial flow changes are observed.

Figure 3.18 provides plots of the imposed acoustic pressure at the resonator's slit for the two different forcing levels employed with 10 Hz modulation frequency. It can be seen that good modulation quality (amplitude change ranging from full amplitude down to zero) is attained. This was possible because of the use of two independent function generators to synthesize the amplitude-modulated signal as described in section 2.1.3.5.

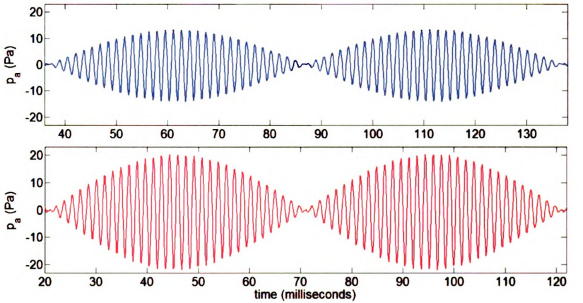

Figure 3.18. Sample of the driving acoustic signal at 10 Hz modulation frequency and two forcing levels

The velocity measurements at the exit of the slit (x/d = -0.5 and y/d = 0) corresponding to the excitation sound signals shown in Figure 3.18 are shown in Figure 3.19. In order to distinguish the lower-frequency modulation from the higher-frequency signal, a low-pass filter was used in the data processing. The cut-off frequency of the filter was set to 200 Hz. The resulting filtered signal is shown using a black line in Figure 3.19. It is clear that the black line "traces" the low-frequency component (i.e., modulated streaming flow) that is employed to affect the flow. Also, note that, as discussed above, two cycles of the low frequency forcing are realized during a single modulation cycle (100 milliseconds for 10 Hz). This means that the actual frequency affecting the flow is in fact twice the modulating frequency, i.e., 20 Hz.

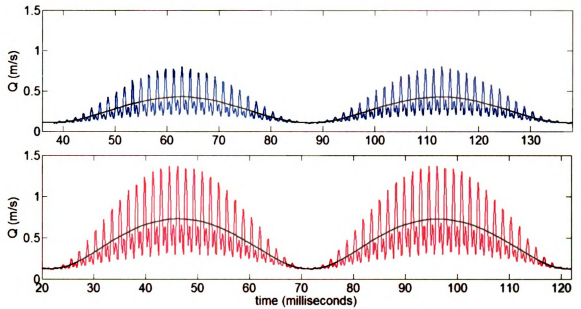

Figure 3.19. Velocity measurements at x/d = -0.5 and y/d = 0 corresponding to the amplitude-modulated acoustic forcing shown in Figure 3.18

Similar results to those shown in Figures 3.18 and 3.19, but for 18 Hz modulation frequency are shown in Figures 3.20 and 3.21. In this case, five different forcing levels were employed (since this was found to be the optimal modulation frequency, as will be discussed in Chapter 4). The corresponding driving acoustic pressure signals can be seen in Figure 3.20. The peak-to-peak values of these signals, from the weakest to the strongest are 10.6, 24.9, 33.9, 49.2, and 69.8 Pa (shown using cyan, magenta, green, blue, and red colored lines, respectively). The resulting velocity traces of the fluidic disturbance at x/d = -0.5 and y/d = 0 are shown in Figure 3.21, along with the low-frequency component highlighted using a black line. The details of these velocity traces may be seen more clearly from Figure 3.22, where "magnified" plots of the traces for the two, largest, forcing amplitudes are given.

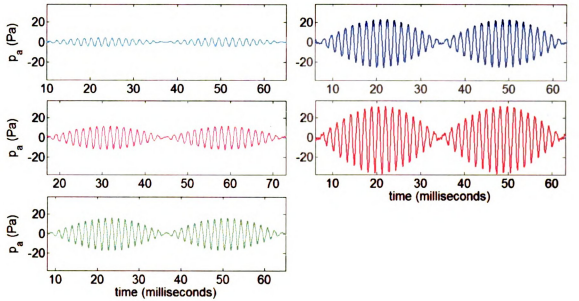

Figure 3.20. Sample of the driving acoustic signal at 18 Hz modulation frequency and five forcing levels

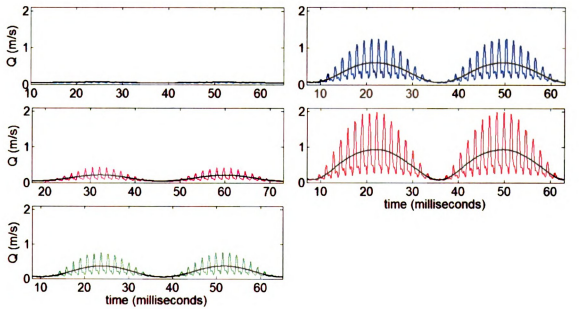

Figure 3.21. Velocity measurements at x/d = -0.5 and y/d = 0 corresponding to the amplitude-modulated acoustic forcing shown in Figure 3.20

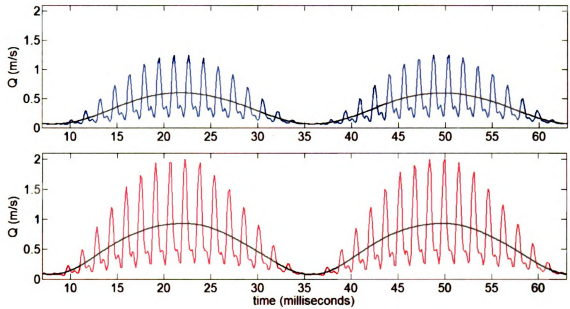

Figure 3.22. Magnified velocity measurements at *x/d* = -0.5 and *y/d* = 0 corresponding to the two largest amplitude-modulated acoustic forcing shown in Figure 3.20

A quantitatively better way of representing the input pressure and resulting excitation velocity relationship is by plotting the RMS of the low-pass-filtered velocity against the input, peak-to-peak pressure. Such plots are done for the two forcing levels employed at 10 Hz modulation frequency, and the five forcing levels used at 18 Hz modulation frequency. The plots can be seen in Figure 3.23.

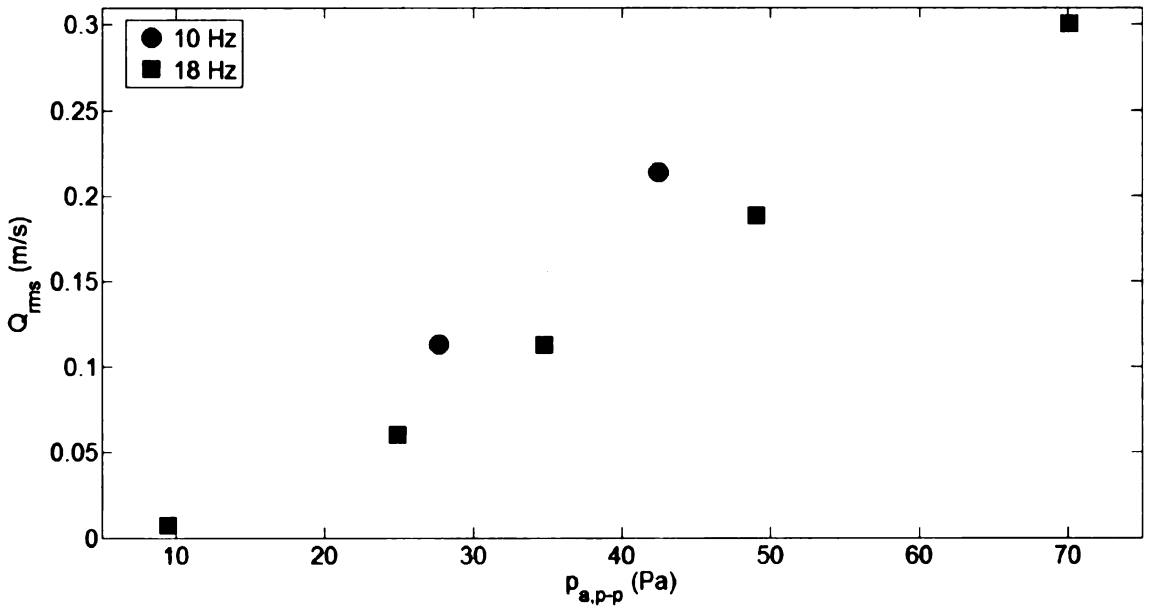

Figure 3.23. RMS of the low-frequency-disturbance velocity versus the input peak-to-peak of the driving acoustic pressure

It is also important to examine the harmonic content of the excitation (low-frequency) signal. To this end, the power spectrum of the low-pass filtered velocity component in the case of 18 Hz modulation frequency is obtained. A sample of this spectrum for peak-to-peak acoustic pressure of 49.2 Pa is provided in Figure 3.24. Two different plots are included in the figure: the top plot (Figure 3.24a) displays the spectrum using logarithmic scale, and the bottom plot applying linear ordinate scale. The former scale indicates certain amount of harmonic distortion, where a second harmonic of the excitation frequency is evident at 72 Hz. However, this distortion is practically negligible, as evident from the dominance of the peak at 36 Hz. In fact, the second harmonic peak cannot be detected altogether in the semi-log plot.

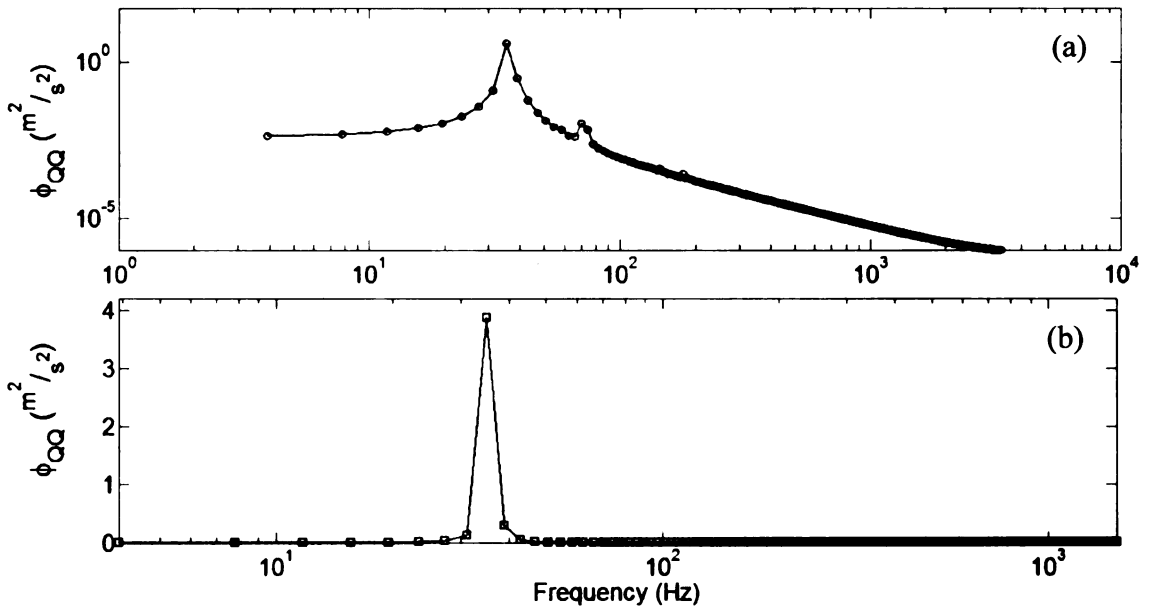

Figure 3.24. A sample power spectrum of the low-frequency fluidic disturbance associated with 18 Hz modulation frequency: (a) logarithmic scale, (b) linear ordinate scale

Finally, as indicated in the motivation section, one of the significant aspects of the flow-excitation device developed here is that it is acoustically quite at the excitation frequency. More specifically, the above discussion indicates that the acoustic input used to drive the speaker will occur at frequencies of $(f_c + f_m)$ and $(f_c - f_m)$, which are nominally at 612 and 648 Hz for a modulation frequency of 18 Hz. Under these conditions, the actual excitation to the flow takes place via a *fluidic* disturbance at a frequency of 36 Hz, or $2f_m$. Thus, it is evident that the major sound contamination from the driven-resonator is at a much higher frequency than the excitation frequency, and hence this contamination could be removed easily via low-pass filtering. This point is demonstrated using the power spectrum results in Figure 3.25 of the acoustic pressure measured at the resonator's lip, under no-flow conditions, for the two lowest forcing levels and modulation frequency of 18 Hz. Note that only the two lowest forcing levels

are examined here since no wall-pressure measurements were conducted for higher forcing levels (because of a dynamic-range limitation of the surface-pressure sensors, as discussed in Chapter 4).

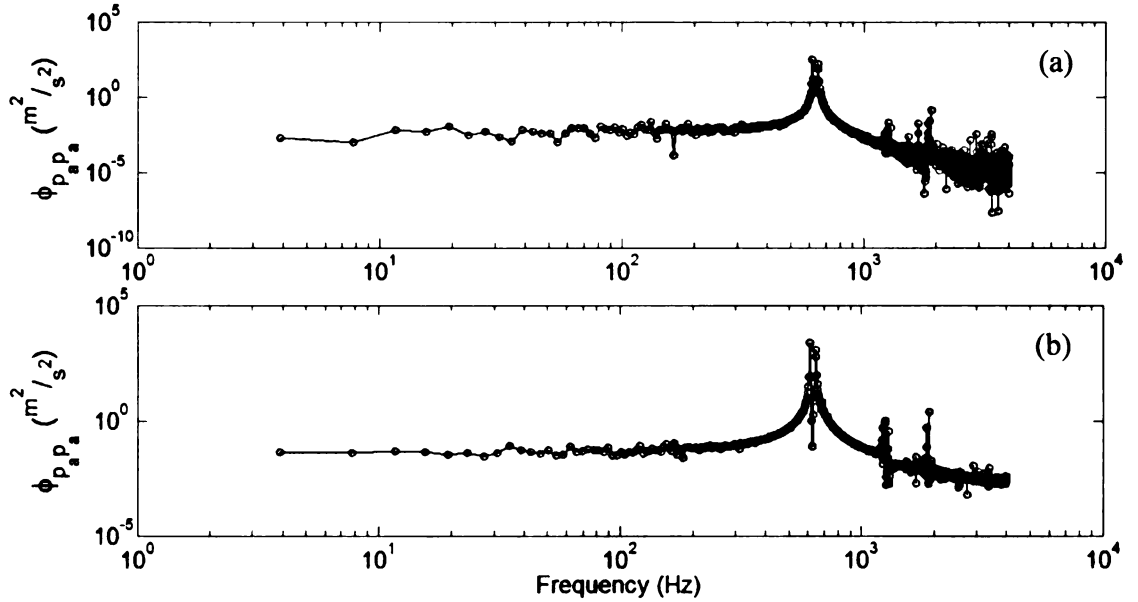

Figure 3.25. Sample power spectra of the acoustic pressure associated with 18 Hz modulation frequency and two lowest forcing levels: (a) 10.6 Pa peak-to-peak, (b) 24.9 Pa peak-to-peak

The spectra in Figure 3.25 show that no pressure disturbances are detected at $2f_m$, or 36 Hz, at the lowest forcing level. A very weak disturbance is seen at 36 Hz for the higher forcing level. This is likely related to the hydrodynamic pressure fluctuations of the oscillating jet, given that the measurements were conducted in the immediate vicinity of the resonator's slit. Moreover, the pressure fluctuations energy contained in this peak is equal to only 1.6% of the peak, hydrodynamic surface-pressure fluctuations measured here. It is noted, though, that we believe that the driven resonator is acoustically quite at forcing levels typical of those used here. At substantially higher forcing levels, the

oscillating jet velocity could become sufficiently high such that the unsteady *fluidic* disturbance itself may become an efficient noise generator.

4 EFFECT OF FORCING ON THE SEPARATED FLOW

In the following sections, an analysis focused on assessing the influence of forcing on the axisymmetric back-step flow will be presented. In the analysis, two issues are of specific interest. First, it is desired to assess whether amplitude-modulated forcing using the externally driven Helmholtz resonator is capable of altering the global characteristics of the separation bubble. To this end, the mean wall-pressure data beneath the bubble will be examined under different levels and frequencies of forcing. It is also desired to learn if alteration to the mean wall-pressure field characteristics caused by the amplitude-modulated forcing is similar to (or different from) those obtained under the more conventional, periodic way of flow control. The second issue to be investigated here is the effect of forcing on the unsteady wall-pressure measurements. This study is preliminary and is primarily focused on the effect of forcing amplitude and modulation frequency on the RMS pressure fluctuations, the corresponding Power Spectral Density (PSD), and the frequency-wavenumber (f-k_x) representation of the spatio-temporal characteristics of the unsteady wall-pressure field.

4.1 The effect of forcing on the mean-pressure distribution

As indicated in Chapter 2, mean-wall-pressure measurements were acquired downstream of the Helmholtz resonator at a Reynolds number (Re_H) of 2525 based on the step height. These measurements were done for the unforced as well as forced flow conditions at different levels and frequencies of forcing. For each of the different forcing conditions, the measurements were done five times to ensure repeatability of the data. The average of these five data sets is then used to calculate the mean-pressure coefficient (C_p), given by Equation 2.4, which is plotted along the ordinate versus the normalized streamwise coordinate (x/H) in Figure 4.1 for the unforced case. The different colors represent the five different runs and the average of these five runs is shown in orange.

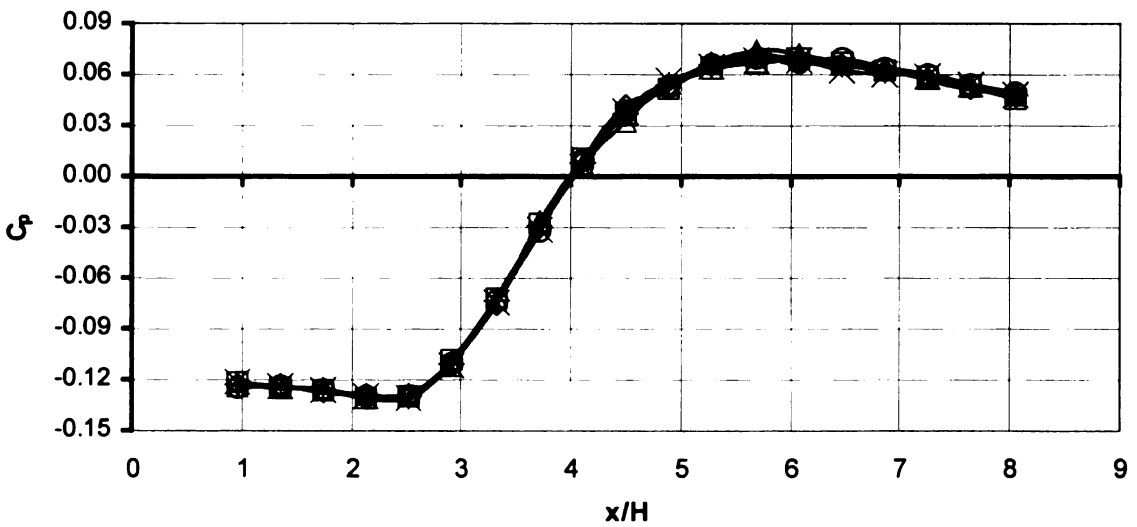

Figure 4.1. Mean-pressure distribution under no forcing condition

The mean-pressure distribution in Figure 4.1 is consistent with the classical backward-facing-step, wall-pressure profile, exhibiting an initial decrease to a minimum, followed by recovery through reattachment to a peak before gradually decreasing to

approach the freestream pressure. In the study of Hudy (2005), the peak location was found to be nominally 1.5 step heights downstream of x_r. For the unforced case in this study, the peak value is found at $5.5H$. Thus, the corresponding x_r value is $4H$. It is important to note that this is an approximate estimate and that a precise value can only be found from wall-shear-stress measurements. Nevertheless, the estimate compares well with data from the study of Li (2004) who did conduct wall-shear measurements on the same test model employed here. This comparison is shown in Figure 4.2, which contains a plot of the reattachment length normalized by the step height versus Re_H.

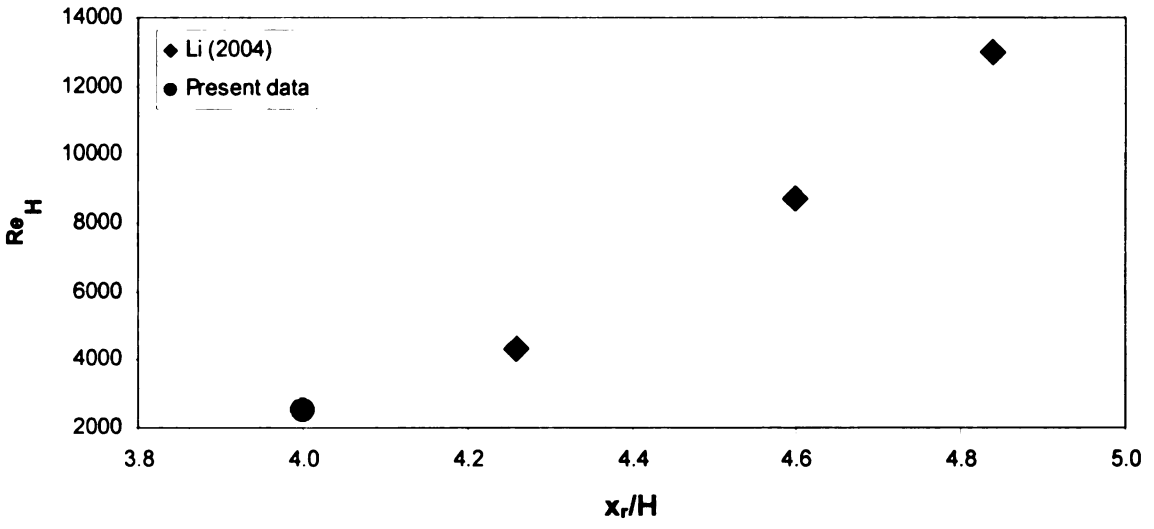

Figure 4.2. Reattachment length estimate from the present study and Li (2004) data

As evident from the plot, the estimated x_r/H value reasonably follows the Reynolds number trend of Li's data. This estimate is used in subsequent analysis for the calculation of the non-dimensional forcing frequency:

$$F^{+} = \frac{2 f_m x_r}{U_\infty} \tag{4.1}$$

Prior to discussing additional results, it is also significant to note that the level of forcing is expressed here using a non-dimensional momentum coefficient (C_μ). The definition of C_μ, which is the most commonly accepted form for expressing the forcing level for periodically excited flows (e.g., see Greenblatt and Wygnanski, 2000), is given by:

$$C_\mu = \frac{2 d u_{j,rms}^{\ 2}}{H U_\infty^{\ 2}} \tag{4.2}$$

where d is the resonator's slit opening width, H is the step height, $u_{j,rms}$ is the RMS jet velocity at a frequency of $2f_m$ (i.e., that produced by the low-frequency modulated streaming flow), and U_∞ is the mean flow velocity.

Figures 4.3 and 4.4 show the mean-wall-pressure profiles for different forcing frequencies and levels, respectively. Provided in these figures is the benchmark mean-pressure distribution corresponding to the unforced case (blue line). In Figure 4.3, the different forced cases correspond to five different F^{+} values (i.e., f_m of 10 Hz, 15 Hz, 18 Hz, 20 Hz, and 25 Hz) at the *same* level of forcing of C_μ = 0.0690%.

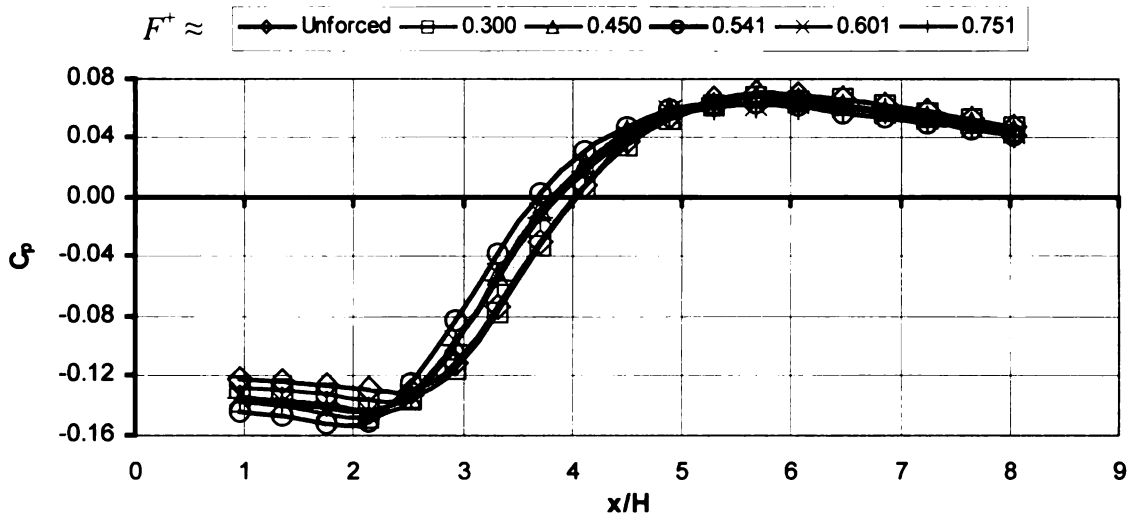

Figure 4.3. Forcing-frequency effect on the mean-pressure distribution beneath the separation bubble at $C_\mu = 0.0690\%$

A couple of interesting observations may be made from the data in Figure 4.3. First, is the apparent strengthening of the negative peak at a nominal value of $1.5H$ with increasing frequency up to F^+ of 0.541. If the frequency is increased beyond this value, the negative peak becomes less pronounced and gradually approaches the unforced value. Moreover, the start of the pressure recovery for the forced cases is evidently sooner (farther upstream) than that of the unforced case: the quicker the start of the recovery, the more pronounced is the negative C_p peak. This is especially seen for the black line (i.e., $F^+ \approx 0.541$), where the pressure begins to recover at $x = 2H$, in comparison to $2.5H$ for the unforced case (blue line).

The above demonstrates that the forcing device developed here has the capability of altering the entire separation bubble (as reflected in its mean-wall-pressure imprint). Moreover, it is also found that there is an optimum F^+ value of 0.541 (f_m = 18 Hz), which is evident from the strongest negative C_p peak along with the fact that the pressure begins to recover soonest in comparison to all other cases. The quicker recovery causes a shift

in the mean-pressure distribution towards the upstream direction, which suggests shrinking of the separation bubble and shortening of the reattachment length.

The observations concerning the forcing frequency effect above is consistent with that found in the literature by Chun and Sung (1996, 1998). They showed that increasing the forcing frequency beyond a critical value ($St_H \geq 0.8$) caused the reattachment length to become independent of the forcing frequency. In fact, Chun and Sung (1996) found that forcing frequencies that were higher than that of the critical value had an adverse effect on the reattachment length; hence, x_r became longer than the unforced case. They also found an optimal, non-dimensional, forcing frequency of 0.275 based on the step height and freestream velocity (this compares to 0.541 in the present study).

Greenblatt *et al.* (2005) associated the improved pressure recovery near reattachment with an intensifying, near-wall, reverse flow region that reduced reattachment length in their investigation of low control frequency ($F^+ < 1$). However, they found out that although the pressure drop immediately downstream of the control slot was smaller, the pressure recovery near reattachment was adversely affected when F^+ was increased beyond its optimum value ($F^+ \geq 1.35$). In another study, Glezer *et al.* (2005) observed the same effect of increasing actuation frequency. They observed a trend in which the actuation became less effective with increasing actuation frequency beyond the optimal value. Interestingly, though, in the Glezer *et al.* (2005) study, when the frequency was increased substantially beyond the optimal value (i.e., more than ten times), it was possible to effectively control the flow. However, this type of control differs substantially from oscillatory control that capitalizes on flow instabilities.

The effect of increasing C_μ at the optimum F^+ of 0.541 may be examined with the aid of Figure 4.4. Five different forcing levels (i.e., C_μ of 0.0003%, 0.0095%, 0.0280%, 0.0690%, and 0.1953%) were exercised. The mean-wall-pressure data for those cases, in addition to the unforced case, are displayed in Figure 4.4. It is seen that the effect of increasing the strength of the sound field driving the Helmholtz resonator produces a gradual, overall, shift of the mean-pressure distribution curves towards the upstream direction. The reader is reminded that the unforced case (blue line) serves as the benchmark pressure profile in this analysis. Moreover, it is evident that as the strength of the forcing is increased, the stronger is the negative C_p peak.

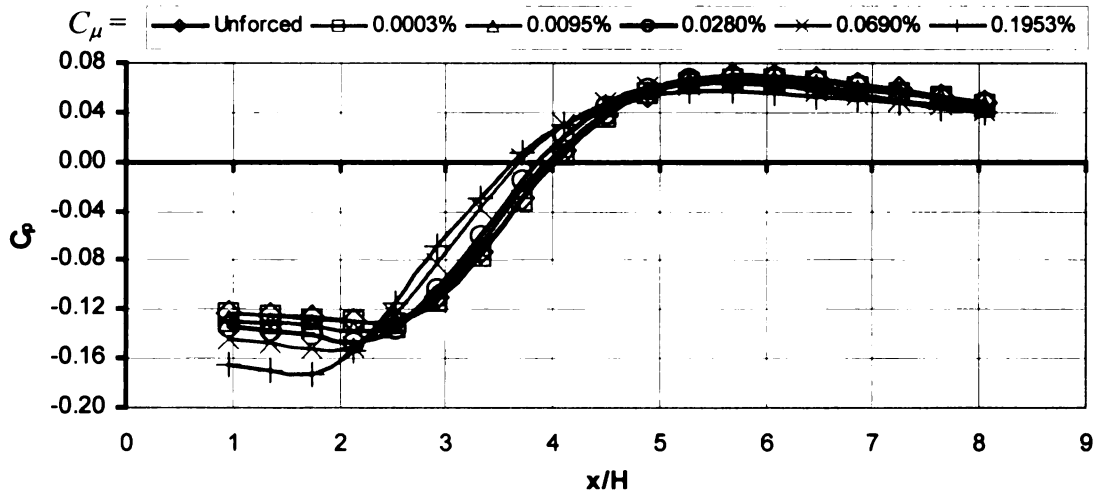

Figure 4.4. Forcing-amplitude effect on mean-pressure distributions at $F^+ \approx 0.541$

The above finding is consistent with that of the literature (e.g., Chun and Sung, 1996, Greenblatt and Wygnanski, 2000, and Greenblatt *et al.*, 2005). However, unlike these studies, where stronger forcing levels were exercised, it appears that the forcing device developed here produces disturbances that are not sufficiently strong to reach

saturation levels, beyond which increased forcing does not cause a proportional change in flow response.

An example of forcing saturation may be found in the study of Greenblatt *et al.* (2005). They found that the shortening of the separation bubble, seen from the pressure recovery, continued with increasing C_μ until $C_\mu \approx 0.11\%$. For higher values of C_μ, the forcing started to weaken the strength of the bubble.

4.2 The unsteady-wall-pressure signature beneath the forced bubble

4.2.1 RMS pressure distributions

The microphone array embedded in the surface of the model was used to measure the spatial distribution of pressure fluctuations resulting from flow structures within the separating/reattaching flow. These pressure fluctuations correspond to deviation of the instantaneous pressure from the mean-pressure value. To examine the strength of the wall-pressure fluctuations at different locations on the wall, one may analyze the root-mean-square (RMS) of the pressure fluctuations captured by each of the microphones embedded in the surface of the model.

The normalized RMS pressure fluctuation plots are shown in Figures 4.5 and 4.6. The normalizing factor for the RMS pressure fluctuations is the freestream dynamic pressure, given by $\frac{1}{2}\rho_{air}U_{\infty}^{2}$. Three-point averaging was used to remove some data scatter associated with microphone-calibration uncertainty. The abscissa represents the streamwise location of each of the microphones downstream of the separation point, normalized by the step height (H). The differently colored curves represent data for the unforced case and different forced cases.

In Figure 4.5, the forced cases correspond to the same C_{μ} of 0.0095% but two different excitation frequencies that include the optimal frequency: $F^{+} \approx 0.300$ and 0.541. It is important to note that for the fluctuating pressure results, it was not possible to show results for C_{μ} values larger than 0.0095% because of dynamic-range limitation of the measurement microphones. Specifically, although the sound field from the speaker did not contaminate the measurements at the forcing frequency ($2f_m$), it did so at ($f_c - f_m$) and ($f_c + f_m$). Because of the high intensity of the sound, the overall pressure fluctuations

exceeded the full-scale threshold of the wall microphones for cases corresponding to $C_\mu >$ 0.0095%.

Examination of the data in Figure 4.5 shows that directly downstream of the step, at the point of separation, the microphones sensed low RMS pressure fluctuations. Hudy (2001, 2005) and Hudy *et al.* (2003) found that the shear layer at the point of separation is too far away from the wall-pressure sensors to influence the measured fluctuations near the step. The small RMS values near separation have been generally linked to the unsteadiness or 'flapping' of the shear layer. Beyond x/H = 2, there is a significant increase in the wall-pressure fluctuations, which is consistent with that of the literature (e.g., see Lee and Sung, 2001). It is generally believed that the increase of the RMS pressure fluctuations is associated with the growth of the shear layer vortical structures. These vortical structures grow in size and strength, and eventually convect downstream while moving closer to the wall. This flow behavior causes the increase in the RMS pressure signature up to a maximum level where the flow "impinges" on the wall as described by Farabee and Casarella (1986). This scenario of a downwards-curved shear layer containing spatially evolving vortex structures, was contradicted recently by the findings of Hudy (2005). In her study, Hudy found the vortex structures to develop to full size (of the order of the step size) in place near the middle of the reattachment zone, before convecting downstream. Albeit different, the scenario was found to be consistent with the shape of the RMS distributions shown in Figure 4.5. In fact, Hudy's measurements were conducted on the same test model as that used here.

The unforced case, shown using the blue line in Figure 4.5, has the lowest RMS pressure. Stronger level of wall-pressure fluctuations, reflective of the influence of flow

control, is found for the forced cases. It is notable that the increase in fluctuation level is not associated with a change in the streamwise location of the peak RMS value (within the uncertainty of the measurements). This peak is known to occur at or slightly upstream of the reattachment location. Therefore, the results suggest that for the forcing conditions of the cases examined in Figure 4.5, there is no substantial shrinkage in the separation bubble. This is consistent with the results given in Figure 4.4, where it is seen that the change in the mean-pressure distribution for C_μ = 0.0095% reflects very small bubble shrinkage. Such a small change is difficult to detect in the RMS pressure measurements.

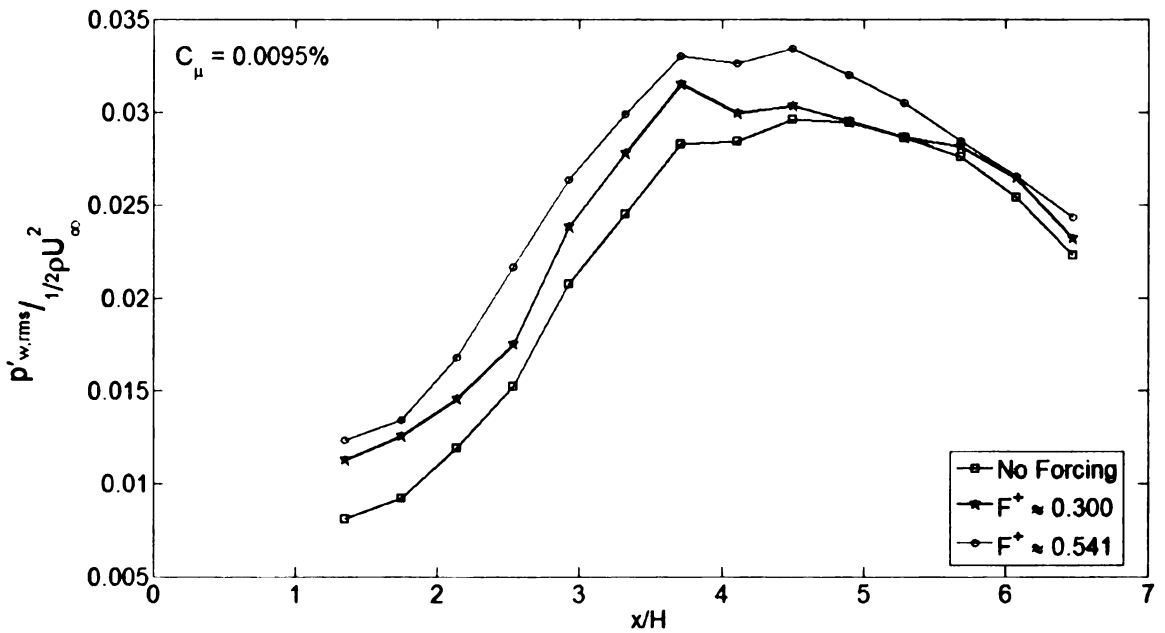

Figure 4.5. Effect of forcing frequency (F^+) on RMS wall-pressure measurements

To examine the effect of the forcing amplitude, RMS pressure results obtained at the most effective F^+ but two different C_μ values are shown in Figure 4.6. For reference, the figure also contains the RMS pressure fluctuations for the unforced case. It is evident

that the lower forcing amplitude yielded pressure fluctuation level that is hardly distinguishable from the unforced case. On the other hand, the increased level of pressure fluctuations at the forcing level of 0.0095% is clearly visible.

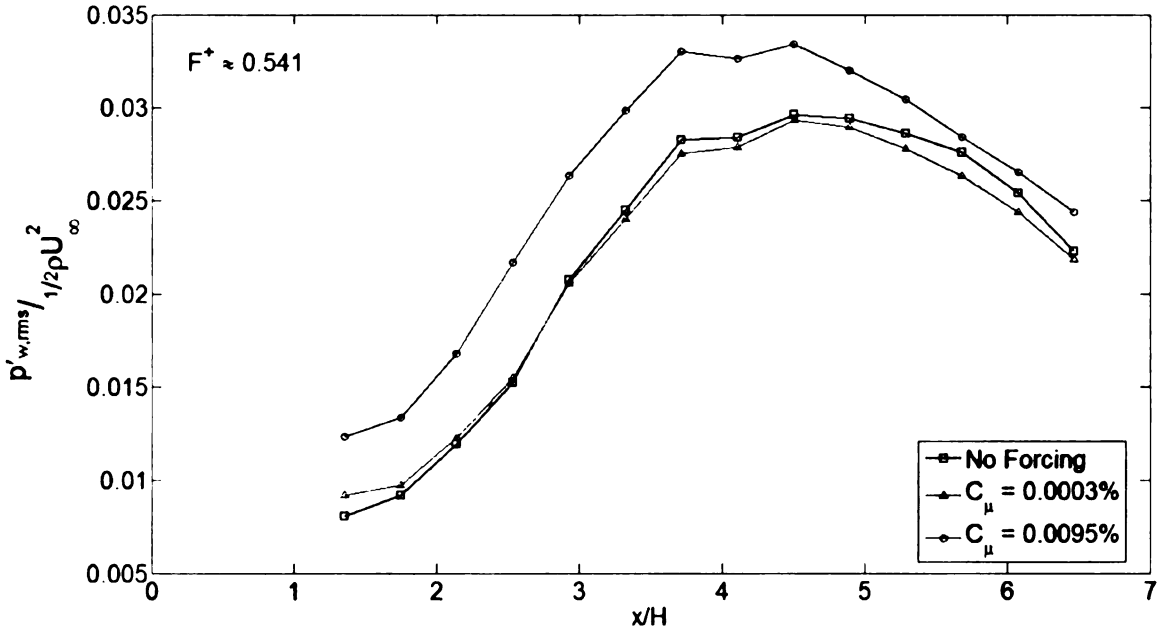

Figure 4.6. Effect of forcing level (C_μ) on RMS wall-pressure measurements

4.2.2 Power Spectrum Density (PSD)

Figure 4.7 show seven plots of the wall-pressure power spectral density at the streamwise location of all microphones. The specific x locations are: x/H = 1.35, 2.14, 2.93, 3.72, 4.50, 5.29, and 6.08. Generally speaking, PSD plots provide frequency-content information of a time signal (e.g., a power spectrum plot can identify at which frequencies the largest fluctuation in a signal occur). In the present analysis, this information can be useful in characterizing the frequency content of the pressure signature of the flow structures. The equation used for calculating the discrete, one-sided, PSD was given earlier (Equation 3.1).

In the seven PSD plots, the abscissa represents frequency plotted up to 150 Hz, since no significant wall-pressure fluctuation exists at higher frequencies, while the ordinate shows the power spectrum magnitude. Each of the plots contains spectra for four different test configurations. These are the unforced-flow case along with three forced-flow cases corresponding to two different F^+ values (0.300 and 0.541) at C_μ = 0.0095%, and two different C_μ values (0.0003% and 0.0095%) at $F^+ \approx 0.541$.

The first plot shown in Figure 4.7 shows the power spectra at the streamwise location closest to the point of separation. At this location (x/H = 1.35), all four data sets show very low spectrum values in accordance with the low level of pressure fluctuations found near separation (see Figure 4.5 and 4.6). However, the effect of the forcing imposed at the higher forcing amplitude (C_μ = 0.0095%) is clearly visible in the small harmonic peaks found at 20 Hz and 36 Hz (F^+ = 0.300 and 0.541, respectively).

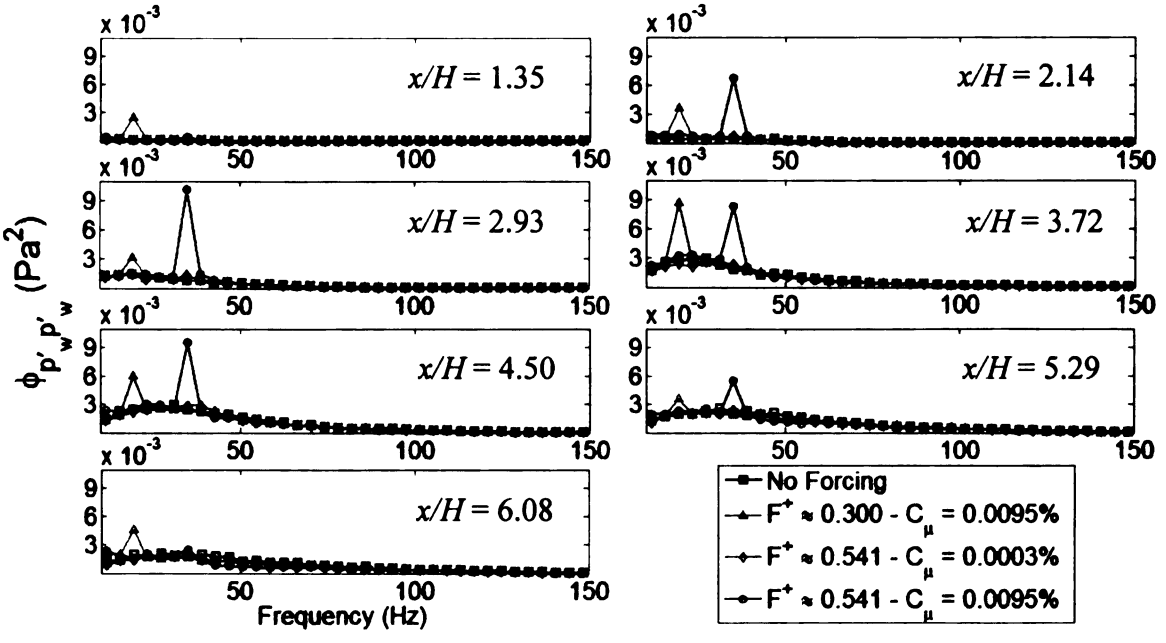

Figure 4.7. One-sided power spectra of the surface pressure at different streamwise locations downstream of the step

The harmonic peak at the forcing frequency becomes stronger with increasing downstream distance up to a certain x location before it starts to decay again. This is consistent with that found in the recent study by Liu *et al.* (2005), who also employed a wall microphone array in a study of a harmonically-excited back-step flow. Although, this is true for both forcing frequencies, the x location at which the peak is highest is more upstream for the lower frequency. Specifically, for $F^+ = 0.300$, the highest peak is found at $x/H = 3.72$, while for $F^+ = 0.541$, the corresponding location is $x/H = 2.93$. This may be seen more clearly in Figure 4.8, where the spectrum magnitude at the frequency of the forcing is plotted (after subtraction of the spectrum value corresponding to the unforced case) for all x locations (note that, similar to the RMS results, three-point averaging was employed to remove some data scatter associated with microphone-calibration uncertainty).

Further examination of Figure 4.8 shows that although the spectrum peak at the higher, forcing frequency is attained farther downstream, the associated pressure fluctuations actually start to amplify quicker (i.e., farther upstream) relative to the lower forcing frequency. Initially, the amplification rate is strong, followed by slow growth, or possibly a flat profile within the uncertainty of the data, for a good stretch of the measurement domain. In contrast, the data at the lower, off-optimal, frequency show the associated pressure fluctuations to start to grow at a farther downstream location relative to the higher forcing frequency. Subsequently, these fluctuations amplify quickly, but the data do not exhibit a streamwise stretch over which the fluctuations strength is sustained. Instead, growth of the pressure fluctuations is immediately followed by rapid decay. These observations are consistent with the findings of Greenblatt *et al.* (2005), who

measured the pressure fluctuations beneath a separation bubble downstream of a wall-mounted "hump" under different forcing conditions.

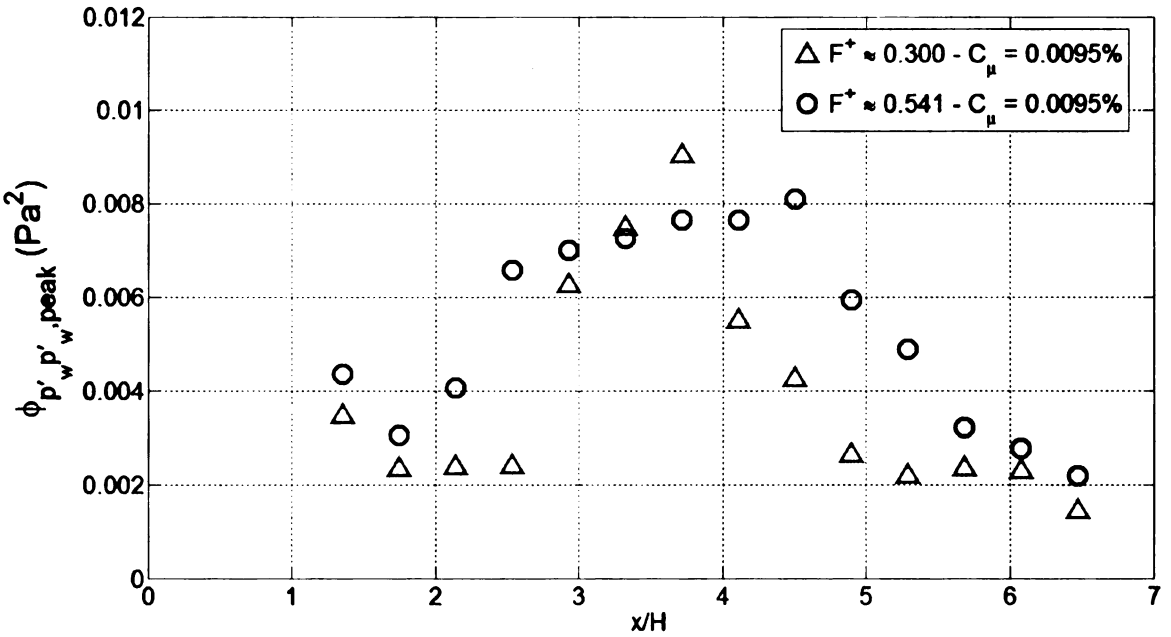

Figure 4.8. Streamwise distribution of the pressure-spectrum magnitude at the forcing frequency for forcing level of C_μ = 0.0095%

4.2.3 Frequency-wavenumber spectra

The frequency-wavenumber (f-k_x) spectrum corresponds to the two-dimensional Fourier transformation of the spatio-temporal, wall-pressure signal's [$p'_w(x,t)$] auto-correlation. The resulting spectra breakdown the energy content of the wall-pressure field into contributions at different frequency and wavenumber combinations. Here, data from fifteen microphones were used in obtaining the f-k_x spectra. The sampling rate used for each of the microphones during the measurements was 8 kHz for 33 seconds. A total of 262,144 (2^{18}) number of samples for each of the microphones were used to create a 262,144 x 15 (time x space) two-dimensional array that made up the entire data set. This

data set was then divided into sub-arrays of 1024 rows x 32 columns, which allowed averaging of the spectrum over 256 records and produced a random uncertainty of 6.25%. It should be noted that the space array was padded with zeros to increase its size from 15 to 32 in order to obtain the resulting spectrum at smaller wavenumber increments via interpolation. To calculate the f-k_x spectrum, Fast Fourier Transform (FFT) of each of the 1024 x 32 records was first taken along the time dimension. A second FFT was then calculated along the space dimension to change the spatial domain representation into the wavenumber domain. Finally, the resulting 2D FFT was multiplied by its conjugate to arrive at the frequency-wavenumber spectrum.

Frequency-wavenumber (f-k_x) spectrum plots representing the four different cases considered for the RMS and PSD analyses above, are shown in Figures 4.9 through 4.12. For all the f-k_x plots, the ordinate gives the frequency normalized by the step height (H) and freestream velocity (U_∞). The abscissa represents the wavenumber normalized with the step height. The color bar on the right side represents the magnitude of the spectrum normalized by its maximum peak value, resulting in a "zero-to-one" scale.

For all the plots, there are two identifiable regions where the pressure-fluctuation energy is concentrated. The bulk of the pressure fluctuation is found to be associated with a "ridge" that is inclined at an angle and located in the right-hand plane ($k_x > 0$). Noting that the slope of a line drawn from the origin of the f-k_x spectrum to any point in the f-k_x plane gives the convection velocity of the corresponding disturbance, it is evident that this ridge represents the signature of downstream-traveling (positive convection velocity) disturbances. In the unforced case, Hudy (2005) showed that this ridge is the result of the pressure fluctuations produced by large-scale (order of H) vortices that form

via the roll-up of the separated shear layer, near the center of the re-circulation zone, and convect downstream. In addition to the "convective ridge", some weak pressure fluctuations are found in the $k_x < 0$ half plane. This signifies that some of the wall-pressure fluctuations beneath the separation bubble are associated with upstream traveling disturbances. These presumably are related to the back-flow within the separation bubble.

Focusing on the convective ridge in the unforced-flow case shown in Figure 4.9, it is seen that there is a preferred frequency/wavenumber where the ridge attains its highest value. The peak associated with this preferred mode is identified at $fH/U_\infty \approx 0.103$ and k_xH of 0.289.

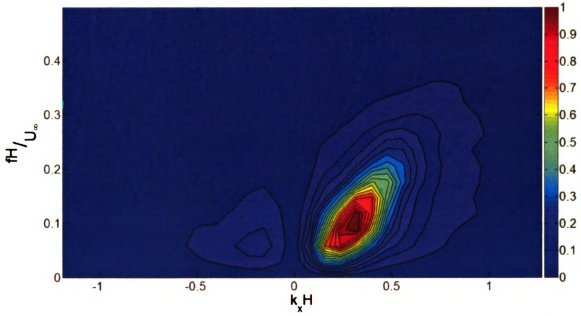

Figure 4.9. Wall-pressure frequency-wavenumber spectrum for the unforced-flow case

Figure 4.10 shows the f-k_x spectrum when forcing the flow at $F^+ \approx 0.300$ (10 Hz modulation frequency, or $f_eH/U_\infty = 0.075$) and C_μ of 0.0095%. Two main observations are found here. First, it is evident that the frequency of the peak of the convective ridge shifts from the unforced value identified earlier to a value equal to that of the forcing frequency. The corresponding wavenumber is found to be $k_xH = 0.268$. The second observation that can be made from Figure 4.10 is that the convective ridge is found to be less broad in comparison with the spectrum of the unforced case (Figure 4.9). This suggests that the forcing leads to better organization of the wall-pressure-generating flow structures: consistent with expectation.

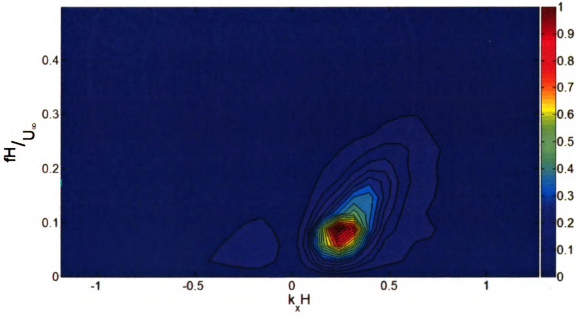

Figure 4.10. Wall-pressure frequency-wavenumber spectrum for the forced flow ($F^+ \approx 0.300$ [$f_eH/U_\infty = 0.075$] and $C_\mu = 0.0095\%$)

Figure 4.11 represents the f-k_x spectrum obtained when forcing the flow at the optimal forcing frequency $F^+ \approx 0.541$ (18 Hz modulation frequency, or $f_eH/U_\infty = 0.135$)

forcing condition, but very low forcing amplitude (C_μ = 0.0003%). In concert with the RMS and frequency spectrum results, very little difference is seen in the f-k_x spectrum results between the forced and unforced cases because of the minute level of forcing. At the higher forcing level of C_μ = 0.0095% (Figure 4.12), while forced at the optimum frequency, the f-k_x spectrum shows the strongest deviation from the spectrum of the natural flow. Similar to the results shown in Figure 4.10 for F^+ = 0.300, the global spectrum peak is found at the forcing frequency, and the overall spectrum becomes substantially narrower than for the natural case, indicating better organization of the flow features generating the surface-pressure fluctuations. The wavenumber corresponding to the global spectrum peak is found at k_xH = 0.350.

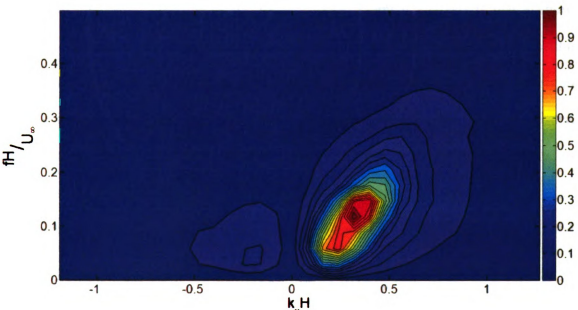

Figure 4.11. Wall-pressure frequency-wavenumber spectrum for the forced flow ($F^+ \approx 0.541$ [$f_eH/U_\infty = 0.135$] and $C_\mu = 0.0003\%$)

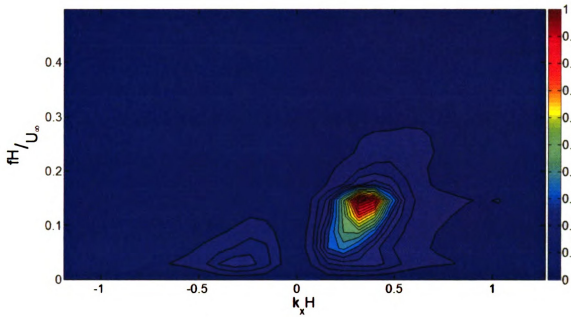

Figure 4.12. Wall-pressure frequency-wavenumber spectrum for the forced flow ($F^+ \approx 0.541$ [$f_c H/U_\infty = 0.135$] and $C_\mu = 0.0095\%$)

An interesting outcome of the frequency-wavenumber analysis is that it shows that the wavenumber of the forced disturbance could be predicted a priori (at least within the forcing and flow parameters employed here). To demonstrate this, consider Figure 4.13 where the f-k_x of the unforced-flow case is re-examined with focus on positive wavenumbers only. The peaks of the convective ridge at different frequencies are identified and shown in yellow circles in the figure. A linear fit to the circles (red dashed line) is employed to provide an analytic equation describing the top of the ridge (or most energetic disturbances at different frequencies). As seen from Figure 4.13, the straight line provides good representation of the ridge top (the data scatter around the line is related to the resolution of the spectrum). Using the obtained linear relation in conjunction with the forcing-frequency values, it was then possible to predict the wavenumbers of the most energetic disturbances in the natural flow at the same

frequency as the forced disturbances. This is illustrated with the broken white lines in Figure 4.13 for $f_eH/U_\infty = 0.075$ (or $f_m = 10$ Hz) and $f_eH/U_\infty = 0.135$ (or $f_m = 18$ Hz). The corresponding wavenumber estimates are $k_xH = 0.256$ and 0.354 respectively, which when compared to the wavenumbers identified earlier from the spectrum peak for the forced flow cases at $C_\mu = 0.0095\%$ ($k_xH = 0.268$ and 0.350) yield an error percentage of less than 5%: a value that is well within the wavenumber resolution of the spectrum. Thus, it appears that the spatial scale of the forced disturbance is pre-set by the natural-flow's frequency-wavenumber characteristics. This finding is interesting in the sense that it provides means for predicting the wavenumber for a given forcing frequency. This may be used, for instance, to shift the wavenumber of a dominant existing disturbance to be far removed from resonant wavenumbers of an underlying surface in order to reduce or eliminate flow-induced noise and vibration.

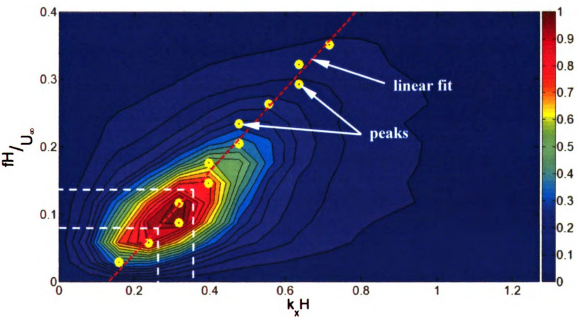

Figure 4.13. Wall-pressure frequency-wavenumber spectrum for the unforced flow, showing straight-line fit to the peak of the convective ridge

5 CONCLUSIONS AND RECOMMENDATIONS

The results from the present investigation are recapitulated below, followed by recommendations for future work.

5.1 Conclusions

An externally driven Helmholtz resonator was designed and implemented for forcing the separated flow over an axisymmetric, backward-facing step at a Reynolds number based on step height of Re_H = 2525. The new device, which allowed the introduction of disturbances to the flow at the point of separation, was used to investigate the effect of the forcing on the wall-pressure signature beneath the separating/reattaching flow downstream of the step.

The acoustic and fluidic disturbance produced by the Helmholtz resonator was characterized utilizing microphone and single-hotwire measurements. The results showed that the frequency at which the strongest fluidic disturbance was produced did not coincide with the resonance frequency of the device. The strongest fluidic disturbance was found at 630 Hz, while the Helmholtz resonator had a resonance frequency of 657 Hz. The difference was due to resonance of the wind tunnel that amplified the device's disturbance at 630 Hz. Nevertheless, the resonator's frequency response (both amplitude and phase) agreed well with the response of a second-order, lumped-parameter system. This confirmed that the oscillations produced by the resonator corresponded to the lowest-order, or Helmholtz, resonance.

Because the frequency at which the flow was most receptive to disturbances was more than an order of magnitude lower than the operating frequency of the device of 630

Hz, a low-frequency amplitude-modulation of the operating (carrier) frequency was employed to effectively couple the perturbation to the flow. The success of this coupling was linked to modulation of the streaming (steady) flow component produced by the driven resonator. In particular, it was found that driving the resonator using a pure harmonic signal produced both an oscillating and streaming fluidic disturbance. The latter is a result of non-linearity of Helmholtz resonators when driven at high intensities of sound (e.g., see Ingard and Labate, 1950). Thus, by modulating the driving acoustic signal of the resonator, the streaming flow component produced a low-frequency jet that excited the flow at the appropriate frequencies.

An additional advantage of the forcing scheme adopted here, which is particularly important to surface-pressure studies, is that the flow disturbance was fluidic rather than acoustic in nature. The acoustic signature of the forcing scheme (primarily from the driving speaker) was confined to high frequencies (near the carrier frequency) and hence it could be removed from the surface-pressure measurements via simple low-pass filtering. It was noted, though, that at forcing levels substantially higher than those employed here, the fluidic disturbance itself might become an effective noise source. Under these conditions the device could not be considered acoustically quite.

The optimum modulation frequency at which coupling of the resonator's disturbance to the flow was most effective was found to be $F^+ \approx 0.541$. At this frequency, a pronounced shift in the mean-pressure distribution towards the upstream direction suggested shrinking of the separation bubble and shortening of the mean reattachment length, x_r. The optimum F^+ value found in the present study is twice the value found by Greenblatt and Wygnanski (2000), Chun and Sung (1996), and Chun *et al.* (1999). The

difference might be due to the geometry. Unlike the axisymmetric model, the planar geometry might be affected by end-walls effect.

The effect of excitation level, C_μ, on the mean-pressure distribution was also examined at the optimum F^+. The results showed monotonic reduction in the separation bubble size with increasing forcing level. However, the range of excitation levels investigated here did not reach the saturation level suggested in the literature at very large forcing levels. Chun and Sung (1996), Greenblatt and Wygnanski (2000), and Greenblatt *et al.* (2005) suggested that flow excitation at saturation levels does not cause proportional change in flow response. Overall, the above demonstrates that the forcing device developed here has the capability of altering the behavior of the entire separation bubble, and not just the local characteristics of the separated shear layer.

The unsteady-wall-pressure imprint beneath the separating/reattaching flow region was measured using an array of 15 wall-pressure microphones. Fluctuating-pressure RMS, power spectrum density (PSD), and frequency-wavenumber (f-k_x) spectra were analyzed. However, the C_μ values employed for this analysis were limited to within 0.0095% due to the upper limit of the dynamic-range of the measurement microphones. Overall, it was found that the wall-pressure fluctuations became more energetic and organized as a result of the forcing. Additionally, PSD results showed that the harmonic peak at the forcing frequency became stronger with increasing downstream distance up to a certain x location before it started to decay again. The streamwise range over which sustained growth of the forced disturbance was found was substantially larger when forcing at the optimal, in comparison to other, frequencies. When forcing at an off-

optimal frequency, the pressure oscillations at the forcing frequency exhibited rapid decay following the initial growth.

An interesting outcome of the frequency-wavenumber-spectrum analysis was the finding that the spatial scale, i.e., streamwise wavenumber, for the wall-pressure disturbance at a given forcing frequency could be predicted using the peak-locus of the convective ridge in the frequency-wavenumber spectrum of the unforced flow. This finding may be used, for instance, as basis for selecting the forcing frequency in order to produce a particular wavenumber associated with the dominant wall-pressure disturbance. This could be useful in reducing or eliminating flow-induced noise and vibration by selecting a wavenumber that is far removed from the resonant wavenumbers of an underlying surface.

5.2 Recommendations for future work

There are still several interesting aspects to explore in attempt to further investigate the effect of amplitude-modulated forcing on the axisymmetric, backward-facing-step flow. Increasing the excitation level beyond that attained here would be useful to confirm the saturation behavior suggested by Chun and Sung (1996) and Greenblatt and Wygnanski (2000). Additionally, unsteady wall-pressure measurements using microphones with wider dynamic range can facilitate higher levels of excitation than was possible here.

Aside from wall-pressure information, it is also significant to examine if the amplitude-modulated excitation alters the flow field in a manner that is similar to the more common method of harmonic excitation. To accomplish this, a velocity-field study is of interest. Measurements using a single-hotwire sensor have been recently completed in the Flow Physics and Control Laboratory (FPaCL) to address this point (Trosin, 2006). Finally, a nice complement to the present data would be oil-film interferometry (OFI) to directly determine the reattachment length under different forcing conditions.

REFERENCES

Amitay, M., Smith, D. R., Kibens, V., Parekh, D. E., and Glezer, A., "Aerodynamic Flow Control over an Unconventional Airfoil Using Synthetic Jet Actuators," *AIAA Journal*, Vol. 39, No. 3, March 2001, pp. 361 – 370.

Amitay, M. and Glezer, A., "Role of Actuation Frequency in Controlled Flow Reattachment over a Stalled Airfoil," *AIAA Journal*, Vol. 40, No. 2, February 2002, pp. 209 – 216.

Chanaud, R. C., "Effects of Geometry on the Resonance Frequency of Helmholtz Resonator," *Journal of Sound and Vibration*, Vol. 178, No. 3, 1994, pp. 337 – 348.

Cherry, N. J., Hillier, R., and Latour, M. E. M. P., "Unsteady Measurements in a Separated and Reattaching Flow," *Journal of Fluid Mechanics*, Vol. 144, July 1984, pp. 13 – 46.

Chun, K. B. and Sung, H. J., "Control of Turbulent Separated Flow over a Backward-Facing Step by Local Forcing," *Experiments in Fluids*, Vol. 21, No. 6, November 1996, pp. 417 – 426.

Chun, K. B. and Sung, H. J., "Visualization of Locally-Forced Separated Flow over a Backward-Facing Step," *Experiments in Fluids*, Vol. 25, No. 2, July 1998, pp. 133 – 142.

Chun, K. B., Lee, I., and Sung, H. J., "Effect of Spanwise-Varying Local Forcing on Turbulent Separated Flow over a Backward-Facing Step," *Experiments in Fluids*, Vol. 26, No. 5, April 1999, pp. 437 – 440.

Daoud, M. I., "Stochastic Estimation of the Flow Structure Downstream of a Separating/Reattaching Flow Region using Wall-Pressure Array Measurements," *Ph.D. Dissertation*, Michigan State University, 2004.

Driver, D. M., Seegmiller, H. L., and Marvin, J. G., "Time-Dependent Behavior of a Reattaching Shear Layer," *AIAA Journal*, Vol. 25, No. 7, July 1987, pp. 914 – 919.

Farabee, T. M. and Casarella, M. J., "Measurements of Fluctuating Wall Pressure for Separated/Reattached Boundary Layer Flows," *Journal of Vibration, Acoustics, Stress, and Reliability in Design*, Vol. 108, 1986, pp. 301 – 307.

Glezer, A. and Amitay, M., "Synthetic Jets," *Annual Review of Fluid Mechanics*, Vol. 34, 2002, pp. 503 –529.

Glezer, A., Amitay, M., and Honohan, A. M., "Aspects of Low- and High-Frequency Actuation for Aerodynamic Flow Control," *AIAA Journal*, Vol. 43, No. 7, July 2005, pp. 1501 – 1511.

Greenblatt, D. and Wygnanski, I. J., "The Control of Flow Separation by Periodic Excitation," *Progress in Aerospace Sciences*, Vol. 36, 2000, pp. 487 – 545.

Greenblatt, D., Paschal, K. B., Yao, C. S., and Harris, J., "A Separation Control CFD Validation Test Case Part 2. Zero Efflux Oscillatory Blowing," *43rd Aerospace Sciences Meeting and Exhibit*, AIAA 2005-0485, Reno, NV, January 10 – 13, 2005.

Heenan, A. F. and Morrison, J. F., "Passive Control of Pressure Fluctuations Generated by Separated Flow," *AIAA Journal*, Vol. 36, No. 6, June 1998, pp. 1014 – 1022.

Hudy, L. M., "Simultaneous Wall-Pressure Array and PIV Measurements in a Separating/Reattaching Flow Region," *Masters thesis*, Michigan State University, 2001.

Hudy, L. M., Naguib, A. M., and Humphreys, W. M., "Wall-Pressure-Array Measurements Beneath a Separating/Reattaching Flow Region," *The Physics of Fluids*, Vol. 15, No. 3, March 2003, pp. 706 – 717.

Hudy, L. M., "Simultaneous Wall-Pressure and Velocity Measurements in the Flow Field Downstream of an Axisymmetric Backward-Facing Step," *Ph.D. Dissertation*, Michigan State University, 2005.

Hudy, L. M., Naguib, A. M., and Humphreys, W. M., "Stochastic Estimation of a Separated-Flow Field using Wall-Pressure-Array Measurements," *44th Aerospace Sciences Meeting and Exhibit*, AIAA 2006-1115, Reno, NV, January 9 – 12, 2006.

Ingard, U. and Labate, S., "Acoustic Circulation Effects and the Nonlinear Impedance of Orifices," *The Journal of the Acoustical Society of America*, Vol. 22, No. 2, March 1950, pp. 211 – 218.

Ingard, U., "On the Theory and Design of Acoustic Resonators," *The Journal of the Acoustical Society of America*, Vol. 25, No. 6, November 1953, pp. 1037 – 1061.

Ingard, U. and Ising, H., "Acoustic Nonlinearity of an Orifice," *The Journal of the Acoustical Society of America*, Vol. 42, No. 1, February 1967, pp. 6 – 17.

Kinsler, L. E., Frey, A. R., Coppens, A. B., and Sanders, J. V., *Fundamentals of Acoustics*, 3rd edition, New York: John Wiley & Sons, Inc., 1982.

Lebedeva, I. V., "Experimental Study of Acoustic Streaming in the Vicinity of Orifices," *Sov. Phys. Acoust. – American Institute of Physics (1981)*, Vol. 26, No. 4, July – August 1980, pp. 331 – 333.

Lee, I. and Sung, H. J., "Characteristics of Wall Pressure Fluctuations in Separated and Reattaching Flows over a Backward-Facing Step," *Experiments in Fluids*, Vol. 30, No. 3, March 2001, pp. 262 – 272.

Lee, I. and Sung, H. J., "Multiple-Arrayed Pressure Measurement for Investigation of the Unsteady Flow Structure of a Reattaching Shear Layer," *Journal of Fluid Mechanics*, Vol. 463, July 2002, pp. 377 – 402.

Li, Y., "Investigation of the Wall-Shear-Stress Signature in a Backward-Facing-Step Flow using Oscillating Hot-wire Sensors," *Ph.D. Dissertation*, Michigan State University, 2004.

Liu, Y. Z., Kang, W., and Sung, H. J., "Assessment of the Organization of a Turbulent Separated and Reattaching Flow by Measuring Wall Pressure Fluctuations," *Experiments in Fluids*, Vol. 38, No. 4, April 2005, pp. 485 – 493.

Roos, F. W. and Kegelman, J. T., "Control of Coherent Structures in Reattaching Laminar and Turbulent Shear Layers," *AIAA Journal*, Vol. 24, No. 12, December 1986, pp. 1956 – 1963.

Schubauer G. B. and Skramstad, H. K., "Laminar Boundary Layer Oscillations and Transition on a Flat Plate," *NACA Report 909*, 1948.

Trosin B. J., "Velocity-Field Measurements of an Axisymmetric Separated Flow Subjected to Amplitude-Modulated Excitation," *Masters thesis*, Michigan State University, 2006.

Urzynicok, F. and Fernholz, H. H., "Flow-Induced Acoustic Resonators for Separation Control," *1st Flow Control Conference*, AIAA 2002-2819, St. Louis, MO, June 24 – 27, 2002.

Wee, D., Park, S., Yi, T., Annaswamy, A. M., and Ghoniem, A. F., "Reduced Order Modeling of Reacting Shear Flow," *40th Aerospace Sciences Meeting and Exhibit*, AIAA 2002-0478, Reno, NV, January 14 – 17, 2002.

Wiltse, J. M. and Glezer, A., "Manipulation of Free Shear Flows using Piezoelectric Actuators," *Journal of Fluid Mechanics*, Vol. 249, 1993, pp. 261 – 285.

Wu, K. E. and Breuer, K. S., "Dynamics of Synthetic Jet Actuator Arrays for Flow Control," *33rd Fluid Dynamics Conference and Exhibit*, AIAA 2003-4257, Orlando, FL, June 23 – 26, 2003.

General references

Doebelin, E. O., *Measurement Systems: Application and Design*, 4th edition, New York: McGraw-Hill, Inc., 1975.

Fox, R. W. and McDonald, A. T., *Introduction to Fluid Mechanics*, 3rd edition, New York: John Wiley & Sons, Inc., 1985.

Potter, M. C. and Wiggert, D. C., with Hondzo, M. and Shih, T. I. P., *Mechanics of Fluids*, 3rd edition, California: Brooks/Cole – Thomson Learning, Inc., 2002.

Thomson, W. T. and Dahleh, M. D., *Theory of Vibration with Applications*, 5th edition, New Jersey: Prentice-Hall, Inc., 1993.

Zuckerwar, A. J., "Acoustical Measurement," *Encyclopedia of Physical Science and Technology*, Vol. 1, 3rd edition, California: Academic Press, 2002.